AD_____

GRANT NUMBER DAMD17-94-J-4362

TITLE: Development of Methods for Improved Breast Imaging Using Ultrasound

PRINCIPAL INVESTIGATOR: Dr. John M. Reid

CONTRACTING ORGANIZATION: Drexel University
Philadelphia, Pennsylvania 19104

REPORT DATE: July 1996

TYPE OF REPORT: Final

PREPARED FOR: Commander
U.S. Army Medical Research and Materiel Command
Fort Detrick, Frederick, Maryland 21702-5012

DISCLAIMER NOTICE

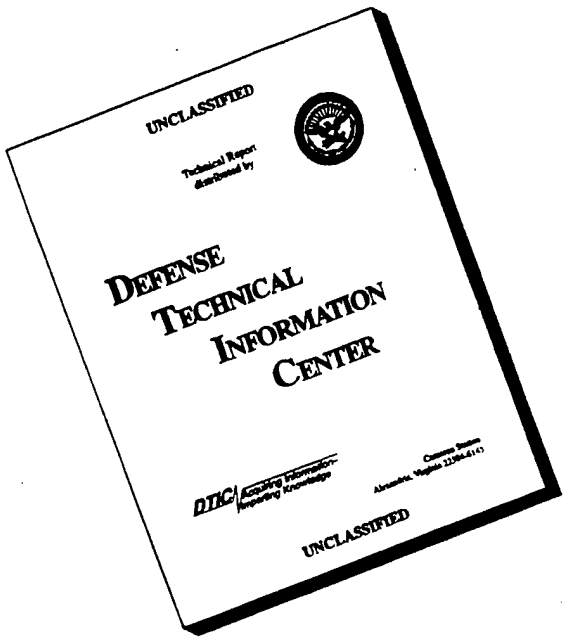

THIS DOCUMENT IS BEST QUALITY AVAILABLE. THE COPY FURNISHED TO DTIC CONTAINED A SIGNIFICANT NUMBER OF PAGES WHICH DO NOT REPRODUCE LEGIBLY.

REPORT DOCUMENTATION PAGE

Form Approved
OMB No. 0704-0188

1. AGENCY USE ONLY *(Leave blank)*	2. REPORT DATE	3. REPORT TYPE AND DATES COVERED
	July 1996	Final (1 Jul 94 - 30 Jun 96)

4. TITLE AND SUBTITLE
Development of Methods for Improved Breast Imaging Using Ultrasound

5. FUNDING NUMBERS
DAMD17-94-J-4362

6. AUTHOR(S)
Dr. John M. Reid

7. PERFORMING ORGANIZATION NAME(S) AND ADDRESS(ES)
Drexel University
Philadelphia, Pennsylvania 19104

8. PERFORMING ORGANIZATION REPORT NUMBER

9. SPONSORING/MONITORING AGENCY NAME(S) AND ADDRESS(ES)
Commander
U.S. Army Medical Research and Materiel Command
Fort Detrick, Frederick, MD 21702-5012

10. SPONSORING/MONITORING AGENCY REPORT NUMBER

11. SUPPLEMENTARY NOTES

12a. DISTRIBUTION / AVAILABILITY STATEMENT
Approved for public release; distribution unlimited

12b. DISTRIBUTION CODE

13. ABSTRACT *(Maximum 200*

A novel framework was introduced for the deconvolution of B-scan images. A model for the rf image was developed first, and then imaging distortions were reconstructed using higher-order statistics of the measured image lines. Based on the estimated distortions deconvolution of the corresponding image was performed, which for the case of images of tissue mimicking phantom as well as human tissue images, led to significant resolution improvement. In the past, estimation of distortions has been carried out using exclusively second order statistics (autocorrelation). Autocorrelation, however, can recover only the minimum phase equivalent of the true distortions, because it is blind to phase. Imaging distortions were also estimates using second order statistics of the image lines. It was demonstrated that although these estimates did lead to resolution improvement, the amount of improvement was far less significant than the one obtained with the higher-order statistics based estimates.

14. SUBJECT TERMS	15. NUMBER OF PAGES
Ultrasound, Radiology, Diagnosis, Imaging, Deconvolution, Detection, Cancer, Young, Women, Resolution, Improvement, Breast Cancer	85
	16. PRICE CODE

17. SECURITY CLASSIFICATION OF REPORT	18. SECURITY CLASSIFICATION OF THIS PAGE	19. SECURITY CLASSIFICATION OF ABSTRACT	20. LIMITATION OF ABSTRACT
Unclassified	Unclassified	Unclassified	Unlimited

FOREWORD

Opinions, interpretations, conclusions and recommendations are those of the author and are not necessarily endorsed by the US Army.

____ Where copyrighted material is quoted, permission has been obtained to use such material.

____ Where material from documents designated for limited distribution is quoted, permission has been obtained to use the material.

____ Citations of commercial organizations and trade names in this report do not constitute an official Department of Army endorsement or approval of the products or services of these organizations.

____ In conducting research using animals, the investigator(s) adhered to the "Guide for the Care and Use of Laboratory Animals," prepared by the Committee on Care and Use of Laboratory Animals of the Institute of Laboratory Resources, National Research Council (NIH Publication No. 86-23, Revised 1985).

____ For the protection of human subjects, the investigator(s) adhered to policies of applicable Federal Law 45 CFR 46.

____ In conducting research utilizing recombinant DNA technology, the investigator(s) adhered to current guidelines promulgated by the National Institutes of Health.

____ In the conduct of research utilizing recombinant DNA, the investigator(s) adhered to the NIH Guidelines for Research Involving Recombinant DNA Molecules.

____ In the conduct of research involving hazardous organisms, the investigator(s) adhered to the CDC-NIH Guide for Biosafety in Microbiological and Biomedical Laboratories.

J.M. Reid / A.P. 8/29/96

PI - Signature Date

Contents

5 INTRODUCTION

5.1 Nature of the problem

The potential benefits of early diagnosis of cancer were recognized many years ago, before soft tissue imaging was available. This goal was behind the first efforts to apply ultrasound to the problem of the detection/diagnosis of breast cancer. Since then, many investigators have devoted effort to this problem because of the known advantages of ultrasound: it is non-ionizing, relatively inexpensive and uses widely available, portable, equipment. Today, with the success of x-ray mammography as an early screening tool, there is still room for improved methods, since there is disagreement regarding the use of ionizing radiation for screening, or routine exams. Also, the fibrous tissue of dense breasts gives poor results in conventional mammograms.

Ultrasound is now available as an adjunctive modality in many breast clinics, where it is used to determine if masses with smooth borders are cystic or solid and to examine dense young breasts. Biopsy is still used often to determine malignancy. The cystic/solid determination can be a problem in borderline cases, because of the tendency of some ultrasonic systems to "fill in" the echo free space with artifactual echoes and thus make a cyst appear to be solid. There is a need for better ultrasound systems, as well as to have a more general-purpose imaging modality available than the x-ray, particularly if this modality had the advantages listed for ultrasound.

Several factors have been identified in the literature as those contributing to poor resolution of ultrasound images. In B-Scan images, finite signal bandwidth of the ultrasonic transducers is a major reason for low resolution in the temporal axis, whereas the non negligible beam width highly contributes to that in the lateral direction [18], [7], [14], [44], [21]. The resolution also depends on the frequency at which the imaging system operates. In addition to equipment limitations, there are factors originating from the nature of the tissue being imaged. Phase aberrations and velocity variations arising from acoustic inhomogeneity of tissues are two of the important causes, not only for low resolution but also for low contrast in images [39], [11], [6]. The observed ultrasonic image can, therefore, be considered as a distorted version of the true tissue image, where the axial distortion is dominated by the pulse-echo wavelet of the imaging system and the lateral distortion by the lateral beam profile.

5.2 Background of previous work

The problem of compensating for imaging distortions has been very active research area, underscoring the importance in improving diagnostic quality of ultrasonic images. There have been several approaches to cancel out the aberration effects, but there is no consensus as to the best way to achieve it [10], [26], [25], [38]. In [10] it was proposed estimating the differences in arrival times between two adjacent receiving element locations using cross correlation techniques; these results were used to modify phasing characteristics of the transducers for ensuing scans. In [25], using an idea adapted from optics, phasing characteristics were determined using speckle brightness as a measure of image quality.

The availability of convolution models, such as in [17], [9], for ultrasound image formation and the wide availability of digital computers has given an added importance to discrete-time deconvolution methods, as a means of improving images beyond the capabilities of hardware. A few researchers have investigated the true 2-D deconvolution of RF images [9], [18], [32], whereas most of the published works are on 1-D techniques [44], [21], [23], [19], [14].

Since the resolution along the lateral direction was much worse than that along the temporal axis, a number of attempts were focussed on deconvolution of lateral image lines. In [44], a B-mode image was considered to be an ensemble of lateral lines corresponding to lateral slices through the envelope detected image, at given times (depth). Observing that the point-spread function of a typical pulse-echo imaging system is highly elongated along the lateral direction, they hypothesized that lateral image lines can be approximately described by a 1-D convolution model. Their model consisted of two 1-D terms: a signal of interest called the tissue reflectance and a blurring kernel in the lateral direction called the lateral point spread function. The latter function was defined to be the laterally varying component of the 2-D point spread function, whose axial variation had been approximated by a Dirac delta function. The problem of resolution enhancement was posed as one of extracting the the tissue reflectance from the observed image, assuming a *perfect knowledge* of the lateral point spread function. Using a Gaussian shaped hypothetical lateral point spread function, it was shown that at the best signal to noise ratio that can be expected from ultrasound images, deconvolution will lead to a resolution enhancement of no better than 2.0. The definition of the resolution was based on the reciprocal of the effective width of the lateral point spread function. However, the amount of improvement was also reported to be dependent on the exact shape of the lateral point spread function. These figures were found to be in agreement with the empirical numbers reported in [14]. Several others have reported results on 1-D lateral deconvolution [43], [33], [21] , where in [33] it was concluded

that the computational effort on lateral deconvolution was wasted because of the very low resolution enhancement they could obtain at the expense of introducing more artifacts.

The drawbacks of the lateral deconvolution techniques discussed above are the following. Although the quantity displayed on an ultrasound imager is the envelope of the received RF signal, the image formation process actually occurs in the RF domain. In [32] it is pointed out that in general the convolutional model of image formation in the RF domain does not hold for envelope detected signals. It is concluded that the 1-D lateral deconvolution on envelope succeeds only in the special case where no phase interference from nearby reflectors is present.

All the papers, except [21], on lateral deconvolution mentioned above, relied on measuring the lateral beam profile to be used in computations. To obtain the true tissue image from the distorted observation, one requires quantitative information on the complex beam shape and acoustic velocity variations in-vivo, which are impossible to measure directly. In highly simplified situations such as measurements of wire targets under water, it is possible to get that information reliably. However, in the case of in-vivo tissue targets, such information is generally unavailable. The measurements done under water are not valid with clinical images, even when the imaging system used is the same, because of the effects of phase aberrations, nonlinearities and dispersive attenuation introduced by the tissues [21], [11], [39] , [6]. thus dramatically limiting the clinical applicability of those methods.

In [21], a line-by-line lateral deconvolution technique which does not require the complex beam shape in tissue or phase information on adjacent lateral lines, was proposed. This method too, however, worked on amplitude detected B-scan images. It hinges on the key assumption that the transfer function of the imaging system along a lateral image line can be approximated by the smoothed Fourier transform of the lateral image line itself. A convolution relationship between the envelope of a lateral point spread function and a slowly varying envelope of the tissue response has been tacitly assumed. Thus this method is subject to all the limitations implied by the above assumptions.

In spite of the fact that temporal resolution in an ultrasound image is much higher than the lateral resolution, axial deconvolution is still of importance. Besides the obvious advantage in improved axial resolution, the removal of the effect of the ultrasound pulse echo wavelet (through axial deconvolution) will tend to make the appearance of images more uniform over different subjects [16], thus simplifying the diagnosis procedures. As the shape of the pulse echo wavelet changes with propagation due to dispersive attenuation, a first step in axial deconvolution often involves the estimation of the pulse in tissue. Parametric modeling of speckle-only image lines has been proposed [37], [20], [16]. However, such approaches are limited by the problems such as the model order selection, associated with

parametric modeling. In [19] a Kalman filter technique was applied to estimate pulse echo wavelets as well as to simultaneously improve the axial resolution. The success of the method was reported to be dependent on the SNR of the observations and the accuracy at which the observations could be modeled. A non-parametric approach for the estimation of the pulse was proposed in [15], where the minimum-phase equivalent of the pulse-echo wavelet was separated from the tissue response. However, quite often pulse-echo wavelets and lateral kernels are non-minimum phase signals, thus limiting the generality of this approach.

5.3 Methods of approach

In the past year we introduced a novel non-parametric framework for deconvolution of B-scan images [1], [2], [3], [4], [5]. We first developed a model for the rf image, and then reconstructed distortions using higher-order statistics of the measured image lines. Based on the estimated distortions we performed deconvolution of the corresponding images and demonstrated that the resolution of ultrasound images of tissue mimicking phantom as well as human tissue images was significantly improved. In the past, estimation of distortions has been carried out using exclusively second order statistics (autocorrelation). Autocorrelation, however, can recover only the minimum phase quivalent of the true distortions, because it is blind to phase. We also estimated distortions using second order statistics of the image lines. We showed that although these estimates did lead to resolution improvement, the amount of improvement was less significant that the one obtained with the higher-order statistics based estimates.

Image formation process in the RF-domain is described by a 2-D convolutional model, where the attenuation of the pulse-echo wavelet and beam aberration effects can be indirectly incorporated [17], [18], [16]. Two 1-D blurring kernels, corresponding to axial and lateral directions, is hypothesized to represent distortions along respective axes. The axial distortion kernel includes the blurring effects due to the finite bandwidth of the transducer, and dispersive attenuation of the pulse-echo wavelet in tissue. The lateral distortion kernel represents the convolutional components of lateral blurring due to the complex beam patterns. Formalizing a definition for resolution, we show that compensation for the effects of the blurring kernels improves the resolution of the image.

The proposed method has the advantage of being able to estimate these kernels at each image line, axial and lateral, thus capturing the variations within the image. Since the estimations are based on higher-order statistics [24] of RF-data, the estimated kernels are robust to additive observation noise and also have correct phase. To the best of our

knowledge, *the method we proposed [1] is the first one to in-vivo estimate the distortion kernels with their true phase, as opposed to conventional methods that estimate minimum-phase equivalent of kernels.*

6 BODY

6.1 Modeling the rf image

During an ultrasonic investigation, a three-dimensional pulsed pressure field is emitted into the tissue. The field interacts with the tissue and part of it is reflected, scattered, and subsequently received by the transducer. Under the assumptions of linear propagation and weak scattering, an expression for the received pressure field was derived in [17], using the first order Born approximation. Absorption effects were neglected. The equation has been expressed as a convolutional model in the following form:

$$y(\mathbf{r}_2, t) = v_{pe}(t) *_t f(\mathbf{r}_1) *_r h_{pe}(\mathbf{r}_1, \mathbf{r}_2, t) + w(\mathbf{r}_2, t), \tag{1}$$

where:

• $\mathbf{r_1}$, $\mathbf{r_2}$ are vectors denoting the location of the scatterer and the transducer, respectively;

• " $*_t$ " and "$*''_r$ denote time and spatial convolution, respectively;

• $f(\mathbf{r}_1)$ originates from the inhomogeneities in the tissue due to density and propagation velocity perturbations above their mean levels, giving rise to the back scattered signal (*tissue response*).;

• $v_{pe}(t)$ is the pulse-echo wavelet that accounts for the transducer excitation and the impulse responses during emission and reception of the pulse;

• $h_{pe}(\mathbf{r}_1, \mathbf{r}_2, t)$is the modified pulse-echo spatial impulse response that relates the transducer geometry and the spatial extend of the scattered field. The computation of $h_{pe}(\mathbf{r}_1, \mathbf{r}_2, t)$ is based on the approach described in [41], [35]. Convolutional components of aberrations and dispersive attenuation, which introduce spatially varying effects to the process, may be incorporated in this already spatially varying kernel.

• $w(\mathbf{r}_2, t)$ represents measurement noise and the unmodeled dynamics of the image formation process.

The problem of extracting the tissue response $f(\mathbf{r}_1)$ from the observation $y(\mathbf{r}_2, t)$ is a deconvolution problem. Since a B-mode image is a mapping from the 3-D tissue space to the 2-D space of the display, the solution is not unique in general. This non-uniqueness should be obviated by making reasonable assumptions about the 3-D structure of the tissues being imaged [9]. An assumption implicit in cases where the deconvolution is done using

kernels confined to the imaging plane is that all image features in the imaging-plane extend perpendicular to the corresponding plane in the tissue space, so as to make the height of extension the effective height of the beam.

The convolution model of (19) expresses the fact that the received signal at the transducer site $\mathbf{r}_2$ is a result of linear spatio-temporal interaction between the signal of interest $f(\mathbf{r}_1)$ and a distortion kernel. Thus, the measured signal contains a distorted version of the true tissue response $f(\mathbf{r}_1)$. Deconvolving these kernels should improve image resolution and contrast. It should also remove aberration-induced artifacts that result from changing beam profiles inside the tissue.

As discussed in the introduction, efforts to carry out this deconvolution have been hampered by the difficulties in measuring the modified spatial impulse response of the imaging system. Underwater measurements using simplified targets would not reveal any significant changes undergone by the interrogating beam in tissue.

Our goal here is actually to identify the combination of $v_{pe}(t)$ and the spatially varying kernel $h_{pe}(\mathbf{r}_1, \mathbf{r}_2, t)$, and subsequently cancel it from the image in order to improve lateral as well as axial resolution. Let us combine both smoothing kernels $v_{pe}(t)$ and $h_{pe}(\mathbf{r}_1, \mathbf{r}_2, t)$ in one spatially and temporally varying kernel, $h(\mathbf{r}_1, \mathbf{r}_2, t)$, which we are going to refer to as the *ultrasonic system impulse response*. For discrete time, and for some fixed transducer location (19) is equivalent to the following two-dimensional convolutional model

$$y(l,n) = \sum_i \sum_j f(i,j)h(l-i, n-j) + w(l,n), \tag{2}$$

where $y(l,n)$ represents the sample from the $l-$th A-line at discrete time n. The goal here is to identify the time varying ultrasonic system response $h(l,n)$, and recover the tissue response, $f(i,j)$, from the noisy measurement $y(k,l)$.

However, we will not attempt a true 2-D deconvolution in this paper. As is commonly done in ultrasound deconvolution literature [15], [23], [18], [19], we assume that an RF A-line can be expressed as a convolution between two 1-D axial terms: a hypothetical tissue response and a distortion kernel. This view is not unique to the image deconvolution literature; ultrasound Doppler systems and tissue attenuation estimation techniques tacitly depend on it [15]. Reducing the problem to a 1-D deconvolution is analogous to the original decomposition of the true 3-D deconvolution problem in to a 2-D one.

6.1.1 Assuming white tissue response: In vivo distortion estimation using higher-order statistics (HOS)

In the following we will treat each image line (either in ateral or axial direction) separately assuming the 1-D model

$$y_i(n) = h_i(n) * f_i(n) + w_i(n),\ i = 1, 2, ..., \tag{3}$$

where i is the A-line index; $f_i(n)$ is the axial or lateral tissue response; $h_i(n)$ is the axial or lateral distortion kernel; which describes the distortion associated with the i-th line; and n denotes discrete time. We assumed that:

(A1) $h_i(n)$ is deterministic, possibly non-minimum phase,

(A2) $f_i(n)$ is stationary, white, independent identically distributed (i.i.d.), zero-mean non-Gaussian,

(A3) $w_i(n)$ is white zero-mean Gaussian, and independent of $f_i(n)$.

If we consider a region of the image that contains speckle only, these assumptions should hold reasonably well. In an image that contains inhomogeneities, however, the whiteness assumption about $f_i(n)$ will not be valid.

The third order cumulant of the observation $y_i(n)$ is defined as [24] :

$$c_{y_i}(\tau, \rho) = E\{y_i(n)y_i(n+\tau)y_i(n+\rho)\} \tag{4}$$

The bispectrum of the $y_i(n)$ is defined to be the Fourier transform of the third order cumulant. Under assumptions $(A1) - (A3)$, the bispectrum of $y_i(n)$ is given by [24]:

$$C_{y_i}(\omega_1, \omega_2) = C_{f_i}(\omega_1, \omega_2)H_i(\omega_1)H_i(\omega_2)H_i^*(\omega_1 + \omega_2) + C_{w_i}(\omega_1, \omega_2) \tag{5}$$

where $C_{f_i}(\omega_1, \omega_2)$ is the bispectrum of $f_i(n)$, $H_i(\omega)$ is the spectrum of $h_i(n)$ and $C_{w_i}(\omega_1, \omega_2)$ is the noise bispectrum. If the additive noise is zero-mean Gaussian, then $C_{w_i}(\omega_1, \omega_2) = 0$ [24] and (4) becomes,

$$C_{y_i}(\omega_1, \omega_2) = C_{f_i}(\omega_1, \omega_2)H_i(\omega_1)H_i(\omega_2)H_i^*(\omega_1 + \omega_2) \tag{6}$$

The bicepstrum is defined as the cepstrum of the bispectrum, from which we get:

$$b_{y_i}(m_1, m_2) = b_{f_i}(m_1, m_2) + c_{h_i}(m_1, m_2), \tag{7}$$

where $b_{f_i}(m_1, m_2)$, $c_{h_i}(m_1, m_2)$ are the bicepstra of $f_i(n)$ and $h_i(n)$, respectively.

If $f_i(n)$ is stationary independent identically distributed (i.i.d.), its third order spectrum is flat and equal to the skewness, γ_{f_i}, of the process. Therefore, its bicepstrum will be an impulse located at the origin. In that case, using bicepstral values along the main axes except at the origin, we can reconstruct a scaled and shifted version of $h_i(n)$ as:

$$h_i(n) = F^{-1}\{e^{F\{c_{h_i}(m)\}}\}, \tag{8}$$

where

$$c_{h_i}(m) = \begin{cases} b_{y_i}(m,0) & m > 0 \\ 0 & m = 0 \\ b_{y_i}(-m,0) & m < 0. \end{cases} \tag{9}$$

We assume that a similar 1-D model holds in the lateral direction of the RF-image. Then, a similar procedure can be followed to estimate lateral distortion kernels at each line. The kernels thus estimated will include the convolutional components of aberration as well. Therefore, axial deconvolution followed by lateral deconvolution, or various combinations thereof, should give us distortion compensated RF images which will have higher resolution and contrast. The ability to estimate and remove beam distortion effects (due to aberration) is seen as a major advantage of this method over other non-parametric techniques [15], [21]. The method proposed in [15], as is, can not estimate non-minimum phase signals, while that of [21] has been designed for envelope detected signals.

6.1.2 Assuming non-white tissue response: In vivo distortion estimation using HOS

As it was already mentioned the tissue response $f_i(n)$ will be non-white if variations in tissue structure occur. A detailed study of this case can be found in [2] (see also Appendix A). The most common way to model a non-white process is consider it as the convolution of a white noise term with a deterministic kernel. This kernel is referred to as the "color" of the process. It describes the correlation between the samples of the process, and can be used as an indication of the the deviation of the process from whiteness.

If the process described in the previous Section is applied when the tissue response is nonwhite, the distortions reconstructed from each image line will contain as convolutional component the color of the tissue response. These distortions will be referred to as "combined kernels".

Combined distortion kernels $k_i(n)$ and $k_j(n)$ obtained at two different but closely spaced lines "i" and "j", can be written as:

$$k_i(n) = h(n) * t_i(n) \tag{10}$$

$$k_j(n) = h(n) * t_j(n) \tag{11}$$

where $h(n)$ denotes the true distortion kernel, which is assumed to be invariant between the two locations "i" and "j"; $t_i(n)$ and $t_j(n)$ respectively represent the color of the tissue responses at "i" and "j".

The true distortion $h(n)$ and the colors $t_i(n)$, $t_j(n)$ can be computed via the blind deconvolution method presented in [31].

6.1.3 Assuming white tissue response: In vivo estimation of the minimum phase equivalent of distortion using second-order statistics (SOS)

Using the model of eq. (3), second order statistics were also used to estimate imaging distortions [12], [13].

Transforming (3) in the autocorrelation domain (second-order statistic) we get:

$$r_{y_i}(\tau) = E\{y_i(n)y_i(n+\tau)\} = \gamma_2^{f_i} \sum_n h_i(n)h_i(n+\tau) + \gamma_2^{w_i}\delta(\tau), \tag{12}$$

where $\gamma_2^{f_i}$ is the variance of $f_i(n)$, $\gamma_2^{w_i}$ is the variance of the noise, and $\delta(\tau)$ is the unit impulse. The power cepstrum is defined as the inverse Fourier transform of the logarithm of the Fourier transform of the autocorrelation. Assuming that the noise level is low enough, in the power cepstrum domain we get:

$$\hat{y}_i(k) \sim \hat{h}_i(k), \quad k \neq 0, \tag{13}$$

where $\hat{h}_i(k)$ is the power cepstrum of the distortion kernel associated with the $i-$th line. From its power cepstrum, we can reconstruct the minimum phase equivalent of $h_i(n)$ [27] as:

$$\tilde{h}_i(n) = F^{-1}[exp\{F[\hat{y}_i(k)w(k)]\}], \tag{14}$$

where $F[.]$ and $F^{-1}[.]$ denote forward and inverse Fourier transforms, and

$$w(k) = \begin{cases} 1, & k > 0 \\ 0, & otherwise. \end{cases} \tag{15}$$

6.2 Experiments

The goals of our experimental work were to:

1. Compare the axial distortions, estimated based on higher-order statistics (HOS-based distort ions), with experimentally obtained ones. Validate the imposeed assumptions.

2. Estimate HOS-based distortions from clinical ultrasound images. Deconvolve ultrasound images using the HOS-based estimated distortions based on the whiteness assumptions about the tissue response (see Section 6.1.1). Quantify resolution improvement.

3. Estimate HOS-based distortions from clinical ultrasound images. Deconvolve ultrasound images using the HOS-based estimated distortions based on the non-whiteness assumptions about the tissue response (see Section 6.1.2). Quantify resolution improvement. Determine if there is any difference in the final deconvolution result depending on the assumption about the whiteness and non-whiteness of the tissue response.

4. Deconvolve clinical images using distortions estimated based on second-order statistics (SOS-based distortions) as outlined in Section 6.1.3). Quantify resolution improvement.

5. Compare resolution improvement of deconvolution with HOS-based and SOS-based distortions.

Towards the above goals we collected the following data:

- Water-tank measurements:

  Experiment A

  We obtained B-Scan images of an ATS model 532 contrast resolution phantom which was positioned in a water tank. The target area consisted of the tissue mimicking background which had a scatterer density of 32 scatterers/mm^3. The transducer we used was a model GE104682 curved device with a nominal center frequency of 3.5 MHz. The nominal focal zone of the transducer was 6-13 cm. A stepper motor with a step size $0.025mm$ controlled the position of the transducer under the guidance of a personal computer. Data acquisition was done through a LeCroy model 9450A dual channel digital oscilloscope connected to the PC by a GPIB interface. Transducer was moved across the scanning plane in steps of $0.25mm$, and RF echos were sampled at a 13.3 MHz rate.

  Experiment B

  A long piece of freshly peeled wire of diameter $0.812mm$ was placed underwater so that it was parallel to the transducer surface and perpendicular to the scanning plane. It was kept inside the focal zone of the transducer, at a distance

$8cm$ away from the transducer surface. The experimental setup used here is the same as in *experiment (A)*. The wavelet reflected from the wire surface was recorded and taken to be an approximate estimate of the pulse-echo wavelet of the imaging system.

- Measurements from Clinical Equipment:

Experiment C

To demonstrate the performance of our method on data from more realistic equipment, we imaged the same ATS532 phantom using a linear array sector scan transducer on a model UltraMark-9 clinical imaging system manufactured by Advanced Technology Laboratories, Seattle, U.S.A. The target area consisted of two cylinders with scatterer densities 4 and 8 scatterers/mm^3, embedded in a tissue mimicking background of 32 scatterers/mm^3. The nominal center frequency of the scanner was 3.5 MHz; the field of vision was 60^0. Data were sampled at a rate of 12 MHz. No TGC was employed.

Experiment D

To demonstrate the performance of our method under clinical conditions, we obtained liver scans of patients imaged by ultrasonologists at the Thomas Jefferson University Hospital, Philadelphia, on the same imaging system described under *experiment (C)*. The patients have been diagnosed with hypoechoic multiple liver metastatic tumors. No T.G.C. had been applied; focus of the imaging system at transmission was set at $2cm$, and dynamic focusing was employed with the receiving mode.

Experiment E

Clinical breast data consists of ultrasound images acquired by radiologists, from patients referred to the Department of Radiology, Thomas Jefferson Universi ty Hospital, Philadelphia 19107. The imaging system was an Ultramark 9 HDI system with RF data acquisition capabilities, provided to Thomas Jefferson University Hospital by Advanced Technology Laboratories. A flat, linear array transducer of center frequency 7.5 MHz was used to collect data (RF-echoes). The sampling rate of the data acquisition system was at 20 MHz. Five breast images (denoted as *Patient 1- Patient 5*) with tumors in them are considered here.

6.3 Results

6.3.1 Water-tank experiments and the accuracy of our estimation method

In order to demonstrate the validity of our kernel estimation procedure, we used the data from underwater measurements, i.e. *experiments (A) and (B).* A part of the RF image data that we gathered using the circular transducer in *experiment (A)* is shown in Fig. 1(a), where the logarithm of the envelope has been used for display purposes.

Under the assumption that the axial blurring kernel of an image line does not significantly depend on the lateral location of the line, data from several nearby axial RF lines can be used to make a longer data vector, which will enable us to obtain better cumulant estimates. In order to minimize the effect of attenuation on our estimations, from each A-line i we considered data segments $y_i(k)$ of length not more than $2N$ samples. The number of adjacent line segments $y_i(k)$ concatenated was in the range $i = 1 - 10$. In the axial kernel estimations, we used $M = 10$ and $N = 64$.

Axial blurring kernels estimated with the method of Section 6.1.1 from different regions of the image in Fig 1(a) are shown in Fig. 2(a), in dotted lines. All of these kernels have been estimated from axial data obtained at the *same depths* of the image, but at different lateral locations. The mean axial blurring kernel, $v_m(t)$, which was computed as the average of estimated kernels, is indicated by the solid line while the measured pulse echo wavelet is indicated by the dashed line.

It can be seen that all of the estimated kernels possess a similar structure, resembling a typical ultrasound pulse-echo wavelet. This is to be expected since the component due to the pulse-echo-wavelet ($v_{pe}(t)$) dominates the axial blurring kernel [18]. The variation among the estimated kernels may be attributed to the statistical estimation errors, deviation of the scatterer response from a statistically white response (which violates our assumption (A2)) and, contributions from the effects of the medium such as aberration and dispersive attenuation which have spatially varying characteristics.

There is a reasonable match between the measured and average estimated kernels (Fig. 2), *within the limits of the accuracy of the experimentation.* Looking at their spectra (see Fig. 2(b)) we can clearly see that the frequency spectrum of the estimated mean kernel has the salient features contained in the experimental pulse echo wavelet measured in *experiment (B).* The center frequency of the spectra fall very close to the nominal center frequency of the transducer, 3.5 MHz. The measured wavelet has a slightly narrower main lobe, probably due to the ringing introduced by the wire target used in *experiment (B).* However, it should be kept in mind that the measured kernel was obtained from simplified underwater experiments, which do not truly represent the situation inside the

tissue mimicking phantom.

The differences between the average estimated kernel and the measured kernel can be attributed to:

(E1) the variance associated with the estimation of third order cumulants,

(E2) the much higher dispersive attenuation and aberrations encountered inside the phantom in *experiment (A)*, compared with those in *experiment (B)*,

(E3) the non-whiteness of the underlying scatter response of the phantom that violates assumption (A2),

(E4) approximate realization of a point target by a line target, in *experiment (B)*.

Averaging techniques that we used with both the cumulant estimates of observations and estimated kernels themselves, make the contributions to total error from (E1) small. The errors introduced by approximating a point target by a thin wire target does not introduce serious errors either; this method is being used in the testing of ultrasound transducers in research environments, [32], [21].

The major contribution to the differences in estimated and measured kernels are from $(E2)$ and $(E3)$. In fact, by virtue of modifying the frequency spectrum of the received signal, attenuations appear as one component contributing to the non-whiteness (color) of the scatterer response, and thereby affects the kernel estimation procedure. To minimize the effect of attenuations on the stationarity of our observations, we considered only short segments (eg. 64 or 128 samples at a 13.3MHz sampling rate) from each A-line of interest. Identifying and compensating for the color of the tissue response can be achieved by applying the blind deconvolution procedure proposed in [31] on different image lines [2].

The results we obtained support our model assumptions $(A1)-(A3)$. It should be noted that (A2) actually contradicts the Gaussianity assumption, which is commonly made for the tissue response. However, non Gaussian models for the backscattered ultrasonic signals have been suggested and used in the past [42], [34], [29], [30]. In the method proposed here, if the tissue response were Gaussian, it would have been suppressed in the bispectrum domain, thereby rendering the estimation of an axial blurring kernel an impossibility. Hence, our success in the estimation supports the non Gaussianity assumption for RF ultrasound data. The structure of the measured kernel (*experiment (B)*) suggest that the axial kernel is indeed a non-minimum phase signal; the method proposed in this paper is capable of estimating non-minimum phase signals in contrast to existing techniques which can only estimate the minimum-phase equivalent of the true non-minimum phase signal.

We consider the agreement between the estimated and measured kernels satisfactory *within the ability of underwater measurements (Measurement B) to match the situation inside the phantom.*

6.3.2 HOS-based distortion estimation and the deconvolution of B-mode images assuming white tissue response (phantom data, human liver, human breast)

A. Images of a tissue mimicking phantom obtained with a single element transducer.
Having established the validity of our assumptions and the kernel estimation technique in the axial direction, we proceeded to estimate lateral distortion kernels from the image obtained in *experiment (A)*, and to perform deconvolution. The lateral distortion kernels we estimated at locations covering a range of depths $6.58cm$-$9.42cm$ from the transducer surface can be seen in Fig. 3(a); their spectra are shown in Fig. 3(b). In these estimations, we used $N = 32$ and $M = 10$. Five adjacent lateral lines were used in each kernel estimation.

In the lateral direction, the estimated kernels have characteristics similar to the lateral beam profiles of the imaging system. Unfortunately, there is no direct way to verify the results of our lateral estimations. In conventional transverse beam profile estimations, the experiments are usually done under water, and the pressure profiles are peak detected. This process masks instantaneous features of the beam, hence the results of such experiments can not be used in a verification. Moreover, it has been shown that in the presence of aberration, the lateral point spread function may undergo significant modifications [6], [39], possibly serious enough to change diagnoses in clinical situations [39]. Time histories of two dimensional instantaneous beam profiles at the focus, shown in [22], are in agreement with the observation that the lateral beam profile can depart heavily from the ideal in the presence of tissue inhomogeneities. These results suggest that, in principle, underwater experiments or theoretical formulae that do not take aberration in to account, can not be used in verifying lateral blurring kernels estimated from complex targets. Further, it should be noted that even though our lateral kernels are estimated at individual lateral image lines (i.e., at a fixed time) nearby lines contribute to the data at a given time by virtue of the spatio-temporal nature of Ultrasonic System Impulse Response defined earlier.

Once the distortion kernels have been identified, retrieving the corresponding true tissue response becomes a typical deconvolution process. For the deconvolution, we used the constrained Wiener filter technique described in [40]. In performing the axial deconvolution, we used the mean HOS-based axial distortion kernel, $v_m(t)$ shown in Fig. 2., which was obtained with the method of Section 6.1.1; in the lateral direction, the mean lateral

distortion kernel obtained as the average of the estimated kernels shown in Fig. 3 was used.

Fig. 1(b) shows the logarithmically compressed envelope of the B-scan image, derived from the laterally deconvolved RF data corresponding to the original image shown in Fig. 1(a). The axially deconvolved image is in Fig. 1(c) and the laterally followed by axially deconvolved image is in Fig. 1(d). Each image represents an area of $2.5cm$X$2.0cm$ in the true tissue space. For the sake of computational simplicity, we assumed that the lateral (and axial) blurring kernel do not vary significantly over different RF-image lines or different image depths in the amounts we are concerned with here. This allowed us to use a single blurring kernel, in each of the axial and lateral directions, to deconvolve the entire image. Using the average lateral kernel to laterally deconvolve a region of the image is justifiable by the fact that all the kernels estimated from the depth range covering the image shown here ($6.58cm$ to $9.42cm$) show a certain degree of similarity. This may be due to the fact that the transducer we used had a focal zone of 6-$13cm$, into which range the lateral image lines considered above belong. Moreover, the phantom we used in experiments had not been designed to simulate strong aberrating effects. As for the axial deconvolutions, the pulse echo wavelet (the major contributor to the axial distortion kernel) of the imaging system is known to stay fairly constant over different RF-lines across the image [18], [16]; our results shown in Fig. 2 also support that hypothesis. However, the method proposed here is still valid, if one needs to estimate kernels for localized regions or individual image lines. To capture fine details in the pass band of the spectrum, one may still require a line by line, or region by region, lateral deconvolution.

Quantifying resolution improvement

According to Fig. 1, the deconvolution in the RF-domain results in a significant reduction in the size of speckles, suggesting a gain in resolution. In order to quantify the apparent increase in resolution, we defined a measure of resolution based on the 2-D auto-covariance function of the image. Auto-covariance function of an image was computed on the *RF data* corresponding to the image, with the peak value of autocovariance normalized to 1.0. The lateral slice, L_{00}, through the peak of the 2-D auto-covariance function was considered in defining the *lateral resolution.* The axial slice, A_{00}, through the peak in defining the *axial resolution.* Similarly, the lateral resolution, $R_d^{(l)}$, was defined as the reciprocal of the width of L_{00}, at d dB below the peak of the slice. Axial resolution was defined similarly except for the fact that the envelope of the absolute value of the slice A_{00} was used. In this paper we used $d = 5.00$ and $d = 10.00$. Defining the resolution at two different dB levels allows us to get a better idea of the shape of the auto-covariance function.

The reason for defining the axial resolution based on the envelope of absolute value of

A_{00} is as follows. We define the resolution in terms of the width, l_0, of the *main lobe* of the auto-covariance function because, l_0 is a measure of the average "smallness" of the basic building elements of the image. In the axial direction, the representation of a point target is an oscillatory, time-limited signal. Therefore, even when the target is a point in space, the received signal would have an auto-covariance function which shows oscillatory behavior (eg. Fig. 4(d)). In this case, the central lobe conveying information on the average image element size is the envelope of the absolute value of the auto-covariance function.

The resolution was defined in the RF domain, because our kernel estimation and deconvolution procedure was done entirely in the RF-domain. The process of envelope detecting itself introduces blurring leading to an inaccurate estimate of the potential resolution delivered by deconvolution, thus making the envelope detected signal domain a less than ideal place to define resolution. Fig. 4(a) shows a 2D shaded mesh plot of the auto-covariance function of the RF-data corresponding to original image in Fig. 1(a). Fig. 4(b) shows the auto-variance function after lateral and axial deconvolutions. Absolute values of the auto-covariance function have been plotted for easy visualization. The slice L_{00} is shown in Fig. 4(c), where the solid line indicates the slice corresponding to the original image (Fig. 1(a)) and the dotted line that of the laterally and axially deconvolved image (Fig. 1(c)). Corresponding plots of the axial slice A_{00} are in Fig. 4(d).

The general decrease, in all directions, of the width of the main-lobe of the auto-covariance function due to deconvolution is obvious from Figs. 4(a) and 4(b). From Fig. 4(c), we computed the *lateral resolution gain*, G_d^l, defined as:

$$G_d^{(l)} = \frac{R_d^{(l_o)}}{R_d^{(l_d)}}, \quad d = 5dB, 10dB, \tag{16}$$

where $R_d^{(l_o)}$ and $R_d^{(l_d)}$ respectively represent lateral resolutions before and after deconvolution. A similar definition holds for the *axial resolution gain*. The lateral resolution gain at $d = 5dB$ and $d = 10dB$ levels, between the original (Fig. 4(a)) and the laterally followed by axially deconvolved image (Fig. 4(c)) was found to be 2.7 and 3.0 respectively. The corresponding figures for axial resolution gain, $G_d^{(a)}$, was 1.73 and 1.72 respectively.

Our results indicate that the lateral resolution gain is higher than the axial resolution gain. Coupled with the fact that, in the original image blurring was much higher in the lateral direction, we can conclude lateral deconvolution is mostly responsible for the improvement in overall resolution.

To investigate the effects of deconvolution on "speckle noise" levels, we defined the signal-to-noise ratio as, $SNR = (\frac{\mu}{\sigma})$, where μ is the mean of the image and σ^2 is the variance. Since we performed our deconvolutions in the RF domain, our SNR calculations were also

done in the RF-domain, on absolute values of RF-data. Computed over the original image (Fig. 1(a)), $SNR = 1.24$; computed over the laterally and axially deconvolved image, $SNR = 1.26$. After only an axial deconvolution, (Fig. 1(c)), $SNR = 1.25$, and after only a lateral deconvolution (Fig. 1(b)), $SNR = 1.23$. Based on these numbers, we conclude that the deconvolution results in a gain in resolution, but does not significantly alter speckle noise levels. The results of SNR computations and resolution gains have been summarized in Tables 1 and 2.

B. Images of a tissue mimicking phantom obtained with clinical equipment

In order to investigate the performance of our technique with B-scan images taken from modern clinical equipment, we estimated axial and lateral distortion kernels from the RF-data collected in *experiment (C)*. Fig. 5(a) shows the logarithmically compressed envelope of the original B-scan image. Average axial and lateral kernels estimated from the RF-data corresponding to Fig. 5(a) are illustrated in Fig. 6(a) and 6(b) respectively. These kernels indicate the average of 20 kernels estimated from the tissue mimicking background region of the phantom, between the two target cylinders (see Fig. 5). The spectra of the average axial kernel is shown in Fig. 6(c) and that of the average lateral kernel in Fig. 6(d).

The result of lateral deconvolution is shown in Fig. 5(b); the result of lateral followed by axial deconvolution is shown in Fig. 5(c). Average estimated kernels shown in Fig. 6 were used in both axial and lateral deconvolutions. Clearly, the deconvolution has resulted in a reduced speckle size and cleaner, better defined boundaries of the target cylinders. It is also evident that the attenuations associated with the imaging process show up much clearly in the deconvolved image. This may have significance in clinical imaging situations, where attenuation properties of tissue convey important diagnostic information.

Fig. 7(a) and 7(b) illustrate the absolute value of the auto-covariance function of the RF-data corresponding to the original (Fig. 7(a)) image and the laterally and axially deconvolved image (Fig. 7(d)), respectively. Fig. 7(c) and 7(d) show the lateral and axial slices L_{00} and A_{00} used to compute resolution gains. Based on data corresponding to Figs. 5 and 7, speckle SNR and resolution gains were computed and tabulated in Tables 1 and 2. Figs. 5, 7 and Tables 1 and 2 lead to the conclusion that considerable resolution enhancement is possible with deconvolution, and that the process of deconvolution does not affect the speckle noise significantly. Once again, lateral resolution is found to be mostly responsible for the overall improvement in the image.

C. Clinical images of a human liver

To evaluate our method with clinical images, we obtained a B-scan of a liver image as

described in *experiment (D)*, section 3.1. Figure 8(a) shows a part of the logarithmically compressed envelope of the original image. Fig 9(a) and 9(b) show the average axial and lateral distortions estimated from the RF-data corresponding to Fig. 8(a). Their spectra can be seen in Figs. 9(c) and 9(d).

The results of lateral deconvolution is shown in Fig. 8(b); results of lateral followed by axial is in Fig. 8(c). In all cases, logarithmically compressed envelope of the images has been displayed.

Again, to visualize the improvement in resolution, we plotted the auto-covariances of the original and deconvolved images. Fig. 10(a) and 10(b) illustrates the shaded 2-D mesh plot of the auto-covariances of RF-data corresponding to Figs. 8(a) and 8(c) respectively. Corresponding L_{00} and A_{00} slices are shown in Figs. 10(c) and 10(d). Slices corresponding to original image are shown in solid lines, whereas those of the deconvolved image are shown in dotted lines.

The lateral resolution gain, $G_d^{(a)}$ at $d = 5dB$ and $d = 10dB$ was found to be 3.0 and 2.5 respectively. Corresponding numbers for the axial resolution gain were 1.7 and 1.5. Speckle SNR ratio computed for the original image (Fig. 8(a)) was $SNR = 1.20$; after lateral and axial deconvolutions (Fig. 8(c)) $SNR = 1.33$. Tables 1 and 2 summarize these results.

These results suggest that considerable gain in resolution is possible with axial and lateral deconvolution of clinical images.

Clinical ultrasound images of the breast

Results obtained in experiment E described in Section 6.2 are shown here.

Fig. 11(a) shows the B-scan breast image of Patient 1. The result of lateral followed by axial image deconvolution is shown in Fig. 11(b). In both cases, the logarithmically compressed envelope of the RF-data has been used for display purposes. Each image represents an axial depth of about 2.5 cm in the true tissue space.

According to Fig. 11, the deconvolution in the RF-domain has resulted in a significant reduction in the size of speckles, suggesting a gain in resolution. In order to quantify the apparent increase in resolution we computed the resolution gain for the image, before and after deconvolution. At the 10 dB and 5 dB levels, the resolution gains were found to be 2.0 and 2.6 (see Table 3). The deconvolution process lead an improvement in the image speckle SNR ratio, from $SNR = 0.68$ to 0.997 (see Table 3). These objective measures suggest that the deconvolution deconvolution process is capable of improving the resolution of breast ultrasound images without compromising the speckle SNR.

Similar results for the breast images of *Patients 2-5* are shown in Figs. 11 to 15 and Tables 3,4. All these results consistently point to the fact that the deconvolution leads to an improvement in the resolution.

However, the real improvement/deterioration due to deconvolution can be fully appreciated only by trained end users, i.e. radiologists, who make diagnostic decisions based on the images. As a preliminary means of obtaining the radiologists response, we showed the original and deconvolved images to a radiologist at the Breast Imaging Center of the Thomas Jefferson University Hospital, Philadelphia. The responses are as follows:

- The radiologist consistently preferred the deconvolved images over the unprocessed ones in all the cases, on the grounds that finer details can be easier to perceive from the deconvolved image due to its smaller speckle sizes (fine-grainess).
- In the case of *Patient 1*, (see Fig. 11), the tumor (indicated by arrows in Fig. 11(a)) and its spread (boundaries) were easier to detect/determine from the deconvolved image.
- In the case of *Patient 3*, (see Fig. 13), the deconvolution resulted in a better visualization of the jaggerdness of the tumor boundary, disclosing tumor infiltration to surrounding tissue and probably suggesting the malignant nature of the tumor. This detail was not easily perceived in the unprocessed image.
- In the case of *Patient 4* , (see Fig. 14), the smooth nature of the boundary of the tumor has become very easy to perceive, compared with the unprocessed image. Smooth boundaries may suggest a benign tumor.
- In the case of *Patient 5* , (see Fig. 15), the finer details have become easier to perceive in the deconvolved image. More importantly, deconvolution resulted in one region (indicated by arrows) becoming a suspected area. It was not very easy to judge in the first image.
- Deconvolution, even though makes the image texture finer, does not lead to a dramatic change in the nature of clinical ultrasound images familiar to radiologists. As a result, it is not hard to get used to deconvolved images in diagnosis.
- It would be very useful if the deconvolution can be done real-time. One of the major advantages of medical ultrasound is its real-time in nature, which results in dynamic images conveying more information than a still picture scan.

Although these responses are preliminary, they are very positive and encourages one to conduct a systematic analysis into the advantages of image deconvolution in clinical diagnosis. This can be attempted ones a large number of images are available for comparison. A large number of radiologists should also be involved in the process.

6.3.3 HOS-based estimated distortions and deconvolution of B-mode images assuming non-white tissue response

To investigate the significance/implications of the whiteness assumption on the tissue response we attempted estimating lateral and axial kernels from a clinical B-scan image described in Section 6.2, *Experiment D.* A part of the image approximately $7cm$X$2cm$ in size (in true tissue space) and containing a hypoechoic metastasis of the liver, is shown in Fig. 16(a). Logarithm of the envelope has been used for display purposes.

Axial Distortion Kernels

Some typical examples of the combined axial kernels $k_i^a(n)$ estimated from the corresponding rf-image are shown in Fig. 17. In order to reduce the estimation variance we concatenated 3 adjacent rf A-lines in each case. The effect of non-stationarities was minimized by considering short segments of data, 128 samples in this case, from each A-line. The kernels shown here correspond to a region of approximately $12mm^2$, in the original tissue space. Figs. 18(a) and (b) show two examples of the kernels estimated from within the tumor, i.e. $k_{iI}(n)$, and Fig. 18(c) and (d) show two kernels estimated from outside the tumor, i.e. $k_{iO}(n)$. The corresponding spectra are illustrated in Fig. 19; the spectra of the rf A-lines used in estimating the kernels and those of the kernels themselves are respectively shown by dotted and solid lines.

Several observations are in order now: (a) Fig. 18 depicts that there is a good match between the spectra of combined kernels and corresponding rf data. Figs. 17(a) and(b) show that there is a similarity between combined kernels $k_{iO}^a(n)$ estimated outside the tumor; the same is true for combined kernels $k_{iI}^a(n)$ estimated inside the tumor, and (c) $k_{iO}^a(n)$ are slightly different from $k_{iI}^a(n)$.

The difference between $k_{iI}^a(n)$ and $k_{iO}^a(n)$ can be attributed to the differences between color of the tissue responses occurring inside and outside the tumor. Since tumors change the structure of normal tissues by definition, indeed we expect to see a change in the color of tissue response.

Applying the blind deconvolution scheme developed in [31] on the two combined axial kernels $k_{1I}^a(n)$ and $k_{1O}^a(n)$ which are shown in Figs. 17(a) and (c) respectively, we identified the color of the tissue responses inside the tumor ($t_{1I}^a(n)$) and outside the tumor ($t_{1O}^a(n)$). Obtained color terms $t_{1O}^a(n)$ and $t_{1I}^a(n)$ are shown in Fig. 19, together with their spectra. It is evident that the color of the tissue response outside the tumor (Fig. 19(b),(d)) is different from the one inside the tumor (Fig. 19(a) and (c)). Apparently, this reflects the change in the tissue structure inside the tumor.

Once we know the color of the tissue response $t_i^a(n)$, we can estimate the true axial

distortion kernel $h^a(n)$ from eq.(10) and (11), through a deconvolution process. We used the constrained Wiener filter technique described in [40] for this purpose. Fig. 20(a) illustrates the resulting estimates for $h^a(n)$. The corresponding spectra are plotted in Fig. 20(b).

Lateral Distortion Kernels

In Fig. 21, two of the typical combined lateral distortion kernels estimated inside and outside of the tumor are shown, together with their spectra. In Figs. 21(b) and (c), solid lines indicate the spectra of data which were used to estimate the distortion kernels, and dotted lines indicate the spectra of the kernels themselves. In order to account for depth related beam spreading, both kernels were estimated at the same axial depth, $5.0cm$, in the true tissue space. As before, 20 adjacent lateral data lines in the rf-image were concatenated to form the basis for the estimations. Each lateral kernel represents an area of $17mm^2$ (approx.) in the original tissue space. From Fig. 21, we can see that the lateral distortion kernels estimated from inside and outside of the tumor assume two slightly different shapes. The same observation is true for the spectra of the rf-data lines used to estimate these kernels.

Using the same procedure followed in the case of axial distortion kernels, we estimated the color of the tissue response (lateral direction), working on the lateral distortion kernels shown in Fig. 21. The resulting terms corresponding to the color of the tissue response are shown in Fig. 22, together with their spectra. It is clear that the color of the tissue response, $t_i^l(n)$ is different in the two regions of the image considered.

Following the same procedure as in the case of axial distortion kernels, we estimated the true lateral distortion kernel. Resulting color-free lateral distortion kernels, $h^l(n)$ and their spectra are shown in Fig. 23.

Using the lateral distortion kernel $h^l(n)$ estimated above, we deconvolved the rf-data corresponding to the image shown in Fig. 16(a). The result of lateral deconvolution is shown in Fig. 16(b), where the logarithmically compressed envelope has been used for display purposes. The result of lateral deconvolution using the kernel $h^l(n)$, followed by the axial deconvolution using $h^a(n)$ estimated earlier, is in Fig. 16(c). Note that we used only a single lateral kernel to deconvolve the entire image. This may be justifiable as a first approximation, considering the depth (approx. 2 cm in the real tissue space) of the image involved.

Deconvolution of the image was also performed using the combined distortion kernels. These kernels are basically the same kernels that would result under the white assumption about the tissue response. The deconvolution results were *identical to the ones shown in Figs. 16(b) and (c).*

Based on Fig. 16, we can conclude that there is a considerable resolution enhancement, especially after the lateral deconvolution, while the resolution improvement is the same for both combined and true distortion kernels. The latter observation leads us to the conclusion that tissue response can be safely assumed white for deconvolution purposes. Although there is some difference in the combined kernels inside and outside the tumor, or otherwise, when tissue structure variations occur, this difference is not significant to affect the deconvolution result. *This difference, however, emerges as potential tissue signature* [2]. If we are interested in detecting tissue structure changes, (e.g., changes between tumorous and tumor-free areas) the combined kernels can not be used. The distortion kernels are the dominant components in the combined kernels and mask the small contribution of the color of the tissue response which carries the discriminating information. The color of the tissue response as a tissue signature has been investigated in [2] (see also Appendix A).

6.3.4 SOS-based estimated distortions and deconvolution of B-mode images

From the images obtained at experiments A, C and D, SOS-based distortions were estimated with the method of Section 6.1.3. The images were subsequently deconvolved, and the deconvolution results are shown in Figs. 27, 28 and 29, respectively. The corresponding resolution gains and speckle SNR are shown in Tables 5 and 6.

Comparing Tables 1 and 2 to 5 and 6, we can conclude that the resolution improvement, both axial and lateral, was consistently superior when deconvolution was performed with the HOS-based estimated distortions. Deconvolution with HOS-based estimates led to axial resolution improvement 1.15 - 1.9 times higher than deconvolution with SOS-based estimates. The improvement of lateral resolution when deconvolving using HOS based estimates was more dramatic; it was better than the SOS based deconvolution by a factor in the range 1.68-4.5. The superiority of the HOS-based deconvolution is also evident by comparing the corresponding images deconvolved with HOS and SOS-based distortion estimates.

7 CONCLUSIONS/FUTURE WORK

Processing ultrasound images with higher-order spectral operations we were able to identify the distortion introduced by the ultrasonic system and the medium. The proposed method makes it possible to estimate both axial and instantaneous lateral blurring kernels, working on B-mode RF data. Distortion identification and subsequent cancelling (deconvolution) operations were carried out on 1-D lines of the RF image, thereby obviating the theoretical

difficulties faced by earlier attempts at beam deconvolution on envelope detected images. The method is capable of estimating mixed phase distortion kernels, and is immune to additive Gaussian noise.

Performing underwater experiments employing single element transducers, commercial tissue mimicking phantoms and simulated point targets, we showed that our kernel estimation procedure could be done with reasonable accuracy. The accuracy of the estimations were verified by measuring axial kernels underwater.

Deconvolution results obtained with phantom data and clinical images indicate considerable resolution improvement. Lateral deconvolution contributes heavily to the gain in resolution, where the resolution was defined in terms of the dimensions of the autocovariance function of the image. These results are significant because in unprocessed images, lateral distortions are known to be as much as 3-5 times severe than axial distortions, leading to a change in appearance in clinical images depending on the orientation of the scanner. Through lateral deconvolution, one can compensate for the lateral distortions and try to achieve consistent images independent from the angular position of the scanner. In the past, distortion estimation was carried out exclusively in the second-order statistics domain. We demonstrated that deconvolution based on HOS-based distortion estimates leads to superior axial and in particular lateral resolution improvement than the one with SOS-based estimates.

Liver tissue is relatively homogeneous, thus the resolution improvement via deconvolution came at little surprise. The highly inhomogeneous nature of breast tissue, on the other hand, made the application of the proposed methodology to breast data a not at all straightforward task. It was really exciting to see that indeed the proposed methodology led to significant resolution gains when applied on human breast images. The resolution gains were quantified based on our standard mathematical measures, but most important based on the opinion of our medical collaborators at Thomas Jefferson University Hospital. Trained radiologists compared the images before and after processing and found that the processed images revealed fine details that were hidden in the original images, and which could be critical in determining the malignant or not nature of the tumor. Although more extensive studies need to be conducted, and on line processing should be considered, we view the obtained results as very encouraging.

It has been reported that high transducer frequencies required for high resolution imaging actually lead to lower resolution in the presence of increased aberration in breast at higher frequencies [8]. In [36] it is pointed out that medium inhomogeneities are also important in systems where a larger aperture is used for higher lateral resolution. In general, the aberration correction is of fundamental importance in high resolution medical ultrasonic

systems. The ability of the proposed method to compensate for convolution components of aberration holds promise in improving the diagnostic value of B-mode breast images beyond the capabilities of hardware.

Deconvolution, viewed as an image de-blurring/restoration operation, should reveal those small structures (such as early stage tumors) that had been hidden away from view due to imaging distortions (including convolutional components of aberrations), but otherwise would show up *on a hypothetical, perfect imager.* A deconvolved image also means access to a distortion-free tissue signal, which is largely independent of the imaging system. Therefore, tissue characterization schemes which ideally require imaging-system-independent data could be based on deconvolved RF images. In addition, the estimated distortion kernels themselves carry information on the statistical structure of scatterer field as manifested through the color of the scatterer response (tissue response), attenuations and, propagation non-linearities associated with the phantom (tissue). Indeed our preliminary investigation suggested that the color of the tissue response is an excellent candidate as a tissue signature.

8 REFERENCES

References

[1] U.R. Abeyratne, A.P. Petropulu and J.M. Reid, "Higher Order Spectra Based Deconvolution of Ultrasound Images," *IEEE Transactions on Ultrasonics, Ferroelectrics, and Frequency Control*, vol. 42(6), November 1995.

[2] U.R. Abeyratne, A.P. Petropulu and J.M. Reid, "On Modeling the Tissue Response From Ultrasonic B-Scan Images," *IEEE Trans. on Medical Imaging*, August 1996.

[3] U.R. Abeyratne, A.P. Petropulu and J.M. Reid, "Blind Deconvolution of Ultrasound Images," *SPIE International Symposium on Optics, Imaging and Instrumentation*, San Diego, July 1994.

[4] U.R. Abeyratne, A.P. Petropulu, J.M. Reid and T. Golas, "Estimating Imaging Distortions and Tissue Response From Ultr asonic Images," *20^{th} International Symposium on Ultrasonic Imaging and Tissue Characterization*, Arlington, VA, June 1995.

[5] U.R. Abeyratne, A.P. Petropulu and J.M. Reid, "Higher Order Spectra Based Deconvolution of Ultrasound Image s," *IEEE Workshop on Nonlinear Signal and Image Processing*, Neos Marmaras, Gre ece, June 1995.

[6] V. N. Adrov and V. Chernomordik, "Mathematical Simulation of Pressure Pulse Propagation in Biological Tissue", *Ultrasonic Imaging*, Vol. 15, pp 59-71, 1993.

[7] F. Arditi, S. Foster and J. W. Hunt, "Transient Fields of Concave Annular Arrays", *Ultrasonic Imaging*, 3, pp 37-61, 1981.

[8] W. J. Davros, E. L. Madsen and J. A. Zagzebski, "Breast Mass Detection by US: a phantom study," *Radiology*, 156, pp 773-775, 1985.

[9] M. Fatemi and A. C. Kak, "Ultrasonic B-Scan Imaging: Theory of Image Formation and a Technique for Restoration", *Ultrasonic Imaging*, Vol. 2, pp 1-47, 1980.

[10] S. W. Flax and M. O'Donnell, "Phase aberration correction using signals from point reflectors and diffuse scatterers: Basic principles", *IEEE Trans. Ultr., Ferroelec., Freq. Contr.*, V UFFC-35, pp. 758-767, 1988.

[11] P. D. Freiburger, D. C. Sullivan, B. H. LeBlanc, S. W. Smith, G. E. Trahey, "Two Dimensional Ultrasound Beam Distortion in the Breast: In Vivo Measurements and Effects.", *Ultrasonic Imaging*, Vol 14, pp 398 -414, 1992.

[12] T. Golas, A.P. Petropulu, J.M. Reid, "In-vivo distortion estimation from ultrasound images: a comparative study of autocorrelation based versus higher-order statistics based methods," *Intern. Conf. on Acoustics Speech and Signal Processing,* ICASSP-96, Atlanta GA, 1996, submitted.

[13] T. Golas, A.P. Petropulu, J.M. Reid, "In-vivo distortion estimation from ultrasound images: a comparative study of autocorrelation based versus higher-order statistics based methods," to be submitted to the *IEEE Trans. on UFFC.*

[14] E. E. Hundt, E. A. Trautenberg, "Digital Processing of Ultrasound Data by Deconvolution", *IEEE Transactions on Sonics and Ultrasonics* , Vol. SU-27, No. 5, pp 249-252, 1980.

[15] J. A. Jensen and S. Leeman, "Nonparametric Estimation of Ultrasound Pulses", *IEEE Trans. Biomedical Engineering* , Vol. 41, No. 10, pp 929-936, October 1994.

[16] J. A. Jensen, "Estimation of Pulses in Ultrasound B-Scan Images", *IEEE Trans. on Medical Imaging* . MI-10, NO. 2, pp 164-172, 1991.

[17] J. A. Jensen, "A model for the propagation and scattering of ultrasound in tissue", *J. Acoust. Soc. Amer.*, 89, pp. 188-191, 1991.

[18] J. A. Jensen, "Deconvolution of Ultrasound Images", *Ultrasonic Imaging,* V14, pp.1-15 1992.

[19] R. Kuc, "Application of Kalman Filtering Techniques to Diagnostic Ultrasound ", *Ultrasonic Imaging*, Vol. 1, pp 105-120, 1979.

[20] R. Kuc and H. Li, "Reduced Order Autoregressive Modeling for Center Frequency Estimation", *Ultrasonic Imaging*, Vol. 7, pp 244-251, 1985.

[21] C. N. Liu, M. Fatemi and R. C. Waag, "Digital Processing for Improvement of Ultrasonic Abdominal Images", *IEEE Trans. on Medical Imaging.* MI-2, NO. 2, pp 66-75, 1983.

[22] D. -L. Liu and R. C. Waag, "Time-shift Compensation of Ultrasonic Focus Degradation Using Least-Mean-Square Error Estimates of Arrival Time" *J. of Acoust. Soc. Am.* 95(1), pp 542-555, 1994.

[23] X. M. Lu, "L1 and L2 norm deconvolution and its application in medical ultrasound", *Ph.D. dissertation*, Drexel University, 1992.

[24] C. L. Nikias and A.P. Petropulu, **Higher-Order Spectra Analysis: A Nonlinear Signal Processing Framework**, Prentice Hall Incorporated, Oppenheim Series in Signal Processing, 1993.

[25] L. Nock, G.E. Trahey and S.W. Smith,"Phase aberration correction in medical imaging using speckle brightness as a quality factor", *J. Acoust. Soc. Amer.*, v 85 pp. 1819-1833, 1988.

[26] M. O'Donnell and W.E. Engeler, "Real-time phase aberration correction system for medical ultrasound imaging", *Proc. IEEE 1990 Engr. in Med. and Biol. Meeting*, pp. 278-280, 1990.

[27] A. V. Oppenheim, R. W. Schafer, **Discrete-Time Signal Processing**, Englewood Cliffs, NJ: Prentice-Hall, 1989.

[28] A. Papoulis and C. Chamzas, "Improvement in Range Resolution by Spectral Extrapolation ", *Ultrasonic Imaging*, Vol. 1, pp 121-132, 1979.

[29] A. P. Petropulu, "Higher order spectra in biomedical signal processing", *CRC Press Biomedical Engineering Handbook*, 1995.

[30] A. P. Petropulu, "Higher order spectra in biomedical signal processing", *International Federation of Automatic Control (IFAC) Biomedical Symposium*, Galveston, Texas, March 27, 1994.

[31] A. P. Petropulu and C. L. Nikias, "Blind Deconvolution Using Signal Reconstruction from Partial Higher Order Cepstral Information",*IEEE Transactions on Signal Processing*, Vol. 41, No. 6, pp 2088-2095, 1993.

[32] D. E. Robinson and M. Wing, "Lateral Deconvolution of Ultrasound Beams ", *Ultrasonic Imaging*, 6, pp. 1-12 , 1984.

[33] H. Schomberg, W. Vollmann and G. Mahne, "Lateral Inverse Filtering of Ultrasonic B-Scan Images", *Ultrasonic Imaging*, Vol. 5, pp 38-54, 1983.

[34] P. M. Shankar, J. M. Reid, H. Ortega, C. W. Piccoli and B. B. Goldberg, " Use of Non-Rayleigh Statistics for the Identification of Tumors in Ultrasonic B-Scans of the Breast" , *IEEE Transactions on Medical Imaging*, Vol. 12, pp 687-692, 1993.

[35] P. R. Stepanishen, "The time-dependent force and radiation impedance on a piston in a rigid infinite planar baffle", *J. Acoust. Soc. Am.*, v. 49, pp. 841-849, 1971.

[36] Y. Sumino and R. C. Waag, "Measurement of Ultrasonic Pulse Arrival Time Differences Produced by Abdominal Wall Specimens", *J. Acoust. Soc. Am.*, 90(6), 2924-2930, 1991.

[37] C. W. Towfig, C. W. Barnes and A. J. Pisa, "Tissue Classification based on Autoregressive Models for Ultrasound Pulse Echo Data ", *Acta Electronica*, Vol 26, pp. 95-110, 1984.

[38] G. E. Trahey, D. Zhao, J. A. Miglin and S. W. Smith, "Experimental Results with a real-time Adaptive Ultrasonic Imaging System for Viewing Through Distorting Media", *IEEE Tr. on Ultr. Ferroelec. and Frequency Control* , Vol. 37, pp 418-427, 1990.

[39] G. E.Trahey, P. D. Freiburger, L. F. Nock and D. C. Sullivan, "In-vivo Measurements of Ultrasonic Beam Distortions in the Breast.", *Ultrasonic Imaging*, Vol 13, pp 71 -90, 1991.

[40] S. Treitel and L.R. Lines, "Linear inverse theory and deconvolution," *Geophysics*, vol. 47(8), pp. 1153-1159, August 1982.

[41] G. E. Tupholme, "Generation of acoustic pulses by baffled pistons", *Mathematica*, v. 16, pp. 209-224, 1969.

[42] R. H. Tuthill, R. H. Sperry and K. J. Parker, "Deviations From Rayleigh Statistics in Ultrasound Speckle", *Ultrasonic Imaging*, 10, pp 81-89, 1988.

[43] R. Vaknine and W. J. Lorenz, "Lateral Filtering of Medical Ultrasonic B-Scans Before Image Generation", *Ultrasonic Imaging*, Vol. 6, pp 152-158, 1984.

[44] W. Vollmann, "Resolution Enhancement of Ultrasonic B-Scan Images by Deconvolution", *IEEE Transactions on Sonics and Ultrasonics* , Vol. SU-29, NO. 2, pp 78-83, 1982.

9 FIGURES/TABLES

Table 1: Resolution gains due to deconvolution with HOS-based estimated distrotions

	Resolution Gains			
	lateral		*axial*	
	5dB	10dB	5dB	10dB
Experiment (A)	2.7	3.0	1.7	1.7
Experiment (C)	5.2	4.2	1.8	1.9
Experiment (D)	3.0	2.5	1.7	1.5

Table 2: The effect of deconvolution with HOS-based distortions on the speckle SNR ratio

	SNR	
	original	*deconvolved*
Experiment (A)	1.24	1.26
Experiment (C)	1.17	1.10
Experiment (D)	1.20	1.30

Table 3: *Resolution gains in breast images due to HOS-based deconvolution.*

	Resolution Gains			
	lateral		*axial*	
	5dB	10dB	5dB	10dB
Patient 1	5.6	2.0	8.6	5.6
Patient 2	4.8	4.0	1.9	1.8
Patient 3	3.0	2.1	1.7	1.6
Patient 4	2.2	1.8	2.1	1.9
Patient 5	2.9	1.9	1.3	1.2

Table 4: *The effect of HOS-based deconvolution of breast images on the speckle SNR ratio.*

	SNR	
	original	*deconvolved*
Patient 1	0.68	0.99
Patient 2	0.46	0.59
Patient 3	0.74	0.84
Patient 4	0.51	0.58
Patient 5	0.75	0.84

Table 5: The effect of deconvolution with SOS-based distortions on the speckle SNR ratio

	Resolution Gains			
	lateral		*axial*	
	5dB	10dB	5dB	10dB
Experiment (A)	1.6	1.35	1.53	1.20
Experiment (C)	1.85	0.93	1.48	1.64
Experiment (D)	1.50	1.44	1.50	1.23

Table 6: The effect of deconvolution with SOS-based distortions on the speckle SNR ratio

	SNR	
	original	*deconvolved*
Experiment (A)	1.21	1.24
Experiment (C)	1.2	1.20
Experiment (D)	1.10	1.17

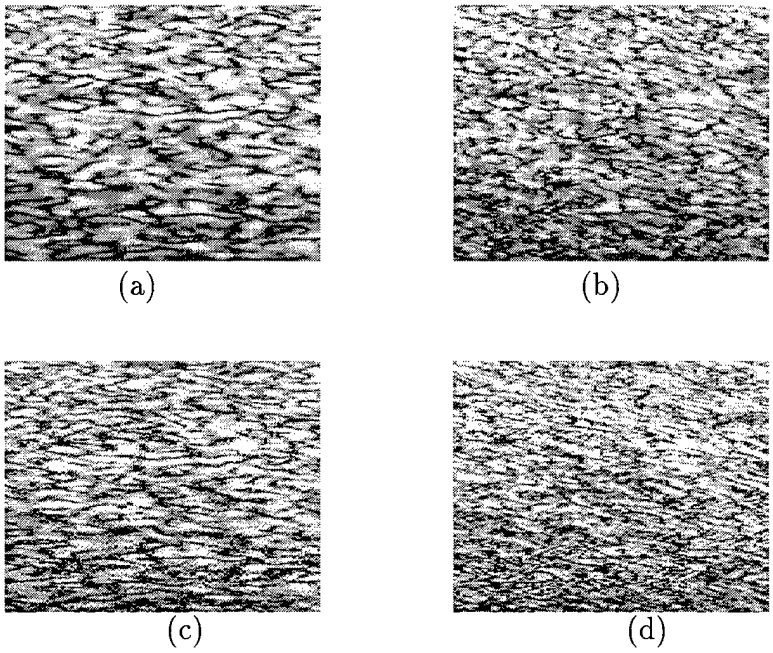

Figure 1: A speckle-only part of the ultrasound image of the tissue mimicking phantom, obtained with a focused single element transducer *experiment (A)*; (b) the result of late ral deconvolution; (c) the result of axial deconvolution and, (d) the result of lateral followed by axial deconvol ution. In all cases, the logarithmically compressed envelope is shown. Deconvolution was performed with the **higher-order statistics** based estimated distortions.

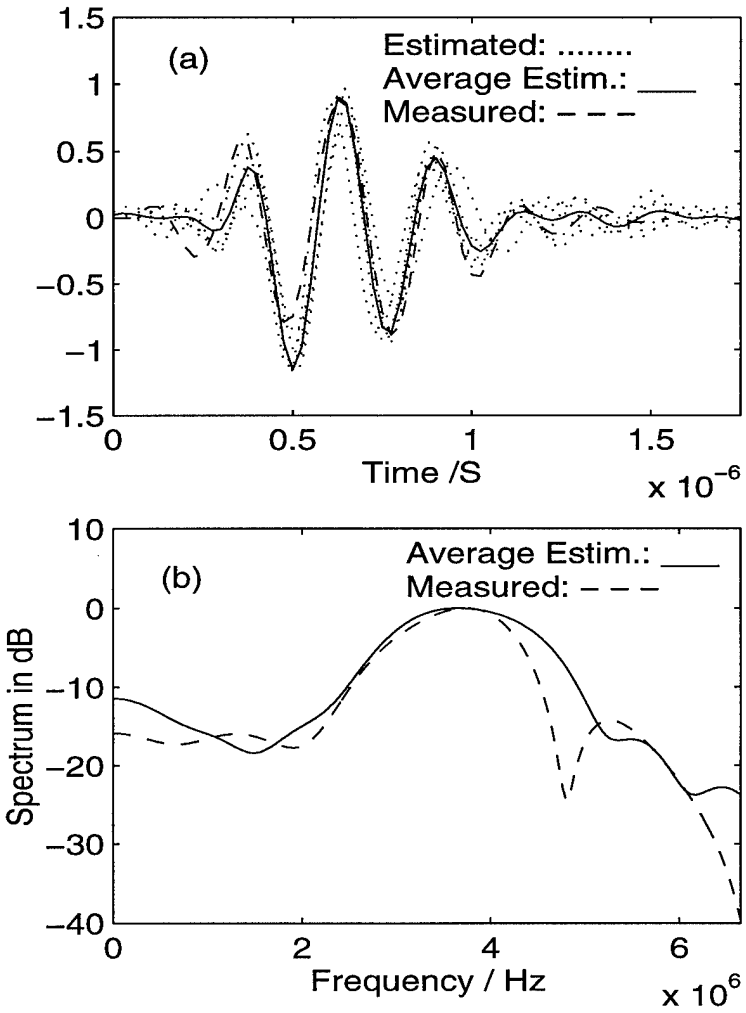

Figure 2: Underwater experiments (*experiments (A) and (B)*): (a) axial kernels estimated at various lateral positions in the B-mode image of the tissue mimicking phantom (dotted lines); average of the estimated kernels (solid line). The experimental kernel, measured as the reflection off a $0.812mm$ diameter wire surface, under water. The close agreement between the estimated and the measured kernels (with in limits of experimental errors), indicates the success of the estimation procedure. (b) Spectra of the average estimated kernel (solid line) and the measured kernel (dashed line). The center frequency of both kernels are compatible with the nominal center frequency of the transducer, 3.5MHz.

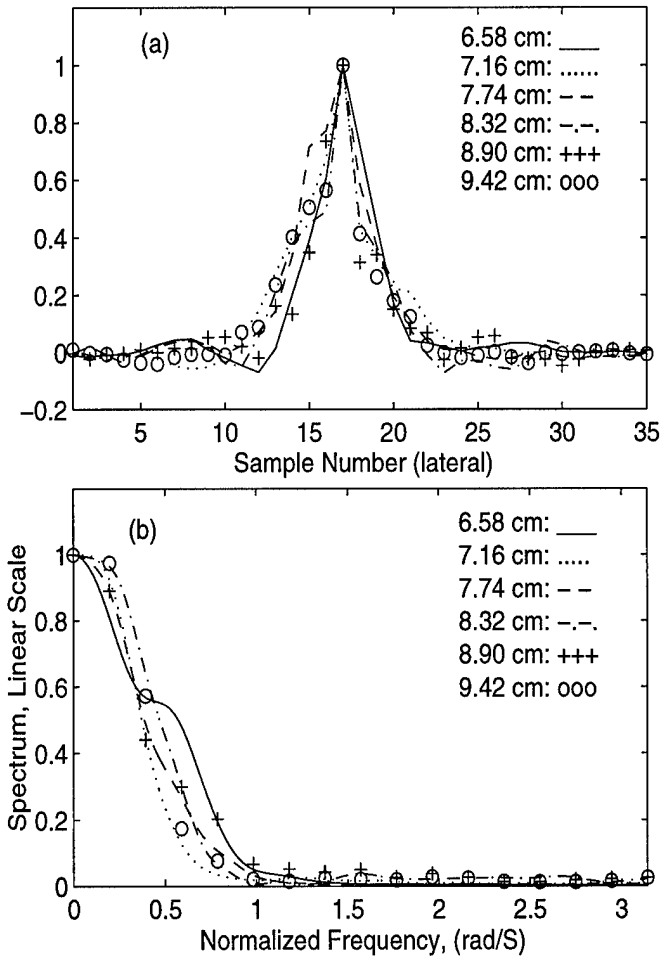

Figure 3: (a) Lateral distortion kernels estimated at various axial depths from the RF data corresponding to the image shown in Fig. 1(a). All the kernels are estimated within the focal zone of the transducer, $6 - 13cm$. (b) Spectra of the lateral kernels shown in (a).

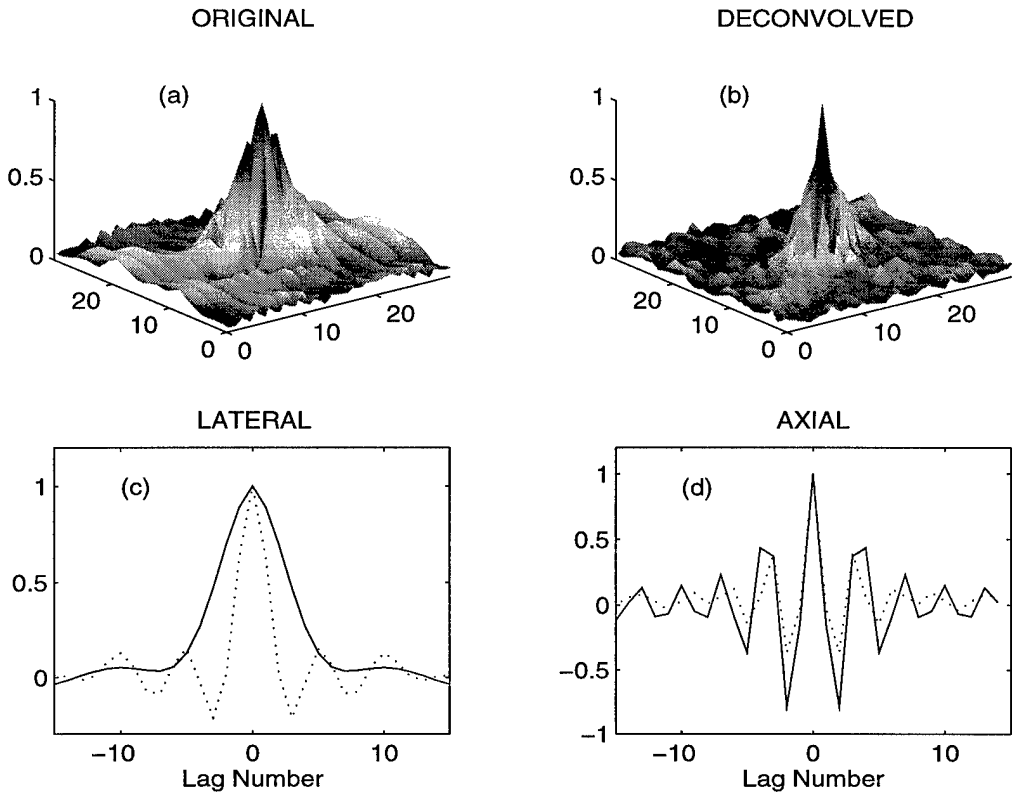

Figure 4: Shaded auto-covariance function of the RF-data corresponding to: (a) the original image shown in Fig. 1(a); (b) the laterally and axially deconvolved image shown in Fig. 1(d). Absolute values of the auto-covariance functions have been shown for easy visualization. (c) The lateral slice L_{00} and (d) the axial slice A_{00} of the auto-covariance function corresponding to: the original image (solid lines), the deconvolved image (dotted lines).

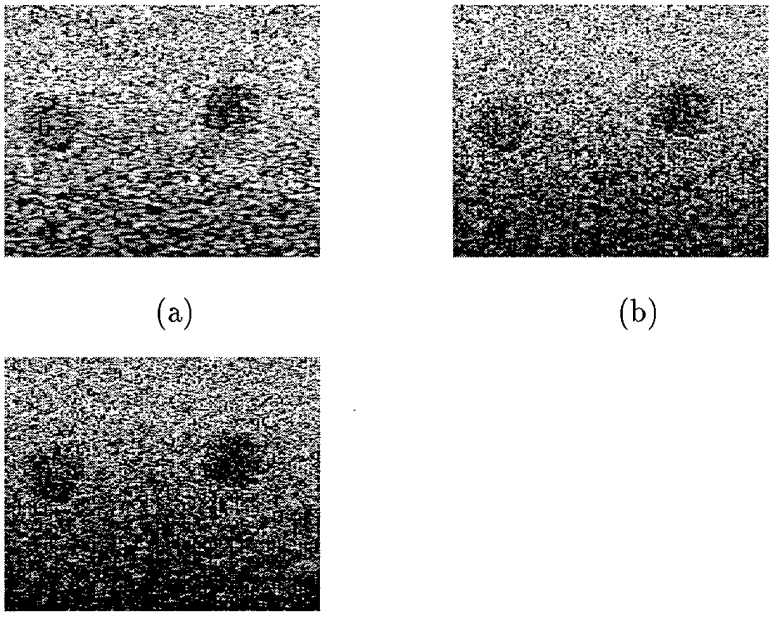

(a) (b)

(c)

Figure 5: (*Experiment (C)*): (a) The original image of the tissue mimicking phantom obtained with the linear array transducer on a clinical imaging system; (b) the result of lateral deconvolution and (c) the result of lateral and axial deconvolution. The logarithmically compressed envelope has been used for display. Deconvolution was performed with the HOS-based estimated distortions.

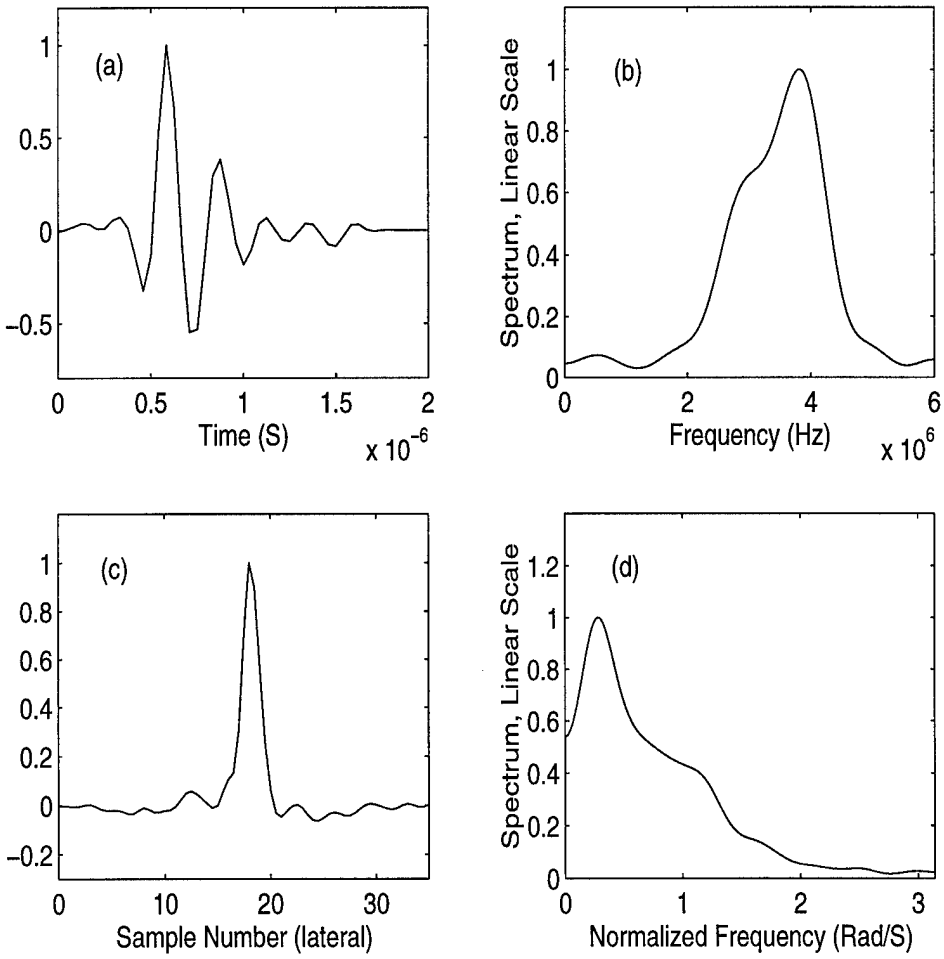

Figure 6: (*Experiment (C)*): (a) The average of the estimated axial kernels from RF-data corresponding to image shown in Fig. 5(a), and (b) its spectrum. (c) The average of the lateral kernels estimated from RF-data corresponding to Fig. 5(a) and (d) its spectrum. These kernels were estimated from the region between the two cylindrical targets in Fig. 5(a).

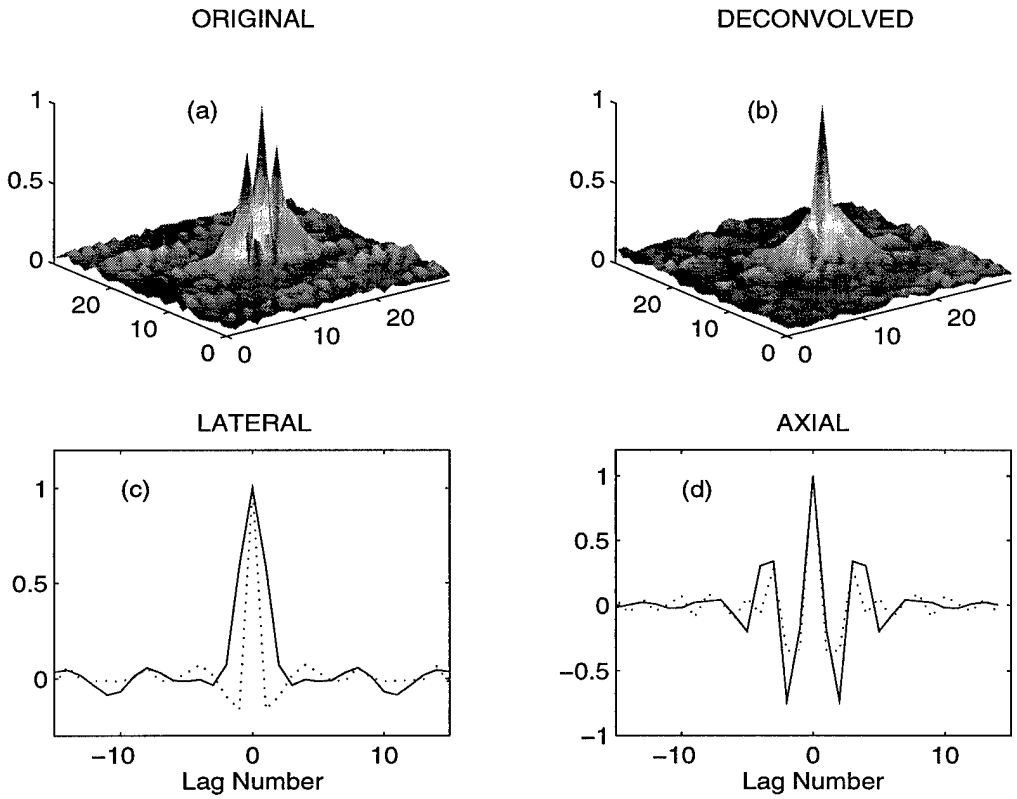

Figure 7: Shaded auto-covariance function of the RF-data corresponding to: (a) the original image shown in Fig. 5(a); (b) the laterally and axially deconvolved image shown in Fig. 5(d). Absolute values of the auto-covariance functions have been shown for easy visualization. (c) The lateral slice L_{00} and (d) the axial slice A_{00} of the auto-covariance function corresponding to: the original image (solid lines), the deconvolved image (dotted lines).

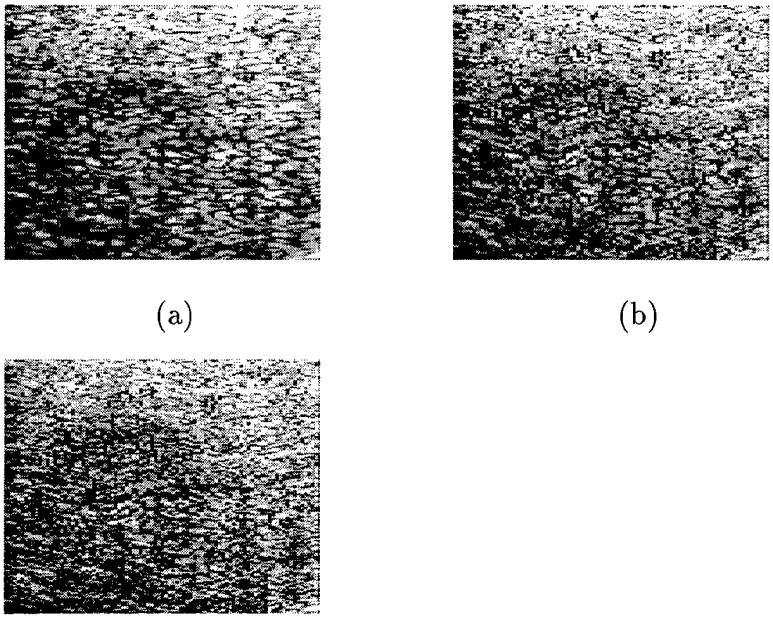

(a) (b)

(c)

Figure 8: (*Experiment (D)*): (a) A part of the clinical image of a human liver containing a tumor; (b) the result of lateral deconvolution and (c) the result of lateral and axial deconvolution. In all cases the logarithm of the envelope is shown. (HOS-based deconvolution is shown here).

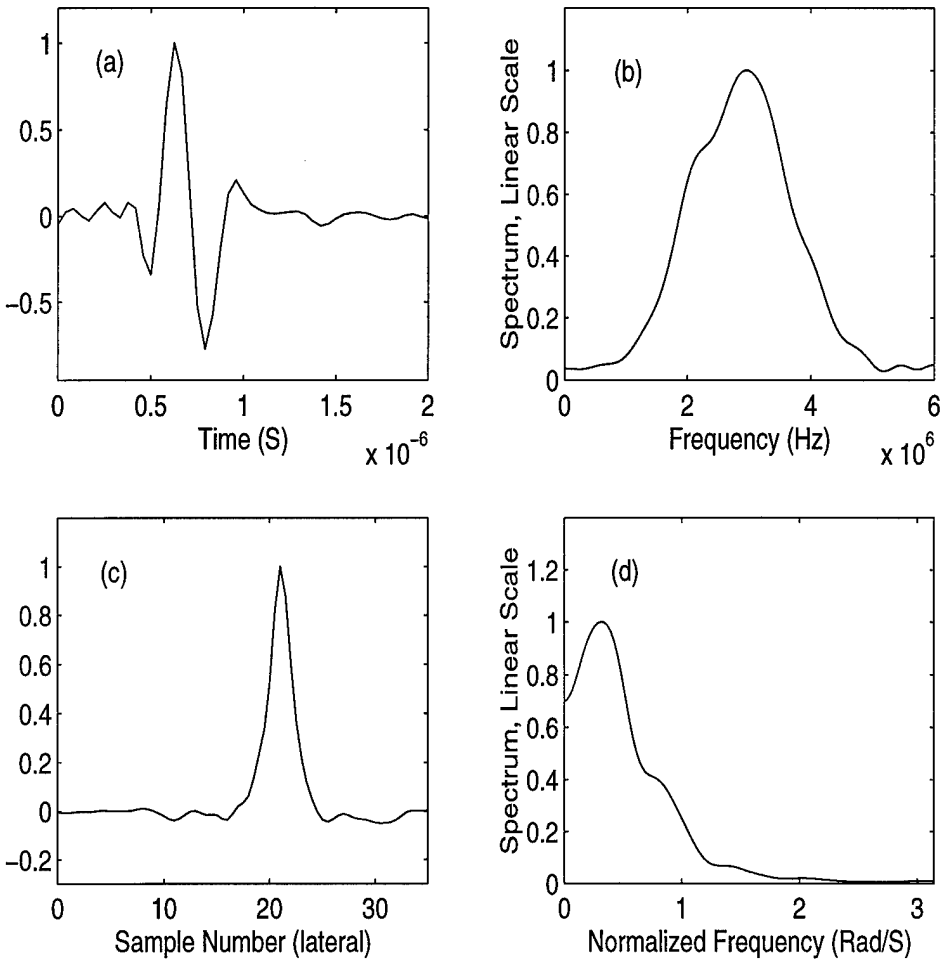

Figure 9: (*Experiment (D)*): (a) The average of the estimated axial kernels from RF-data corresponding to image shown in Fig. 8(a), and (b) its spectrum. (c) The average of the lateral kernels estimated from RF-data corresponding to Fig. 8(a) and (d) its spectrum.

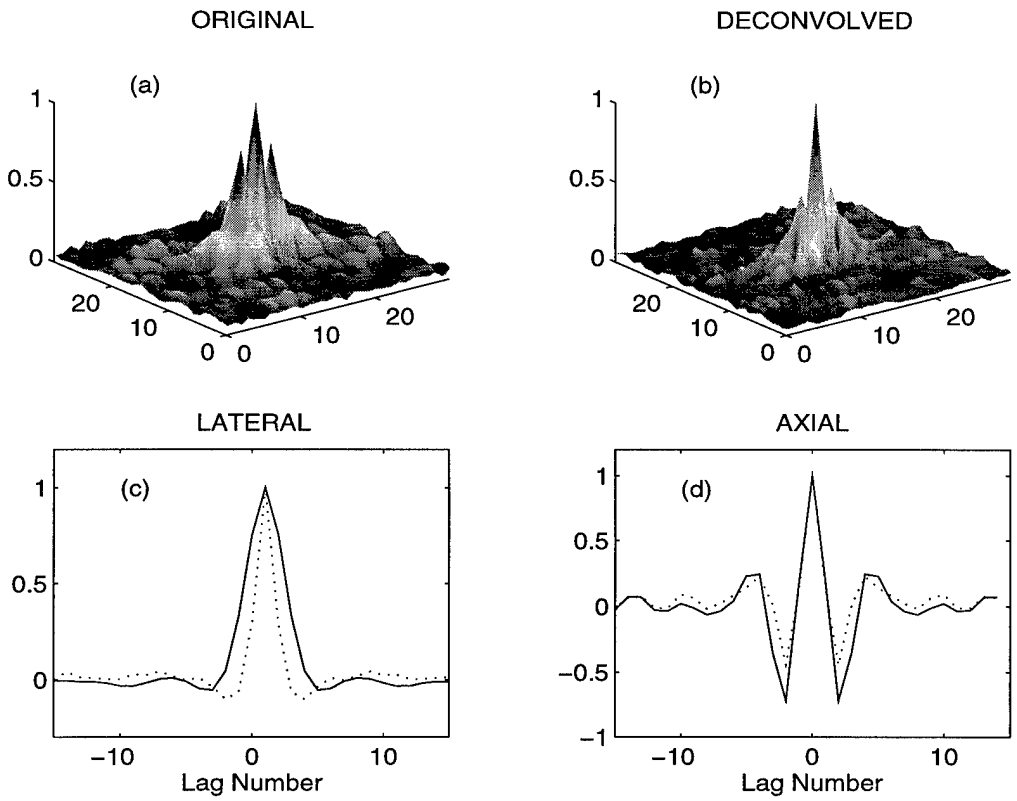

Figure 10: Shaded auto-covariance function of the RF-data corresponding to: (a) the original image shown in Fig. 8(a); (b) the laterally and axially deconvolved image shown in Fig. 8(d). Absolute values of the auto-covariance functions have been shown for easy visualization. (c) The lateral slice L_{00} and (d) the axial slice A_{00} of the auto-covariance function corresponding to: the original image (solid lines), the deconvolved image (dotted lines).

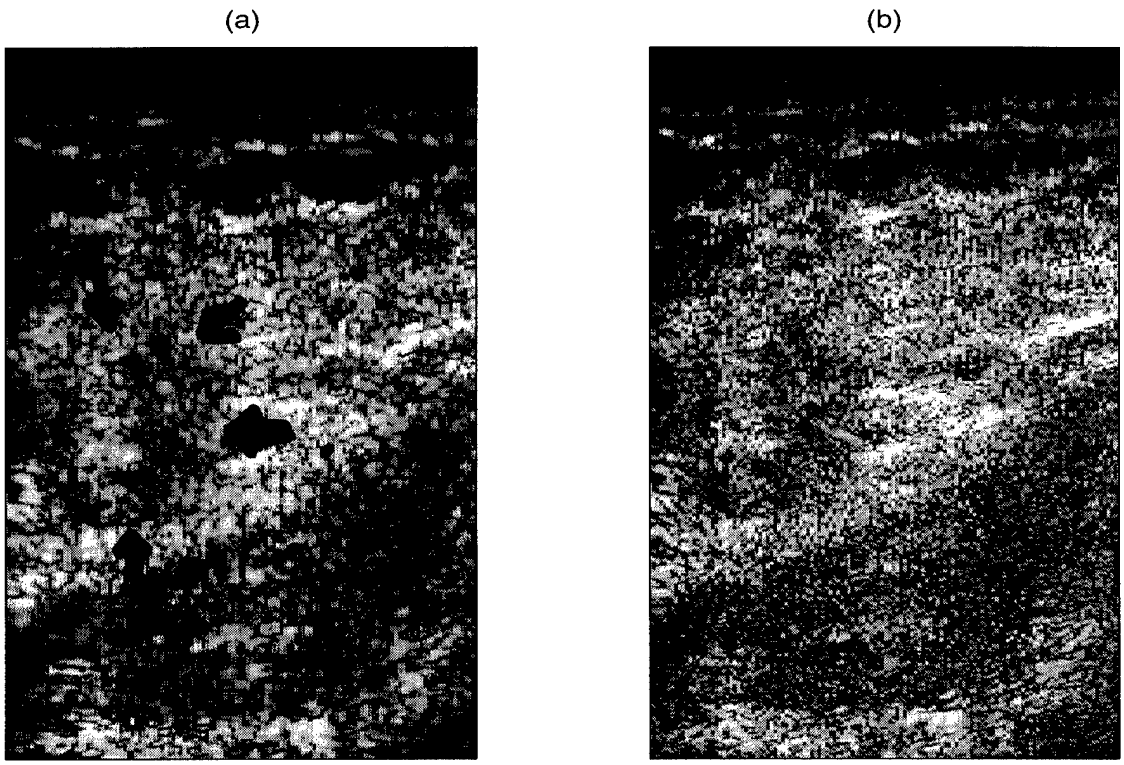

Figure 11: (*Patient 1*): (a) A part of the clinical image of a human breast containing a tumor; (b) the result of lateral followed by axial deconvolution. In all cases the logarithm of the envelope is shown.

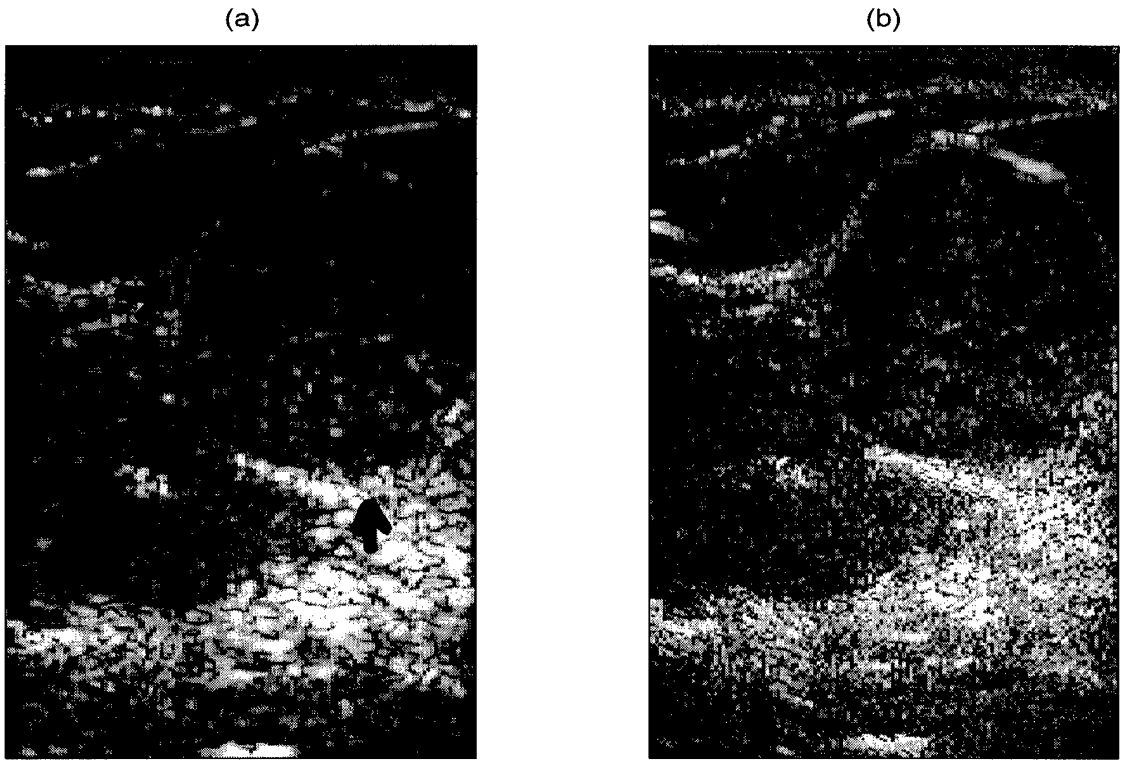

Figure 12: (*Patient 2*): (a) A part of the clinical i mage of a human breast containing a tumor; (b) the result of lateral followed by axial deconvolu tion. In all cases the logarithm of the envelope is shown.

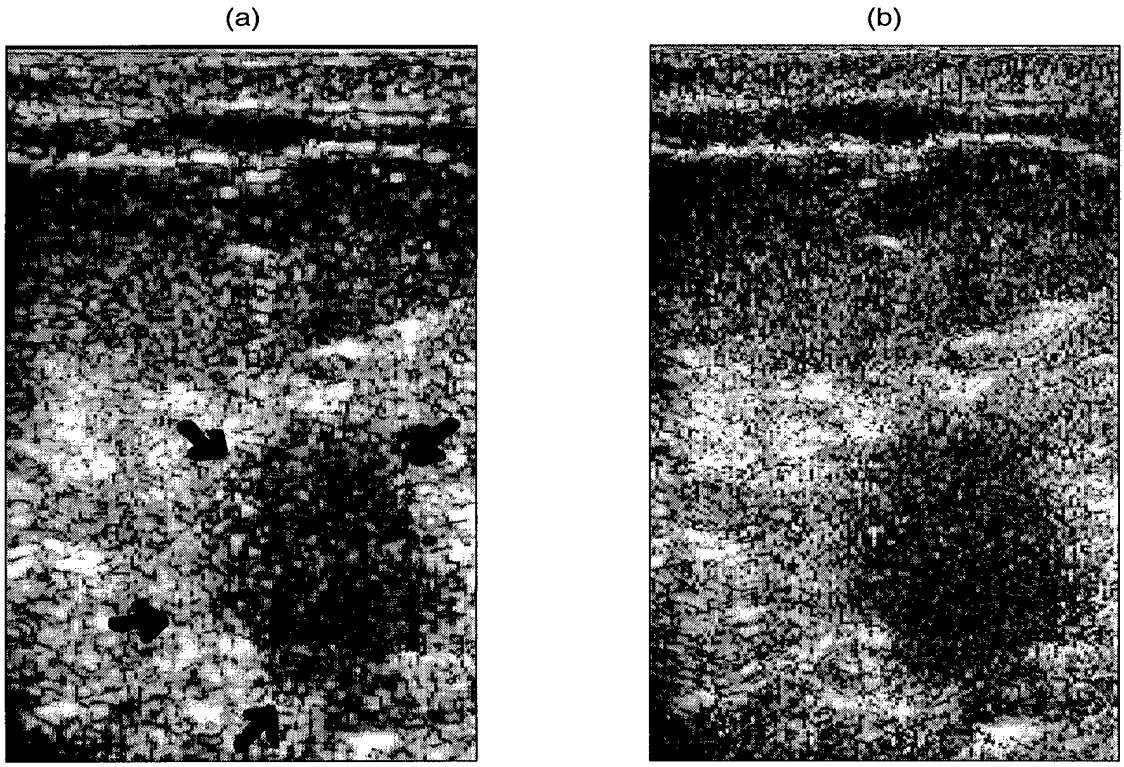

Figure 13: (*Patient 3*): (a) A part of the clinical image of a human breast containing a tumor; (b) the result of lateral followed by axial deconvolution. In all cases the logarithm of the envelope is shown.

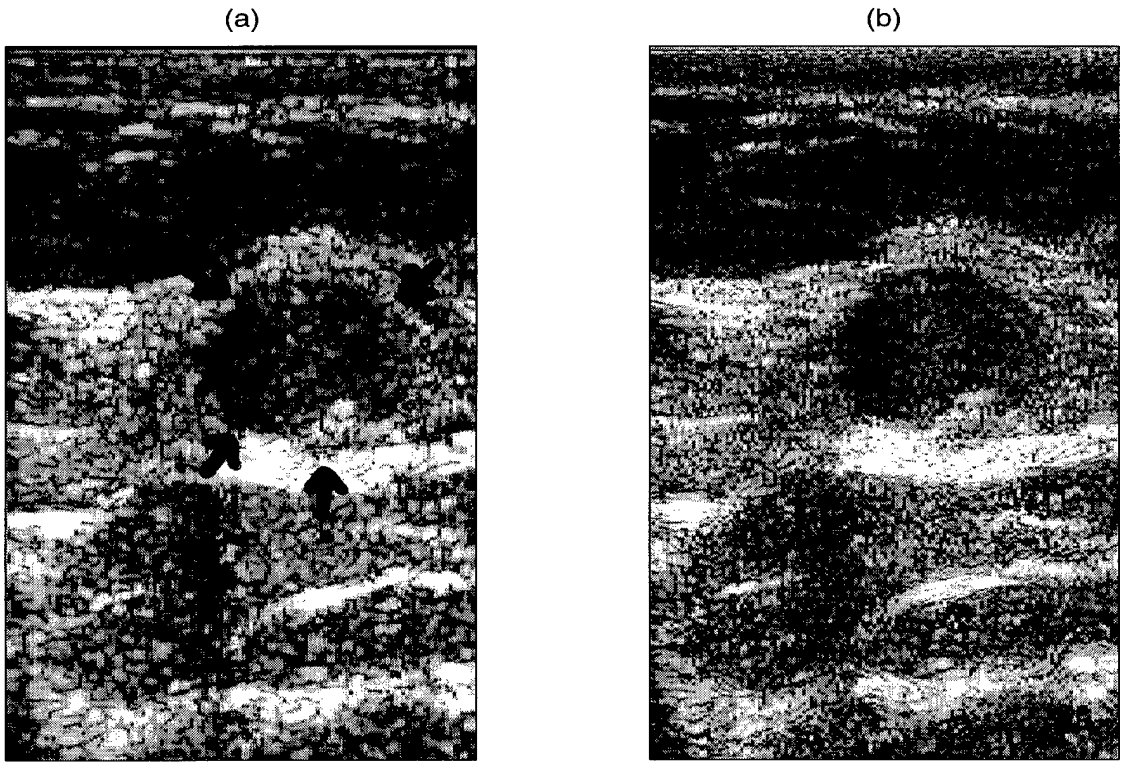

Figure 14: (*Patient 4*): (a) A part of the clinical image of a human breast containing a tumor; (b) the result of lateral followed by axial deconvolution. In all cases the logarithm of the envelope is shown.

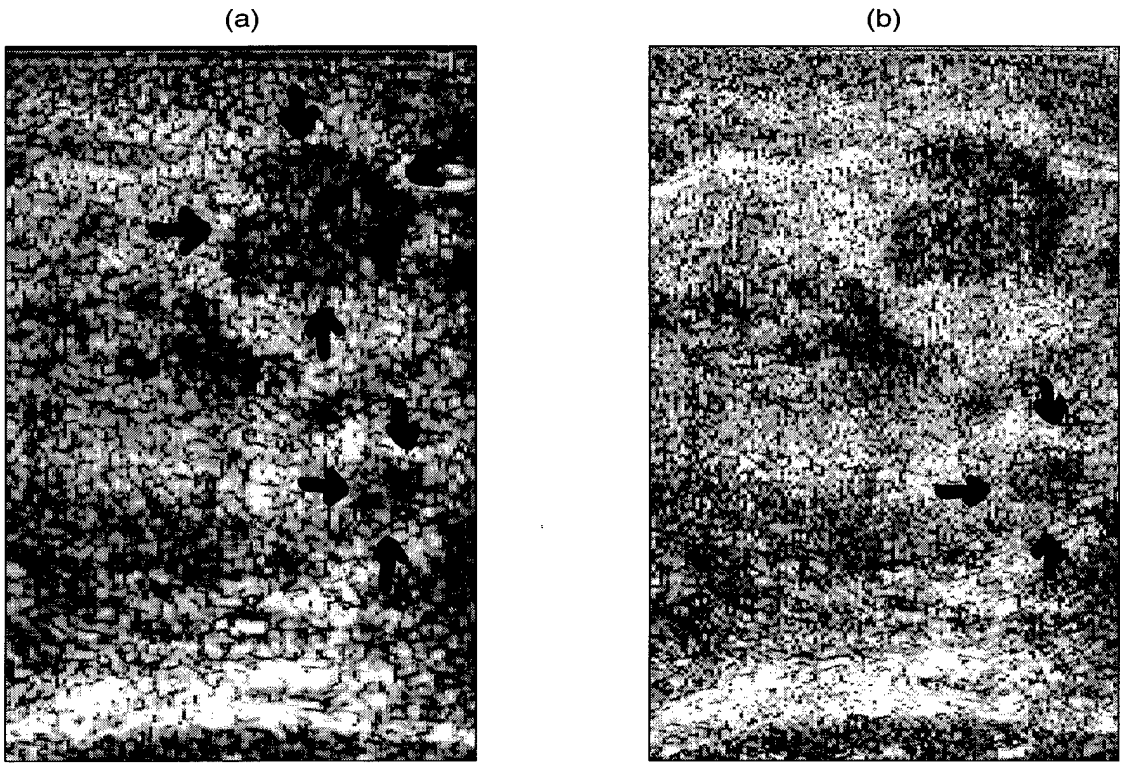

Figure 15: (*Patient 5*): (a) A part of the clinical image of a human breast containing a tumor; (b) the result of lateral followed by axial deconvolution. In all cases the logarithm of the envelope is shown.

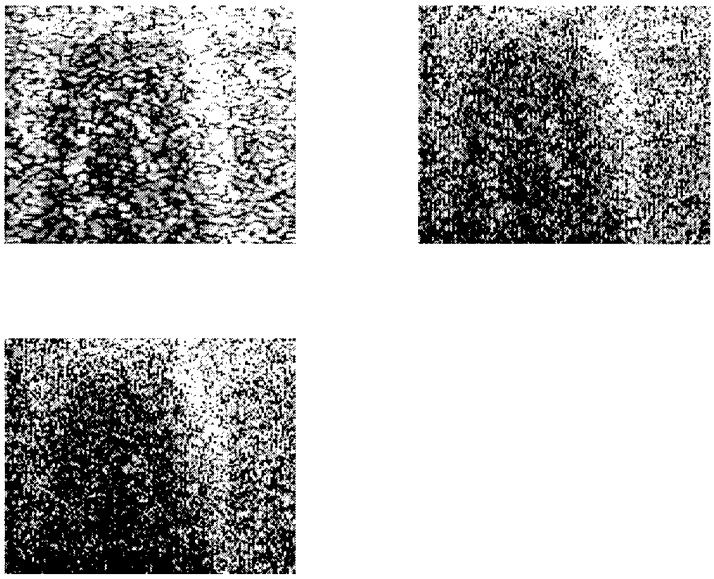

Figure 16: Clincal image of a human liver. (a) Envelope of a part of the original image containing hypo-echoic liver metastasis tumor; (b) laterally deconvolved image; (c) laterally followed by axially deconvolved image. logarithm of the envelope is shown.

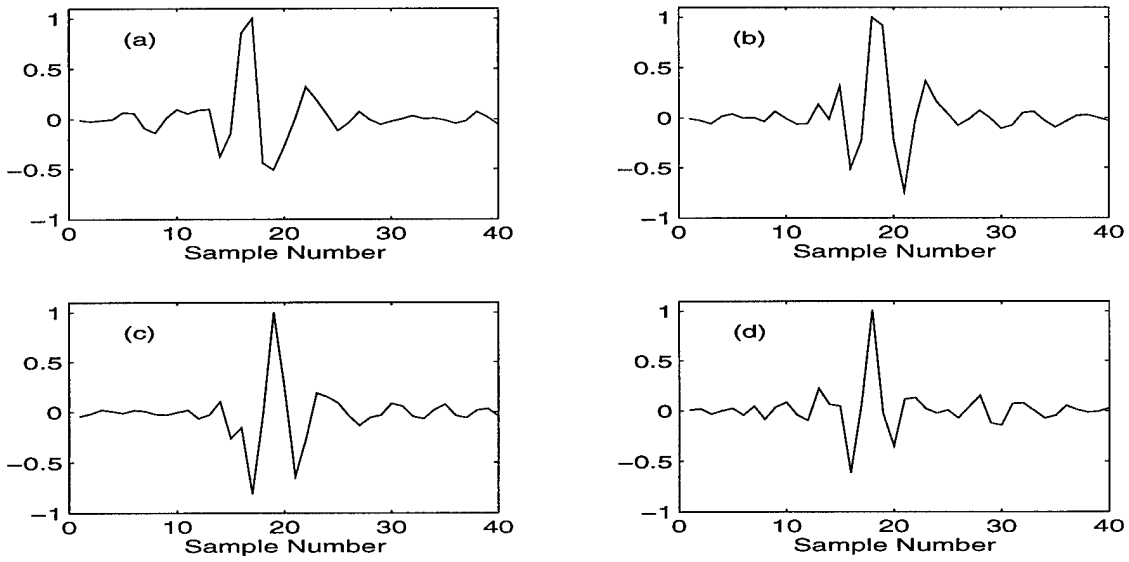

Figure 17: (a),(b) Combined axial distortion kernels estimated from small regions inside the liver tumor; (c),(d) combined axial distortion kernels estimated outside the liver tumor.

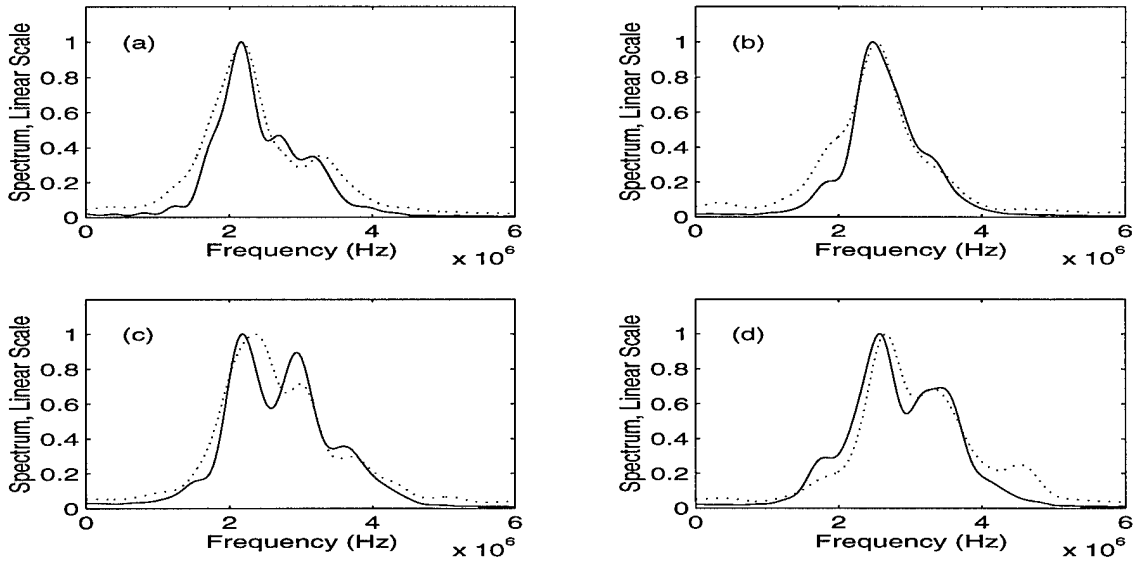

Figure 18: (a),(b) Spectral of combined axial distortion kernels estimated from small regions inside the liver tumor; (c),(d) spectra of combined axial distortion kernels estimated outside the liver tumor. Solid lines indicate the spectra of estimated kernels and dotted lines those of the rf data based on which the kernels were estimated.

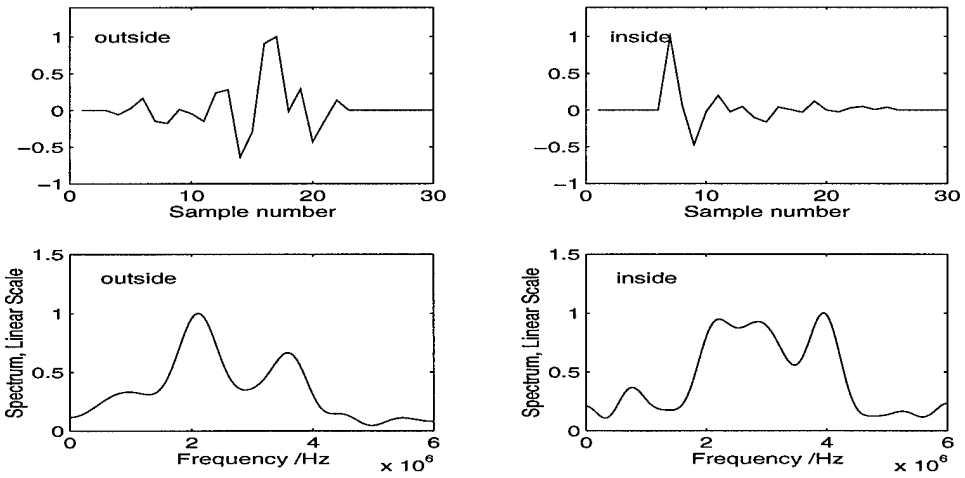

Figure 19: Color of the axial tissue response estimated from small regions (a) inside the tumor and (b) outside the tumor. (c) Spectrum of the kernel shown in (a); (d) spectrum of the kernel shown in (b).

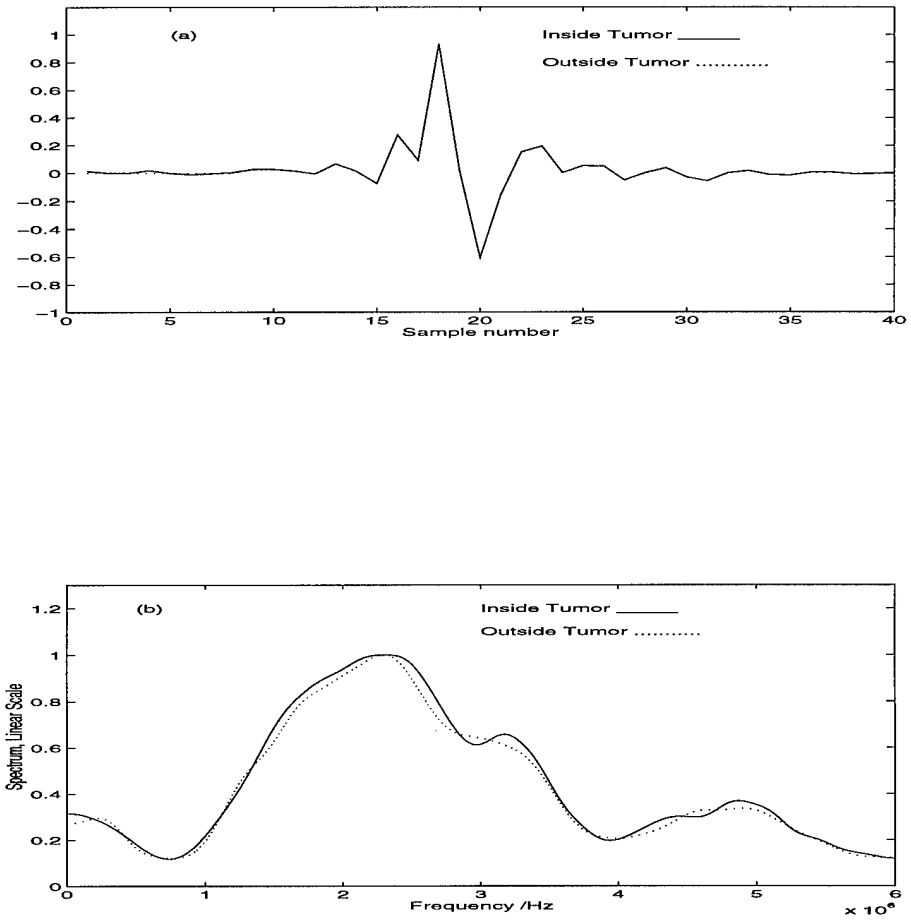

Figure 20: (a) True axial distortion kernels reconstructed based on the combined distortion kernels estimated from inside (solid line) and outside (dotted line) the tumor, and (b) the corresponding spectra.

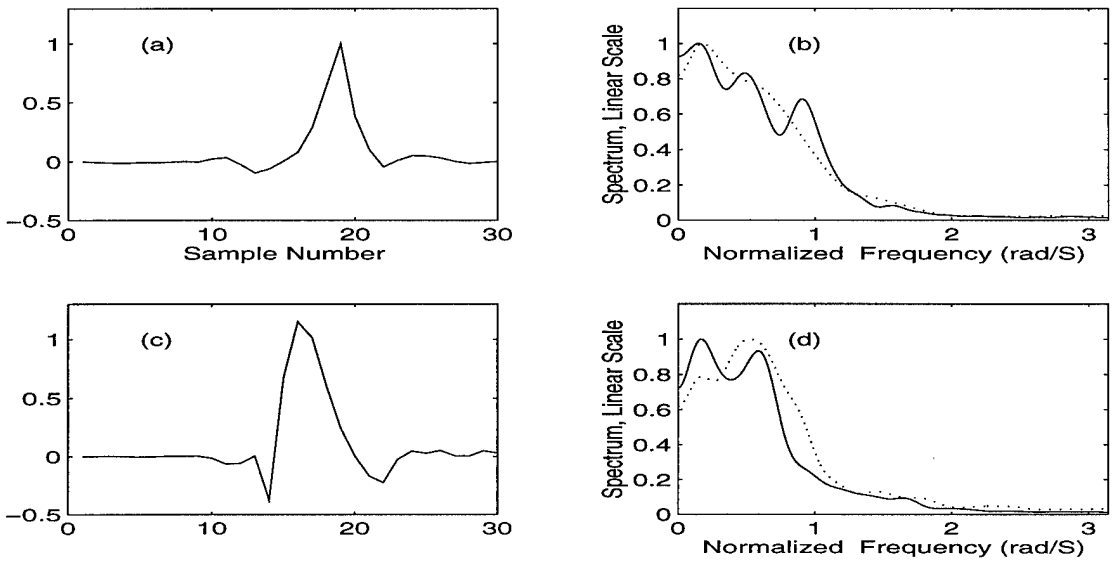

Figure 21: (a) Combined lateral distortion kernels estimated (a) inside the tumor, and (b) its spectrum. Combined lateral distortion kernels estimated (c) outside the tumor, and (d) its spectrum. Solid lines indicate the spectra of estimated kernels and dotted lines those of the rf data based on which the kernels were estimated.

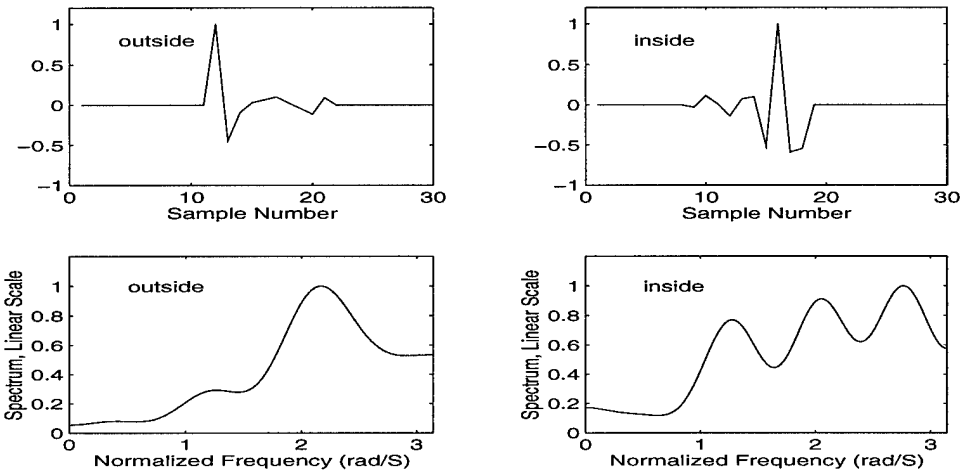

Figure 22: (a) The color of the lateral tissue response estimated (a) inside the tumor and (b) outside the tumor. (c), (d) The spectra corresponding to (a) and (b).

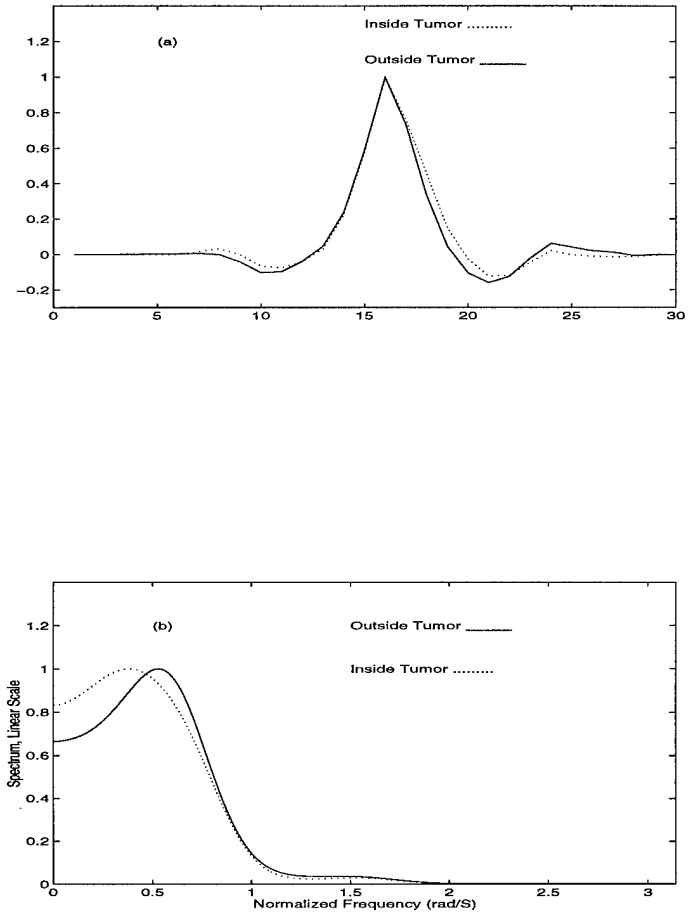

Figure 23: (a) True lateral distortion kernels reconstructed from the combined kernels estimated from inside (dotted line) and outside (solid line) the tumor. (b) The corresponding spectra.

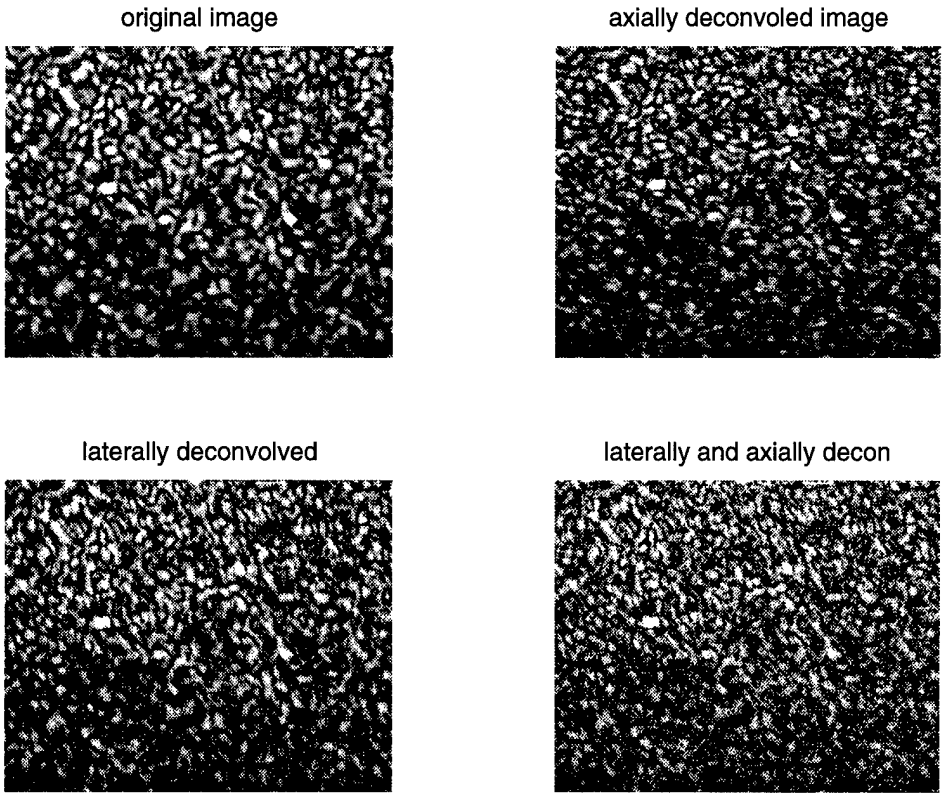

Figure 24: A speckle-only part of the ultrasound image of the tissue mimicking phantom, obtained with a focused single element transducer *experiment (A)*; (b) the result of lateral deconvolution; (c) the result of axial deconvolution and, (d) the result of lateral followed by axial deconvolution. In all cases, the logarithmically compressed envelope is shown. Deconvolution was performed with the **second-order statistics** based estimated distortions.

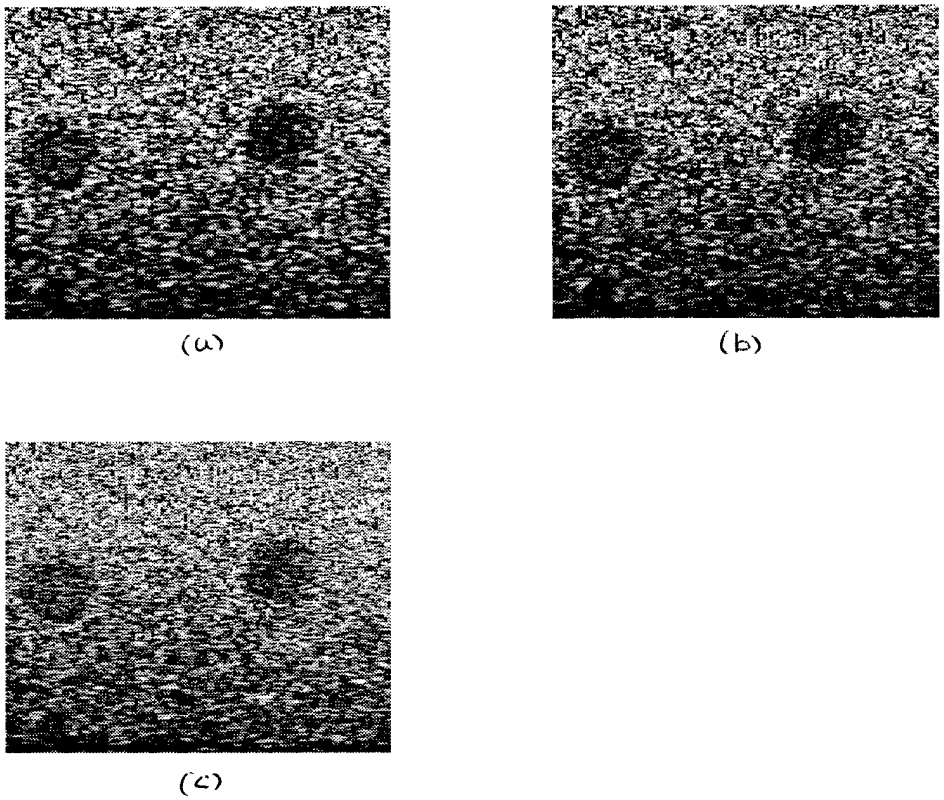

Figure 25: (*Experiment (C)*): (a) The original image of the tissue mimicking phantom obtained with the linear array transducer on a clinical imaging system; (b) the result of lateral deconvolution and (c) the result of lateral and axial deconvolution. The logarithmically compressed envelope has been used for display. Deconvolution was performed with the second-order statistics based estimated distortions.

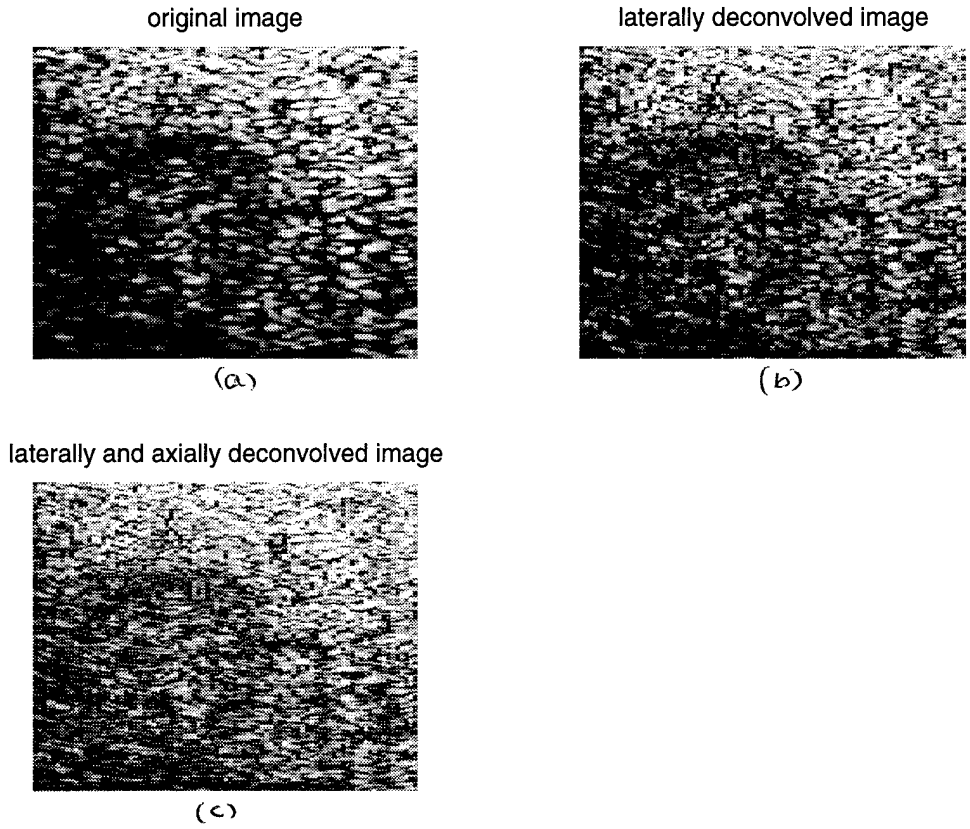

Figure 26: (*Experiment (D)*): (a) A part of the clinical image of a human liver containing a tumor; (b) the result of lateral deconvolution and (c) the result of lateral and axial deconvolution. In all cases the logarithm of the envelope is shown. (second-order statistics based deconvolution is shown here).

10 PUBLICATIONS

Journal publications supported by this grant during 1994-1995

- A.P. Petropulu, "Higher-Order Spectra in biomedical signal processing," *CRC Press Biomedical Engineering Handbook*, 1995.
- U.R. Abeyratne, A.P. Petropulu and J.M. Reid, "Higher Order Spectra Based Deconvolution of Ultrasound Images," *IEEE Transactions on Ultrasonics, Ferroelectrics, and Frequency Control*, vol. 42(6), November 1995.
- U.R. Abeyratne, A.P. Petropulu and J.M. Reid, "On Modeling the Tissue Response From Ultrasonic B-Scan Images," *IEEE Trans. on Medical Imaging*, August 1996.
- U.R. Abeyratne, A.P. Petropulu, J.M. Reid, and F. Forsberg "Blind deconvolution of ultrasound breast images: a comparative study of autocorrelation based versus higher-order statistics based methods," submitted to the *IEEE Trans. on Ultrasonics, Ferroelectrics, and Frequency Control* in 1996.

Conference proceedings publications supported by this grant during 1994-1995

- U.R. Abeyratne, A.P. Petropulu and J.M. Reid, "Blind Deconvolution of Ultrasound Images," *SPIE International Symposium on Optics, Imaging and Instrumentation*, San Diego, July 1994.
- U.R. Abeyratne, A.P. Petropulu, J.M. Reid and T. Golas, "Estimating Imaging Distortions and Tissue Response From Ultrasonic Images," *20^{th} International Symposium on Ultrasonic Imaging and Tissue Characterization*, Arlington, VA, June 1995.
- U.R. Abeyratne, A.P. Petropulu and J.M. Reid, "Higher Order Spectra Based Deconvolution of Ultrasound Image s," *IEEE Workshop on Nonlinear Signal and Image Processing*, Neos Marmaras, Gre ece, June 1995.
- U.R. Abeyratne and A.P. Petropulu, "α-Weighted Cumulant Projections: a Novel Tool for System Identification," *29^{th} Annual Asilomar Conference on Signals, Systems and Computers*, California, October 1995.
- U.R. Abeyratne, A.P. Petropulu, J.M. Reid, E. Halpern and F. Forsberg, "Higher-Order Statistics Based Approaches for Estimating Scatterer Periodicity and Correlation Structure of Tissue," *21st International Symposium on Ultrasonic Imaging and Tissue Characterization*, Arlington, VA, June 1996.

MEETING ABSTRACTS

SPIE International Symposium on Optics, Imaging and Instrumentation, San Diego, July 1994.

Blind Deconvolution of Ultrasound Images

Udantha R. Abeyratne, Athina P. Petropulu and John M. Reid*

Biomedical Engineering and Science Institute
*Department of Electrical and Computer Engineering,
Drexel University, Philadelphia, PA 19104

We address the problem of improving the resolution of ultrasound images using blind deconvolution. The transducer measurement that forms the ultrasound image can be expressed as the convolution of two terms, the tissue response and the ultrasonic system response, plus additive noise. The quantity of interest is the tissue response, however, due to the convolution operation, we measure a blurred version of it, which obscures the fine details in the image. Our goal is to remove the blurring caused by the ultrasonic system, in order to enhance the diagnostic quality of the ultrasound image. Under the assumption that speckle behaves as an i.i.d. zero-mean non-Gaussian process, we were able to reconstruct the blurring kernel using bicepstrum operations on corresponding A-scan lines. Based on the estimated blurring kernel we performed deconvolution on the measured image. Preliminary results obtained from ultrasound images of a tissue mimicking phantom indicate significant resolution improvement.

20^{th} International Symposium on Ultrasonic Imaging and Tissue Characterization, Arlington, VA, June 1995.

Estimating Imaging-Distortions and the Color of the Tissue Response From Ultrasonic Images

Udantha R. Abeyratne, Athina P. Petropulu, John M. Reid and Thomas Golas**

Biomedical Engineering and Science Institute
***Department of Electrical and Computer Engineering,**
Drexel University, Philadelphia, PA 19104

We address the problem of estimating imaging-distortions and modeling the tissue response from clinical B-scan ultrasound images, based on rf A-lines that form the image. We

model rf A-lines as: $y_i(n) = h_i(n) * f_i(n) + w_i(n), i = 1, 2, \cdots$, where $y_i(n)$ is the observed rf A-line, $f_i(n)$ is the tissue response, $w_i(n)$ is the observation noise and $h_i(n)$ is the kernel representing imaging distortions; the symbol '$*$' stands for the convolution operation. The fol- lowing assumptions are made: [A1] $h_i(n)$ is deterministic, possibly non- minimum phase, [A2] $f_i(n)$ is stationary, zero-mean non-Gaussian, modeled as the convolution of a white component $e_i(n)$ and a deterministic part $t_i(n)$ corresponding to the statistical color of the issue response, [A3] $w_i(n)$ is zero-mean, Gaussian, and independent of $f_i(n)$. A colored random process is taken as the model for the tissue response, considering the fact that under- lying scatterers need not be randomly and independently located. Applying higher order spectra based blind deconvolution on pairs of closely located rf A-lines, we identify the color of the tissue response as well as the distortion kernels. The color of the tissue response is independent of the imaging system and can be used in tissue characterization. We estimate distortion kernels and the color of the tissue response, from a B-mode image of a human liver, containing a tumor. The statistical color of the tissue response estimated inside the tumor has features that are distinctly different from those estimated outside the tumor. This may be attributed to the change in the tissue structures brought about by the tumor. Our kernel estimation and color identification process is based on data from regions as small as 12 mm^2 (approx.) in the tissue space. The advantages of the proposed approach are:(a) since the estimations are carried out in higher order spectra domain, results are immune to additive Gaussian noise in observations, and (b) both minimum phase and non-minimum phase kernels can be estimated. We compare our method with existing non-parametric pulse estimation techniques and demonstrate relative strengths and weaknesses.

IEEE Workshop on Nonlinear Signal and Image Processing, Neos Marmaras, Greece, June 1995.

Higher Order Spectra Based Deconvolution of Ultrasound Images

Udantha R. Abeyratne, Athina P. Petropulu[†], John M. Reid
Biomedical Engineering and Science Institute
[†] Electrical and Computer Engineering Department
Drexel University, Philadelphia, PA 19104

Our goal is to model and identify the tissue response based on the backscattered rf signal that forms the ultrasound image. We model the rf ultrasonic image, in both axial and lateral directions, as the convolution between an 1-D hypothetical tissue response and

the ultrasonic system response (distortion), plus additive Gaussian noise. We model the tissue response as a non-Gaussian, colored random process. Closely spaced axial (lateral) image lines contain as a common convolutional term the axial (lateral) distortion, whereas the noncommon terms are due to the tissue color. Applying blind deconvolution, we identify the color of the tissue response as well as the corresponding distortion kernels. The color of the tissue response is independent of the imaging system and can be used as a tissue characterization parameter. Estimated kernels are compared with experimentally obtained kernels, and the deconvolution of real ultrasound images is performed.

Asilomar 1995

α-Weighted Cumulant Projection: A New Tool For System Identification

*Udantha R. Abeyratne and Athina P. Petropulu**

Biomedical Engineering and Science Institute
*Department of Electrical and Computer Engineering,
Drexel University, Philadelphia, PA 19104

Summary

It is well established that identification of a nonminimum phase non-Gaussian random process can be achieved based on its higher-order cumulants (order three or higher). We propose a computationally attractive approach for system identification, whose complexity remains constant as the order of the employed cumulants increases. We define the **α–weighted n^{th}-order cumulant projection** of the process $x(k)$ to be

$$p_n^x(\tau;\alpha) = \sum_{\tau_2} \cdots \sum_{\tau_{n-1}} c_n^x(\tau,\tau_2,...,\tau_{n-1})\alpha^{\tau+\tau_2+...+\tau_{n-1}}, \quad \alpha : complex, |\alpha| = 1, \tag{17}$$

where $c_n^x(\cdot)$ denotes n^{th} order cumulant. For the process

$$x(k) = h(k) * e(k), \tag{18}$$

where $e(k)$ is white non-Gaussian zero-mean, and $h(k)$ is deterministic generally nonminimum phase, we prove that

$$P_n^x(z;\alpha) = cH(\alpha^{-1}z)H(\alpha^{(n-1)}z^{-1}), \tag{19}$$

where $P_n^x(z;\alpha)$ is the Z-transform of $p_n^x(\tau;\alpha)$, and c is a constant. ¿From (19), it can be shown that by controlling α, $H(z)$ can be identified for $n > 2$. If $\hat{p}_n^x(k;\alpha)$ and $\hat{h}(k)$ denote

the complex cepstra of $p_n^x(\tau;\alpha)$ and $h(k)$, respectively, we show that

$$\hat{h}(k) = \frac{\hat{p}_n^x(k;\alpha) - \alpha^{(n-1)k}\hat{p}_n^x(k;1)}{\alpha^k - \alpha^{(n-1)k}},\ k > 0 \tag{20}$$

$$\hat{h}(-k) = \frac{-\hat{p}_n^x(k;\alpha) + \alpha^k\hat{p}_n^x(k;1)}{\alpha^k - \alpha^{(n-1)k}},\ k > 0, \tag{21}$$

which leads to a scaled and shifted version of $h(k)$ via inverse cepstrum operations. We show that we can always find a complex number α with unit magnitude to guarantee that the denominator in (20) and (21) is different from zero, and discuss the rationale behind choosing a particular value for α.

Based on equation (19) a formula for the estimation of the Fourier phase of $h(k)$ from the phase of the α-weighted cumulant projection is also derived.

21st International Symposium on Ultrasonic Imaging and Tissue Characterization, Arlington, VA, June 1996.

Higher-Order Statistics Based Approaches for Estimating Scatterer Periodicity and Correlation Structure of Tissue

Udantha R. Abeyratne, Athina P. Petropulu, John M. Reid, Ethan J. Halpern+ and Flemming Forsberg+*

Biomedical Engineering and Science Institute

* Electrical and Computer Engineering Department Drexel University, Philadelphia, PA 19104

+Dept. of Radiology, Thomas Jefferson University Hospital, Philadelphia. PA 19107.

We model tissue as a collection of point scatterers embedded in a uniform media, and show that the higher- order statistics of the scatterer spacing distribution can be estimated from digitized RF scan line segments and be used in obtaining tissue signatures. We model the ultrasonic RF echo, y(t), by y(t)=h(t)*f(t)+w(t), where h(t) is the pulse-echo wavelet of the imaging system, w(t) is the zero-mean observation noise, and "*" is the linear convolution operator. The quantity f(t), which we will call the tissue response, represents the underlying tissue structure, and is modeled as: f(t) = rd(t)+rm(t)+rr(t), where, rd(t) represents unresolvable diffuse scatterers leading to fully-developed speckle with Gaussian statistics [1], [2], rr(t) represents resolvable, coherent scatterers with long-range order (pseudo-periodicity).The quantity rm(t) represents unresolvable periodicity from structural scatterers, and, correlated non-periodic components of diffused and structural scatterers (short- range order). The terms rm(t), rr(t) (and their contributions to the RF-echo y(t))

are non-Gaussian, due to contributions from periodic structures and/or scatterers of short range order. Based on our model for tissue micro structure, we develop methods for the estimation of resolvable periodicity via higher-order spectra of the RF observation y(t). Also, we propose a tissue signature, the color of the tissue response , that captures the correlation among non-periodic scatterers. The tools employed, i.e., higher-order statistics, were chosen as the most appropriate ones because they suppress Gaussian processes, such as the one arising from the diffused scatterers and observation noise. Higher-order statistics, unlike second-order statistics, also preserve the Fourier-phase of the color of the tissue response. Working on simulated and clinical data, we show that the proposed periodicity estimation technique is superior to the widely used power spectrum and cepstrum techniques in terms of the accuracy of estimations. We also show that even when there is no significant periodicity in data, we are still able to characterize tissues using signatures based on the higher-order cumulant structure of the scatterer spacing distribution.

[1] K.D. Donohue, J.M. Bressler, T. Varghese and N.M. Bilgutay, "Spectral Correlation in Ultrasonic Pulse-echo Signal Processing", IEEE Tr. on Ultrasonics, Ferroelec., and Frequency Control, vol. 40, no. 4, pp.330-337, 1993.

11 PERSONNEL

John M. Reid, Drexel University
Athina P. Petropulu, Drexel University
Udantha Abeyratne, Drexel University
Thomas Golas, Drexel University
Vladimir Genis, Drexel University
Christopher Wendt, Drexel University

12 APPENDICES

On Modeling The Tissue Response From Ultrasonic B-scan Images

Udantha R. Abeyratne, Athina P. Petropulu, John M. Reid

Abstract— **We model tissue as a collection of point scatterers embedded in a uniform media, and show that the higher-order statistics (*HOS*) of the scatterer spacing distribution can be estimated from digitized *RF* scan line segments and be used in obtaining tissue signatures. We assume that *RF* echoes are non-Gaussian, on the grounds of empirical/theoretical justifications presented in works such as [25], [6], [3], [24] and [27]. Based on our model for tissue microstructure, we develop schemes for the estimation of resolvable periodicity as well as correlations among non-periodic scatterers. Using higher-order statistics of the scattered signal, we define as tissue "color" a quantity that describes the scatterer spatial correlations, show how to evaluate it from the higher-order correlations of the digitized *RF* scan line segments, and investigate its potential as a tissue signature. The tools employed, i.e., higher-order statistics, were chosen as the most appropriate ones because they suppress Gaussian processes, such as the one arising from the diffused scatterers. Higher-order statistics, unlike second-order statistics, also preserve the Fourier-phase of the signature, the color of the tissue response. Working on simulated and clinical data, we show that the proposed periodicity estimation technique is superior to the widely used power spectrum and cepstrum techniques in terms of the accuracy of estimations. We also show that even when there is no significant periodicity in data, we are still able to characterize tissues using signatures based on the higher-order cumulant structure of the scatterer spacing distribution.**

Keywords— **tissue modeling, tissue characterization, medical ultrasound, higher-order statistics, periodicity estimation**

I. Introduction

ULTRASOUND is one of the widely used medical imaging techniques, due to its versatility, relative safety, low cost and the availability of portable units. It is commonly used by radiologists as an adjunct modality in differentiating between cystic and solid masses, a crucial distinction in diagnosing cancer. Despite decades of research leading to many technological advances, still the clinical diagnoses are primarily based on qualitative evaluation of images by expert observers. There have been many attempts at developing objective tissue characterization criteria on the premise that there is much more observer-independent information available from ultrasound than what is currently being used. These are rooted on the fundamental notion that the biological tissues are composed of characteristic structures whose ultrasonic properties often change due to diseases. The goal of tissue characterization is the extraction of signatures that assume distinct values in the presense of normal and diseased states of tissues, such that it is possible to differentiate between them.

Although the exact identities of the physical structures responsible for ultrasound backscattering are generally unknown [22], [5], they can usually be characterized either as macroscopic or microscopic, compared with the wavelength of the interrogating ultrasonic beam. The tissue is often modeled as a collection of point scatterers, embedded in a uniform non-scattering medium. Considering the biological variabilities associated with tissues, the spatial distribution and the scattering strengths (scattering cross-sections) associated with these scatterers are usually described in statistical terms. The statistics of the inter-scatterer spacing distribution are commonly used as tissue signatures.

In organs such as the liver the overall arrangement of the tissues consists of an organized repetition of a basic structural unit. This repeated structure is regarded to be providing resolvable, repeated scattering centers for the propagating ultrasonic pulse [10], [12], [13], [7]. It has been shown that a periodicity can be observed from the liver pulse-echo data, and the estimated periodicity can be linked to the mean-scatterer-spacing of the underlying tissue [10]. It was also shown that the mean scatterer spacing may be used as a feature for tissue characterization of diffuse liver diseases, such as cirrhosis and chronic active hepatitis [10],[13].

However, the success of some of these methods [10] was reported to be compromised by the presence of coherently reflecting structures such as blood vessels. In [26], the periodicity detection was carried out in the power cepstrum domain. In [13], the liver tissue micro-structure has been described by a three component model: the first component (diffuse) represents randomly positioned scatterers of sufficient concentrations to generate circular-Gaussian statistics; the second component (regular) represents non-randomly distributed coherent scatterers with long-range order (pseudo-periodicity); the third component (short-range order) is due to organ boundaries and blood vessels etc.

All of the above techniques are based on the auto-correlation/power spectrum of the observations, thereby neglect information contained in the Fourier-phase of the *RF* echo. In [28], [9] the *RF* echo was modeled as a cyclo-stationary signal, thus preserving phase information. The

Manuscript submitted in February 1995, revised in January 1996. Major part of support for this work came from the US Army Medical Research grant DAMD17-94-J-4362, the Whitaker Foundation and NSF under grant MIP-955 3227.

U.R. Abeyratne is with the Biomedical Engineering and Science Institute, Drexel University, Philadelphia, PA 19104. E-mail: udantha@cbis.ece.drexel.edu

A.P. Petropulu is with the Electrical and Computer Engineering Dept., Drexel UNiversity, Philadelphia, PA 19104. E-mail: athina@artemis.ece.drexel.edu

J.M. Reid is with the Biomedical Engineering and Science Institute, Drexel University, Philadelphia, PA 19104. E-mail: reid@coe.drexel.edu

embedded periodicity was detected in the frequency domain. That approach seemed to perform better than conventional power-spectral density/cepstra based techniques in detecting periodicity. Both in the cyclo-stationarity approach and the power cepstrum one it was assumed that the diffused scatterer spacings are uncorrelated.

The scatterer spatial correlation has been used in the past to model ultrasonic properties of tissue [11],[15],[16],[8],[4] and was shown to lead to promising tissue signatures. In [16], it was shown that using power spectra, deterministic, membrane-like structures as well as structures consisting of random, diffuse structures can be characterized. In [17], effective scatterer sizes, concentrations and acoustic impedances were investigated using power spectra, as potential tissue signatures. The effective scatterer size was reported to be the most important tissue feature sensed with the method of [17].

In this paper, we use a point scatterer model similar to the ones in [13] and [9] to describe tissue microstructure, with the exception that our model takes the correlations existing among both resolvable and non-resolvable scatterers into account. This enables us to also consider cases of coherent long-range scatterer distributions which have high variances associated with the inter-scatterer spacing, i.e. almost no periodicity, and, non-periodic echos resulting from correlated, non-periodic components of both diffused and structural scatterers. We assume that *RF* echoes are non-Gaussian, on the grounds of empirical/theoretical justifications presented in works such as [25], [6], [3], [24] and [27]. Based on our model for tissue microstructure, we develop schemes for the estimation of resolvable periodicity as well as correlations among non-periodic scatterers. Using higher-order statistics of the scattered signal, we define as tissue "color" a quantity that describes the scatterer spatial correlations, show how to evaluate it from the higher-order correlations of the digitized *RF* scan line segments, and investigate its potential as a tissue signature. The tools employed, i.e., higher-order statistics, were chosen as the most appropriate ones because they suppress Gaussian processes, such as the one arising from the diffused scatterers. Higher-order statistics, unlike second-order statistics, also preserve the Fourier-phase of the signature, the color of the tissue response.

Via computer simulations, we show that the proposed periodicity estimation technique is superior to the widely used power spectrum and cepstrum techniques in terms of the accuracy of estimations. We also preliminary evidence that even when there is no significant periodicity in data, we are still able to characterize tissues using signatures based on the higher-order cumulant structure of the scatterer spacing distribution.

II. Theory

In the following, we use lower case characters to symbolize time domain quantities, and upper case ones to denote frequency domain quantities unless otherwise specifically specified.

Assuming a narrow ultrasound beam, linear propagation and weak scattering in the tissue medium, we model the ultrasonic *RF* echo, $y(t)$, by,

$$y(t) = h(t) * f(t) + w(t), \tag{1}$$

where $h(t)$ is the pulse-echo wavelet of the imaging system, $w(t)$ is the zero-mean observation noise and "*" is the linear convolution operator. The quantity $f(t)$ represents the underlying tissue structure and will be called *the tissue response.*

A. The tissue structure:

Following [5],[13] and [9] we model the structures within tissue that are responsible for backscattered ultrasonic field by point-scatterers organized at different levels. Existing work such as [13] and [9] attempt to characterize liver tissue based on a two component point scatter model: (a) the *diffused component*, which represents [13] randomly positioned scatterers of sufficient concentrations to produce echo signals with circular Gaussian statistics. The positions of individual scatterers are assumed uncorrelated [13]; (b) the *coherent component*, which represents non-randomly distributed scatterers with long-range order [13], [12].

In this paper, we describe liver tissue by a three-component model, which in addition to (a) and (b) above, also takes into account the correlations existing among (i) diffused scatterer locations, (ii) resolvable and unresolvable pseudo-periodic scatterers leading to long range order, and (iii) collection of scatterers leading to short range order, but not strong enough to violate the conditions of weak-scattering or the stationarity of the *RF* echo in a significant manner.

We model the tissue response $f(t)$ by,

$$f(t) = r_d(t) + r_m(t) + r_r(t), \tag{2}$$

where,

- $r_d(t) = \sum_{p=1}^{N_d} a_p \delta(t - \nu_p)$ represents unresolvable diffuse scatterers leading to fully-developed speckle with Gaussian statistics,
- $r_m(t) = \sum_{p=1}^{N_m} b_p \delta(t - \lambda_p)$ represents the combined effects of unresolvable periodicity from structural scatterers, and, correlated non-periodic components of diffused and structural scatterers.
- the term $r_r(t) = \sum_{p=1}^{N_r} v_p \delta(t - \theta_p)$ represents the periodic, resolvable scatterers.

Note that the terms $r_m(t)$ and $r_r(t)$ are non-Gaussian, due to contributions from periodic structures and/or scatterers of short range order.

B. The RF-echo:

From (1) and (2), $y(t)$ can be expressed as:

$$y(t) = y_d(t) + y_m(t) + y_r(t) + w(t), \tag{3}$$

where $y_d(t) = r_d(t) * h(t)$, $y_m(t) = r_m(t) * h(t)$ and $y_r(t) = r_r(t) * h(t)$ are respectively called the *diffused, mixed and resolvable-periodic* components of the *RF* echo $y(t)$. The

observation noise $w(t)$ is assumed zero-mean, Gaussian and uncorrelated with $y_i(t)$, $i = d, m, r$.

Let us assume an infinite extent tissue media, and $N_d, N_m, N_r \rightarrow \infty$. The RF echo $y(t)$ is assumed to be compensated for attenuation. In section 2.3, we discuss the effects of attenuation and finite-extent data on our estimations.

Assuming that the terms $y_i(t)$, $i = d, m, r$ are zero-mean, mutually uncorrelated, the third-order cumulants $c_3^y(\tau_1, \tau_2)$ [19] the process $y(t)$ can be written as:

$$\begin{aligned} c_3^y(\tau_1,\tau_2) &= E\{y(t)y(t+\tau_1)y(t+\tau_2)\}, \\ &= c_3^{y_d}(\tau_1,\tau_2) + c_3^{y_m}(\tau_1,\tau_2) \\ &\quad + c_3^{y_r}(\tau_1,\tau_2), \end{aligned} \tag{4}$$

where $E\{\cdot\}$ is the statistical expectation operator over the ensemble. The third-order cumulants $c_3^w(\tau_1, \tau_2)$ of the noise process $w(t)$ vanishes under the hypothesis that $w(t)$ is Gaussian.

B.1 The diffused component (DC):

We model the diffused component $y_d(t)$ of the RF echo $y(t)$ as a Gaussian process (See also [13]). As such the third-order cumulants sequence equals:

$$c_3^{y_d}(\tau_1,\tau_2) = 0, \quad \forall \tau_1, \tau_2. \tag{5}$$

B.2 The mixed, non-Gaussian component (MC):

The mixed component $y_m(t)$ of the RF echo $y(t)$ is given by:

$$y_m(t) = \left\{ \sum_{p=1}^{N_m} b_p \delta(t - \lambda_p) \right\} * h(t). \tag{6}$$

Let us assume:
(A1) λ_i is uncorrelated to b_j, $i, j = 1, 2, \cdots, N_m$,
(A2) λ_i, $i = 1, 2, \cdots$, form a stationary process, and,
(A3) $y_m(t)$ is a zero-mean process.
Under (A3) the third order cumulants of $y_m(t)$ equal,

$$\begin{aligned} c_3^{y_m}(\tau_1,\tau_2) &= E\{y_m(t)y_m(t+\tau_1)y_m(t+\tau_2)\}, \\ &= M_3^{r_m}(\tau_1,\tau_2) * c_3^h(\tau_1,\tau_2), \end{aligned} \tag{7}$$

with,

$$\begin{aligned} M_3^{r_m}(\tau_1,\tau_2) &= \sum_{p=1}^{N_m}\sum_{q=1}^{N_m}\sum_{s=1}^{N_m} E\{b_p b_q b_s\} \\ &\times E\{\delta(t-\lambda_p)\delta(t+\tau_1-\lambda_q)\delta(t+\tau_2-\lambda_s)\}, \end{aligned} \tag{8}$$

where (A1) has been used in obtaining (8).

Let the joint probability density function (arbitrary) for the scatterer location triplets $\lambda_p, \lambda_q, \lambda_s$ be given by $f_m(\lambda_p, \lambda_q, \lambda_s)$. Then from (8) we obtain:

$$\begin{aligned} M_3^{r_m}(\tau_1,\tau_2) &= \sum_{p=1}^{N_m}\sum_{q=1}^{N_m}\sum_{s=1}^{N_m} E\{b_p b_q b_s\} \\ &\times \int_{-\infty}^{\infty}\int_{-\infty}^{\infty}\int_{-\infty}^{\infty} \delta(t-\lambda_p)\delta(t+\tau_1-\lambda_q)\delta(t+\tau_2-\lambda_s) \\ &\quad \times f_m(\lambda_p,\lambda_q,\lambda_s)\,d\lambda_p\,d\lambda_q\,d\lambda_s \\ &= \sum_{p=1}^{N_m}\sum_{q=1}^{N_m}\sum_{s=1}^{N_m} E\{b_p b_q b_s\} \\ &\quad \times f_m(t, t+\tau_1, t+\tau_2). \end{aligned} \tag{9}$$

Under the assumption (A2), the probability density function $f_m(t, t+\tau_1, t+\tau_2)$ does not depend on the particular t chosen. Thus, $f_m(t, t+\tau_1, t+\tau_2)$ can be written as $f_m(\tau_1, \tau_2)$. Therefore, from (7) and (9) we obtain:

$$c_3^{y_m}(\tau_1,\tau_2) = K_m f_m(\tau_1,\tau_2) * c_3^h(\tau_1,\tau_2), \tag{10}$$

where K_m is given by,

$$K_m = \sum_{p=1}^{N_m}\sum_{q=1}^{N_m}\sum_{r=s}^{N_m} E\{b_p b_q b_s\}. \tag{11}$$

B.3 Resolvable periodic component (RPC):

In the context of ultrasonic tissue characterization, the RPC component has been shown to be of great significance [10], [9]. *To be classified as the resolvable periodic component, the scatterer separation should be regular enough, and the repeat distances should be large enough (compared to the length of the pulse-echo impulse response) to be resolvable.* The Gamma distribution has proven to be a particularly useful tool in describing inter-scatterer space distribution [14], [9], because of its versatility in producing scatterer locations ranging from almost periodic to clearly non-periodic.

The general mathematical description of the RPC follows directly from the expressions derived for the case of MC component. The resolvable periodic component, $y_r(t)$, can be written as:

$$y_r(t) = \left\{ \sum_{p=1}^{N_r} v_p \delta(t - \theta_p) \right\} * h(t). \tag{12}$$

Again, we assume:
(B1) θ_i is uncorrelated to v_j, $i, j = 1, 2, \cdots, N_r$,
(B2) θ_i, $i = 1, 2, \cdots$, froms a stationary process, and,
(B3) $y_r(t)$ is a zero-mean process.
From (12) we can obtain as in the case of MC component,

$$c_3^{y_r}(\tau_1,\tau_2) = K_r f_r(\tau_1,\tau_2) * c_3^h(\tau_1,\tau_2), \tag{13}$$

$$K_r = \sum_{p=1}^{N_r}\sum_{q=1}^{N_r}\sum_{s=1}^{N_r} E\{v_p v_q v_s\}, \tag{14}$$

where the joint probability density function $f_r(\tau_1, \tau_2)$ now describes a (pseudo) periodic phenomenon, i.e. $f_r(\tau_1, \tau_2)$ is a two dimensional bed of spikes, whose separation is equal to the mean-scatterer-spacing.

In the following we derive an expression for $f_r(\tau_1, \tau_2)$, under the constraint that the resolvable periodic scatterers are separated by a constant time interval, T, i.e. the process is strictly periodic and the resolvable periodicity (unknown) is T. Then the periodic component $r_r(t)$ can be written as:

$$r_r(t) = \sum_{p=1}^{N_r} v_p(t)\delta(t - pT), \tag{15}$$

where $v_p(t)$ is the *scatterer strength function*, and is a bounded function defined over the set of real numbers, $\mathcal{R}_{(-\infty,\infty)}$.

The Fourier transform $\tilde{R}_r(\omega)$ of $r_r(t)$ can be obtained as,

$$R_r(\omega) = \frac{2\pi}{T} \sum_{k=-\infty}^{\infty} V(\omega - \frac{2\pi}{T}k), \tag{16}$$

where $V_p(\omega)$ is the Fourier transform of $v_p(t)$. Let the region of support of the function $v_p(t)$ be $\{t : |t| < B\}$. As $B \to \infty$, $V(\omega) \to \delta(\omega)$. As $B \to \infty$ the bispectrum [19] $C_3^{r_r}(\omega_1, \omega_2)$ of $r_r(t)$ is given by:

$$\begin{aligned} C_3^{r_r}(\omega_1, \omega_2) &= R_r(\omega_1)R_r(\omega_2)R_r(-\omega_1 - \omega_2), \\ &= (\frac{2\pi}{T})^3 \sum_{k_1}\sum_{k_2}\sum_{k_3} \delta(\omega_1 - \frac{2\pi}{T}k_1)\delta(\omega_2 - \frac{2\pi}{T}k_2) \\ &\quad \times\delta(-\omega_2 - \omega_1 - \frac{2\pi}{T}k_3), \end{aligned} \tag{17}$$

$$= (\frac{2\pi}{T})^3 \sum_{k_1}\sum_{k_2} \delta(\omega_1 - \frac{2\pi}{T}k_1)\delta(\omega_2 - \frac{2\pi}{T}k_2). \tag{18}$$

For the case $V(\omega) \to \delta(\omega)$, from (12) and (18) we can obtain the bispectrum $C_3^{y_r}(\omega_1, \omega_2)$ of $y_r(t)$ as:

$$\begin{aligned} C_3^{y_r}(\omega_1, \omega_2) &= (\frac{2\pi}{T})^3 \{C_3^h(\omega_1, \omega_2) \sum_{k_1}\sum_{k_2} \delta(\omega_1 - \frac{2\pi}{T}k_1) \\ &\quad \times\delta(\omega_2 - \frac{2\pi}{T}k_2)\}. \end{aligned} \tag{19}$$

The third-order cumulant sequence $c_3^{y_r}(\tau_1, \tau_2)$ of the RPC can be obtained from (19) through an inverse Fourier transform, i.e.,

$$c_3^{y_r}(\tau_1, \tau_2) = c_3^h(\tau_1, \tau_2) * \sum_{k_1}\sum_{k_2} \delta(\tau_1 - k_1T)\delta(\tau_2 - k_2T). \tag{20}$$

Comparing (14) and (20) we get:

$$f_r(\tau_1, \tau_2) = \sum_{k_1}\sum_{k_2} \delta(\tau_1 - k_1T)\delta(\tau_2 - k_2T), \tag{21}$$

Based on (5), (10), and (13), eq. (4) becomes:

$$\begin{aligned} c_3^y(\tau_1, \tau_2) &= \{K_m f_m(\tau_1, \tau_2) + K_r f_r(\tau_1, \tau_2)\} * c_3^h(\tau_1, \tau_2), \\ &= \{K_m f_m(\tau_1, \tau_2) + \sum_{k_1}\sum_{k_2} \delta(\tau_1 - k_1T)\delta(\tau_2 - k_2T)\} \\ &\quad *c_3^h(\tau_1, \tau_2), \end{aligned} \tag{22}$$

when the inter-scatterer spacing of the RPC component is a constant T.

C. The proposed method for the estimation of periodicity

From (18) and (22) we observe that the periodicity manifests itself in both bispectrum and the third order cumulant domains. In the cumulant domain, peaks are separated by the period T, while in the bispectrum domain the separation is $\frac{2\pi}{T}$ rad/S. Let us form the weighted 3^{rd}-order cumulant projection (see also [2],[1]) of (22) as follows:

$$\begin{aligned} p_3^y(\tau_1, \omega) &= \sum_{\tau_2} c_3^y(\tau_1, \tau_2)e^{j\omega\tau_2}, \quad 0 \le \omega < 2\pi, \qquad (23) \\ &= p_3^m(\tau_1, \omega) + p_3^r(\tau_1, \omega). \qquad (24) \end{aligned}$$

From (23), $p_3^y(\tau_1, \omega)$ can be viewed as the one-dimensional Fourier transform of $c_3^y(\tau_1, \tau_2)$ with respect to the variable τ_2. According to this interpretation, $p_3^m(\tau_1, \omega)$ equals:

$$\begin{aligned} p_3^m(\tau_1, \omega) &= F_{\tau_2}\left\{c_3^{y_m}(\tau_1, \tau_2)\right\}, \\ &= K_m F_{\tau_2}\left\{f_m(\tau_1, \tau_2) * c_3^h(\tau_1, \tau_2)\right\}, \end{aligned} \tag{25}$$

and also

$$\begin{aligned} p_3^r(\tau_1, \omega) &= F_{\tau_2}\left\{(c_3^{y_r}(\tau_1, \tau_2))\right\}, \\ &= F_{\tau_2}\{c_3^h(\tau_1, \tau_2)\} \sum_{k_1}\sum_{k_2} \delta(\tau_1 - k_1T)\delta(\omega - \frac{2\pi}{T}k_2), \end{aligned} \tag{26}$$

where $F_{\tau_2}\{\cdot\}$ is the one-dimensional Fourier transform with respect to the variable τ_2, and $c_3^{y_m}(\tau_1, \tau_2)$ and $c_3^{y_r}(\tau_1, \tau_2)$ are given by (10) and (20).

Based on (26) the periodicity can be estimated from the $p_3^y(\tau_1, \omega)$ as the separation T between peaks along the τ_1-axis. Along the ω-axis, the peaks are separated by the amount $2\pi/T$.

D. The estimation of the color of the tissue response

When the tissue under study shows no periodic variations in ultrasonic properties, the periodicity will loose its significance as a tissue signature. In the following we define a new quantity, the *color of the tissue response* to supplement periodicity as a tissue signature.

The contribution of the MC to the third-order cumulants of the RF echo is described by (10). The term $K_m f_m(\tau_1, \tau_2)$ can be viewed as the third-order moment sequence of the signal:

$$s(t) = e(t) * g(t), \tag{27}$$

where $e(t)$ is an *i.i.d.*, non-Gaussian, zero-mean noise process, whose skewness is K_m, and, $g(t)$ is the signal whose third-order moment sequence is given by $f_m(\tau_1, \tau_2)$.

We will refer to $g(t)$ as the "color of the tissue response". The time domain equivalent of (10) becomes:

$$z(t) = e(t) * u(t), \tag{28}$$

where $u(t) = g(t) * h(t)$ will be referred to as the *combined kernel.*

Assuming, that the support of the third-order cumulant sequence $c_3^z(\tau_1, \tau_2)$ of $z(t)$ is contained in a square defined

by $|\tau_1|, |\tau_2| < T$, where T is the resolvable periodicity, we can recover the term $c_3^z(\tau_1, \tau_2)$, from $c_3^y(\tau_1, \tau_2)$ as:

$$c_3^z(\tau_1, \tau_2) = c_3^y(\tau_1, \tau_2), \quad |\tau_1|, |\tau_2| \leq T_0, \tag{29}$$

where $T_0 \approx T$ and T is the known or estimated period of the RF data. Note that a precise knowledge of T is not required.

Applying methods of system reconstruction from higher-order spectra, [19], [2], [1], we can retrieve $u(t)$ from $c_3^z(\tau_1, \tau_2)$ within a scalar and a time delay. In the work of this paper, we used the α-WCP based method of system reconstruction proposed in [2], exploiting its low computational load.

The color of the tissue response, $g(t)$, compactly summarizes both phase and magnitude information available in the tissue response $f(t)$.

The quantities $u_i(t)$ and $u_j(t)$ obtained from two different A-lines "i" and "j" can be written as:

$$u_i(t) = h(t) * g_i(t), \tag{30}$$

$$u_j(t) = h(t) * g_j(t), \tag{31}$$

where $h(t)$, the pulse-echo impulse response of the imaging system, can be assumed to be invariant between the two locations "i" and "j"; $g_i(t)$ and $g_j(t)$ respectively represent the color of the tissue responses at "i" and "j". The quantities $g_k(t)$, $k = 1, 2, \cdots$, summarizes information about the tissue, and is also free from the effects of $h(t)$, making it a good candidate for a tissue signature.

Using (30) and (31) we form a tissue signature $S_{ij}(t)$, in the time domain, as follows:

$$\begin{aligned} S_{ij}(t) &= u_i(t) * \{u_j(t)\}^{-1}, \\ &= h(t) * g_i(t) * \{h(t) * g_j(t)\}^{-1}, \\ &= g_i(t) * g_j^{-1}(t), \end{aligned} \tag{32}$$

where $\{\cdot\}^{-1}$ denotes the convolutional inverse.

If the estimations are from two regions with similar ultrasonic properties, for instance from two healthy regions of a liver, $S_{ij}(t)$ will approach a Dirac delta-function. On the otherhand, if the two estimates are from two regions inside and outside a tumor which has brought in a change in the inter-scatter spacing distribution, then $S_{ij}(t)$ and will depart from Dirac delta. Thus, the closeness of S_{ij} to a Dirac delta performs as a relative tissue signature. We will estimate S_{ij} from clinical images and validate its usefulness as a signature.

The quantities $g_i(t)$ and $g_i(t)$ can individually be obtained from (30) and (31) using a blind deconvolution technique [21], i.e. a technique through which the input to a system can be obtained when only its output is known. Preliminary results of a blind deconvolution approach to separate $g_i(t)$ and $g_i(t)$ have been reported in [4].

E. The effects of attenuation and finite data lengths

The results in *Section 2* were derived under the assumption of an infinite tissue media. However, in practice we have access to only finite-length data records. With such records, one can obtain, parallel to the situation in autocorrelation estimation from finite data, only a statistical estimate of the true higher-order cumulants of RF data. Expressions for the statistical properties of HOS estimators can be found in [19]. Similar to the power spectrum domain, in the bispectrum domain (and in $p_3^y(\tau_1, \omega)$), the finite data records limit the smallest period that can be detected.

Attenuation represents all forms of energy loss experienced by a propagating pulse and is unavoidable in biological media. The effects of attenuation on the pulse at the depth $x = vt_0/2$, where v is the ultrasonic propagation velocity and t_0 is time, in tissue space can be represented as [18]:

$$\tilde{H}(t_0, \omega) = A(t_0, \omega)H(\omega), \tag{33}$$

where $\tilde{H}(t_0, \omega)$ and $A(t_0, \omega)$ are respectively the Fourier transforms of space-dependent pulse echo response and attenuation; $H(\omega)$ is the Fourier transform of the pulse transmitted.

Eq.(33) can be written in the time domain as:

$$\tilde{h}(t_0, t) = a(t_0, t) * h(t), \tag{34}$$

where $\tilde{h}(t_0, t)$, $a(t_0, t)$ and $h(\omega)$ are the time domain equivalents of $\tilde{H}(t_0, \omega)$, $A(t_0, \omega)$ and $H(\omega)$ respectively.

For short data records, we can ignore the t_0-dependency of (34) and consider $\tilde{h}(t_0, t)$ as a time-invariant quantity. Then the effect of attenuation on our period estimation techniques follows directly from (22), and (26) with the quantity $c_3^h(\tau_1, \tau_2)$ replaced by the third-order cumulant sequence $c_3^{\tilde{h}}(\tau_1, \tau_2)$ of $\tilde{h}(t_0, t)$.

In estimating the color of the tissue response, the combined kernels $u_i(t)$ and $u_j(t)$ (see (30) and (31)) now takes the form,

$$u_i(t) = a_i(t_0, t) * g_i(t) * h(t), \tag{35}$$

$$u_j(t) = a_j(t_0, t) * g_j(t) * h(t), \tag{36}$$

resulting in a tissue signature S_{ij} given by,

$$\begin{aligned} S_{ij}(t) &= u_i(t) * \{u_j(t)\}^{-1}, \\ &= g_i(t) * g_j^{-1}(t) * a_i(t_0, t) * a_j(t_0, t)^{-1}. \end{aligned} \tag{37}$$

From (37) we note that the differences in attenuation characteristics at locations "i" and "j" are also captured in S_{ij}.

III. Data collection

A. Simulated data

We simulated digitized ultrasound RF scan lines on a computer, using a model similar to the ones used in [14], [9] and [7]. Scatterers were modeled as a collection of points, distributed according to some probability density function. A uniform probability density function described both inter-scatterer spacings and the scattering strengths related to the DC component. The RPC scatterer spacings were described by a Γ-probability density functions,

because of the relative ease with which one can obtain inter-scatterer spacings ranging form almost periodic to uniform. Scatterer strengths were also modeled with a Γ-density function with a different set of parameters. The quantity $\frac{\sigma}{\mu}$, where μ is the mean and σ is the standard deviation, of the scatter-strength distribution was set to 0.35, so that we get a wide variation in strengths. The program also had the capacity to simulate correlated scatteres contributing to the MC component, via another Γ-distribution. The correlations in the scatterer spacings were obtained by filtering them through a linear, time invariant system of arbitrary frequency response.

Observation noise, which is unavoidable in any physical measurement, was modeled by a zero-mean Gaussian process as is commonly done. Observation noise was allowed to be a colored process.

The center frequency of the transducer was $4.2MHz$; the pulse envelope followed a Gaussian shape and its $3dB$ bandwidth was $2.5MHz$. The sampling frequency of the data acquisition was selected to be $20MHz$.

B. Clinical data

To demonstrate the performance of our method under clinical conditions, we used liver scans of healthy volunteers, (volunteer nos. I and II) and a patient (hypoechoic tumor of the liver) imaged by ultrasonologists at the Thomas Jefferson University Hospital, Philadelphia, on a model UltraMark-9 system manufactured by Advanced Technology Laboratories, Seattle, U.S.A. A linear array, sector scanner with a nominal center frequency of 3.5 MHz and a field of vision 60° was used as the transducer. In the cases of the volunteer-I and the patient, the focus at transmission was set at a depth of $20mm$ (approx.); multi-focusing had been used for the volunteer-II, with focii set at depths of 77, 100 and 125 mms (approx.). Dynamic focusing was applied in the receiving mode. The data were sampled at 12 MHz.

IV. Results

A. Cumulant estimation procedure

Both of the tissue signatures proposed in this paper rely on computing the third-order cumulants from digitized RF scan line segments. In the following we describe the procedure followed to estimate them. In the following, we assume $y(k)$ to be an ergodic process.

(S1) Segment the i-th data record $y_i(k)$ into K records of length N samples each; subtract the mean of each record to form the zero-mean sub-segments $y_{ij}(k)$.

(S2) Estimate the third-order cumulants $\hat{c}_{y_{ij}}(\tau,\rho)$ of each sub-segment $y_{ij}(k)$, $j = 0, 2 \cdots K-1$ according to:

$$\hat{c}_{y_{ij}}(\tau,\rho) = \frac{1}{N}\sum_{k=0}^{N-1} y_{ij}(k)y_{ij}(k+\tau)y_{ij}(k+\rho), \quad |\tau| \le M, |\rho| \le M \qquad (38)$$

where M is the length of third-order correlation lags considered in the computation.

(S3) Average the cumulant estimates $\hat{c}_{y_{ij}}(\tau,\rho)$ over all sub-segments $j = 0, 1 \cdots K-1$ to obtain the cumulant estimate $\hat{c}_{y_i}(\tau,\rho)$ corresponding to the data record $y_i(k)$:

$$\hat{c}_{y_i}(\tau,\rho) = \frac{1}{K}\sum_{j=0}^{K-1} \hat{c}_{y_{ij}}(\tau,\rho), \qquad (39)$$

B. Estimating the periodicity

B.1 Simulation I

In this experiment, we compare the proposed method to detect periodicity (see eq. (23)), with the power spectrum [10] and power cepstrum [26] techniques. Only the RPC component of the RF echo was considered. We simulated the inter-scatterer spacing with the Γ-density function, for $v = \sigma/\mu = 0.03, 0.15,$ and, 0.35, where μ and σ respectively denote the mean and the standard deviation of the scatter-spacings. The nominal mean scatterer spacing was $\mu = 1.0mm$.

Cumulants for the process were estimated according to the procedure (S1)-(S3) with the following parameters: $M = 100$, $N = 256$, $K = 4$. Fig. 1(a),(b) and (c) show the contour maps of the estimated cumulants corresponding to $v = 0.03, 0.15, 0.35$.

Based on the cumulant estimates, $|p_3^y(\tau_1,\omega)|$, $0 \le \omega < \pi$, was computed through (23), and its contour map is shown in Fig. 1 (d),(e) and (f) for $v = 0.03, 0.15$ and 0.35 respectively.

The periodicity in data is evident from both the cumulants and in $p_3^y(\tau_1,\omega)$. However, they are better visualized in Fig.1 (g),(h) and (i), which were obtained by projecting the absolute values of Fig. 1 (d), (e) and (f) along frequency axes, followed by smoothing. The dotted lines in Fig. 1 (g),(h) and (i) correspond to the true mean scatterer spacing, $1.00mm$.

Periodicity can also be estimated from the ω-axis of $p_3^y(\tau_1,\omega)$; Fig. 2 (a), (b) and (c) respectively show $|p_3^y(\tau_1,\omega)|$, $0 \le \omega < \pi$, corresponding to $\tau_1 = 0.0, 1.0$ and 2.0 mm (see Fig.1 (d),(e),(f) and eq. (26)). The spacings between adjacent spectral peaks, which is given by $2\pi/T$ according to (26), can be obtained from Fig. 2 (a), (b) and (c) and periodicity be determined.

Next we computed the power spectrum and the power cepstra of the same set of data. Data were segmented exactly the same way as for the cumulant estimates, and the average autocorrelation over segments obtained. The autocorrelation estimates were smoothed through a Blackman window, before computing the power spectrum. Fig. 3 (a), (b) ,(c) show the power spectra estimated for the cases $v = 0.03, 0.15$ and 0.35. Note that the power spectrum reveals the periodicity only for the case $v = 0.03$, which corresponds to an almost periodic scatter spacings. Based on power spectra, the power cepstra illustrated in Fig. 3 (d),(e) and (f) were computed; the dotted lines in these figure corresponds to the true mean scatter spacing, 1.0 mm. The power cepstrum shows a well localized peak for $v = 0.03$ and a reasonably well localized peak for the case

$v = 0.15$. However, it shows a large spurious peak for the case $v = 0.35$ which overshadows the true peak.

We ran 50 Monte Carlo runs on the mean scatterer-spacing, based on the power cepstrum and the proposed method, corresponding to the case $v = 0.15$, and the mean-scatterer-spacing= $1.0mm$. Due to poor performance, the power spectrum method was excluded. In estimating the periodicity via the proposed method, the first peak location was obtained as the location corresponding to the highest peak in the region 0.4-2.5 mm. The same procedure was used in the case of the power cepstrum method. Table I illustrates the results we obtained. These results illustrate that the proposed method outperforms the power cepstrum in estimating periodicity.

Better estimates of the cepstrum can be obtained with parametric methods such as the AR approach considered in [26], when the model order is known fairly accurately. However, the estimation of the model order is not always a trivial task. In this paper, our use of non-parametric techniques to compute the power cepstrum is justified because we used non-parametric techniques to compute higher-order cumulants too.

B.2 Simulation II

In this simulation, we generated the RPC component as in *Simulation I* and added a DC component at a signal to noise ratio, $SNR = -16\ dB$, where, following [9] the SNR is defined as:

$$SNR = 10 \log_{10} \left\{ \frac{\sum_k y_r(k)^2}{N_r \sum_k y_d(k)^2} \right\}, \qquad (40)$$

where N_r is the number of resolvable scatterers in the data segment considered. If the normalization term N_r is not included, the SNR measure does not represent the true situation. For instance, there can be cases with only a few resolvable scatterers over a long tissue length, where the energy per scatterer is high enough so that the periodicity can be determined without processing the signal, but still leading to a misleadingly low SNR measure.

Fig. 4 illustrates the results of the proposed method and the power cepstrum one. Fig. 4 (a), (b), (c) show $|p_3^y(\tau_1, \omega)|$ projected along the ω-axis for cases $v = 0.03, 0.15, 0.35$. Fig. 4 (d), (e), (f) show the power cepstra corresponding to $v = 0.03, 0.15, 0.35$. Periodicities obtained from Fig. 4 (a), (b), (c) are: 0.97, 1.00, 0.96 mm. Periodicities obtained from Fig. 4 (d), (f) are: 0.96 and 0.88 mm. The result form (e) is inconclusive; there are several spurious peaks, two major ones corresponding to periodicities of 0.74 mm and 1.2 mm.

Figs. 1, 4 and Table 1 suggest that the higher-order statistics based periodicity estimation technique proposed in this paper outperforms both the power spectrum and the power cepstrum.

A problem often encountered with the power cepstrum is that it tends to produce spurious peaks in the presence of noise. Power cepstrum computations are heavily affected by the DC component and also the observation noise in RF echoes. Any noise escaped through the averaging and windowing operations at the auto-correlation estimation process, may contribute a large, slowly decaying component to the power cepstrum, thus masking small peaks. Spurious peaks pose a serious problem to the periodicity detection/estimation process. Fig. 4 indicates the fact that in the presense of the DC, the problem of spurious peaks gets aggravated. Since HOS suppresses the DC component and measurement noise, the proposed technique is robust against their unwanted effects.

B.3 Clinical data: *Normal subjects:*

In this section, we present the periodicities estimated from clinical images, using the higher-order techniques. In all clinical images, we used $M = 80$, $N = 128$ and $K = 5$. Each segment corresponded to a length of 8 mm (approx.) in tissue.

Fig. 5 illustrates results corresponding to a normal liver (*volunteer-I*). Contour maps of $|p_3^y(\tau_1, \omega)|$, $0 \leq \omega < \pi$ is shown in Fig. 5 (a), and its smoothed projection along the ω-axis is shown in Fig. 5 (b). The power spectrum and the power cepstrum computed from the same data using the same parameters as those used in the computation of cumulants, are illustrated in Fig. 5 (c) and (d).

The period estimated from the cepstrum and the proposed method are respectively 1.28 mm, and $1.3mm$. Periodicity is much more evident in Fig. 5 (a), (b), which suggests that the proposed method is better than both the power cepstrum and the power spectrum. From the power cepstrum/spectrum it is impossible to see repeated peaks confirming a suspected periodicity, whereas repeated peaks are clearly seen in higher-order estimates.

Fig. 6(a) shows the quadrature demodulated, logarithmically compressed liver image of *volunteer-I*; the histogram of estimated periods obtained from throughout the image, where periodicity could be detected, is shown in Fig. 6(b). The average value of the period evaluated using the proposed method over 80 estimations was 1.03 mm, at a standard deviation of 0.26 mm. Fig. 6(c) and (d) show similar results for the volunteer number II, where the average=1.07 mm and the standard deviation = 0.25 mm. In these images, periodicities were estimated in a depth of approx. 35 mm - 51 mm from the transducer surface.

B.4 Clinical data: *tumor of the liver:*

In this section we report the results of our attempts to estimate periodicities from focal diseases of the liver. We obtained a clinical image of a patient diagnosed with a hypo-echoic tumor of the liver (see section 3.2) and applied higher order periodicity detection schemes proposed in this paper. Fig. 7 (a) shows a part of the image we used. Periodicities were estimated at a depth of 48-65 mm from the transducer surface. The focus of the imaging system at transmission had been set at about 20 mm from the transducer surface; dynamic focusing was used in the receive mode. In this simulation, we used $M = 80$, $N = 128$ and $K = 5$.

Fig. 7(b) shows the histograms of the periodicities estimated using the proposed method from within and out-

side the tumor. The mean and the standard deviation of the scatterer spacing obtained from within the tumor are respectively 1.07 and 0.42 *mm*. For regions outside the tumor, corresponding values were 0.97 and 0.31 *mm*.

Based on Fig. 7 we conclude that there is no significant difference in periodicity within and outside the tumor. These results highlight the fact that there are important clinical situations where the periodicity detection fails to delineate normal from abnormal tissue. This can happen either because there is no discernible change in the periodicity inside and outside the diseased area, or there is no periodicity associated with the concerned tissues at all, irrespective of normal or diseased.

In the following, we investigate the performance of the color of the tissue response as a tissue signature in such situations.

C. Estimating the color of the tissue response

C.1 Simulated data

We simulated two realizations of digitized *RF* scan line segments corresponding to two differently-correlated, inter-scatterer spacings. In the first case an *RPC* component was generated with $v = 0.05$. The simulated *RF* echo was close to purely periodic, whose cumulants sequence was only slightly affected near the origin by the slight variations in the inter-scatterer spacings. This served as our first digitized *RF* scan line segment under study.

In the second, we used $v = 0.35$ in the *RPC* component resulting in a digitized *RF* scan line segment with wider changes in the inter-scatterer spacings, thus contributing to the third order cumulant near the origin, i.e. change the statistical color of the *RF* echo. Another component from unresolvable correlated scatterers were simulated with another Γ distribution, withe $\sigma/\mu = 0.8$, and $\mu = 0.3$ *mm*, i.e. inter-scatterer spacing distribution was almost non-periodic. Correlations were further introduced to the spacings by filtering them through a linear time invariant system of arbitrary frequency response. The echo corresponding to this scatterer distribution was taken as the second realization of the digitized *RF* scan line segment.

To both of these realizations, a *DC* was added at a $SNR = -17dB$, defined according to (40) to get the two digitized *RF* scan line segments $y_1(k)$ and $y_2(k)$. In order to simulate the effect of observation noise, we added white, Gaussian noise at a signal to noise ratio $S/N = 10dB$, where the ratio S/N was defined to be:

$$S/N = 10\log_{10}\left\{\frac{\sum_k y_i(k)^2}{\sum_k w(k)^2}\right\},\ i = 1,2 \qquad (41)$$

where $y_i(k)$, $i = 1,2$ are the two digitized *RF* scan lines under study and $w(k)$ is the observation noise.

From the two sets of digitized *RF* scan line segments $y_1(k)$ and $y_2(k)$ so generated, we estimated the third-order cumulant sequences $c_3^{y_1}(\tau_1,\tau_2)$ and $c_3^{y_2}(\tau_1,\tau_2)$ according to steps *S*1-*S*4. To separate the non-periodic parts $c_3^{z_1}(\tau_1,\tau_2)$ and $c_3^{z_2}(\tau_1,\tau_2)$ from $c_3^{y_i}(\tau_1,\tau_2)$, $i = 1,2$, and to reduce the estimation variance associated with the cumulants, we applied a *minimum bispectrum bias supremum* window of length M on the cumulant sequence obtained through steps *S*1-*S*4. We used $M = 30$, $N = 128$ and $K = 8$, in following *S*1-*S*4.

Fig. 8(a) shows the results of 50 Monte carlo runs for the quantity $u_1(k) = g_1(k) * h(k)$ estimated through the methods of *section 2.2* , based on 50 realizations of the digitized *RF* scan line segments corresponding to $v = 0.05$, i.e. $y_1(k)$. The average value over 50 runs is shown in a solid line. The shaded area represents the average $\pm$ standard deviation. The dash-dotted line indicates the true ultrasonic pulse used in the simulations. Fig. 8(b) shows the corresponding figure obtained with 50 realization of $y_2(k)$. It can be seen that the contributions of the correlated scatterer locations affect the estimated combined kernel $u_2(k)$. However, from Fig. 8 we can see that the larger quantity $h(t)$ masks the smaller differences between $u_1(k)$ and $u_2(k)$.

We formed the estimator S_{ij}, $i = 1,2, j = 1$ according to (32). Fig. 8(c) indicates the result S_{11} over 50 Monte Carlo runs; S_{21} is shown in Fig. 8(d). The average estimate is shown in a solid line, while the shaded area represents average $\pm$ one standard deviation. Fig. 8 suggests that our estimator S_{ij}, $i = 1,2, j = 1$ is capable of detecting the color difference between $y_1(k)$ and $y_2(k)$.

C.2 Clinical data

To investigate the performance of the color of the tissue response as a signature in clinical situations, we attempted estimating the color of the tissue response measure S_{ij} from images of the liver shown in Fig. 7(a). In estimating the cumulants we used $N = 128$, $M = 25$ and $K = 3$, where the three segments corresponding to $K = 3$ came form three adjacent A-lines located at the same depth of the image, i.e. from each A-line we considered data segments of length 128 samples (8 *mm* in tissue space).

Fig. 9(a) and (b) show the quantities $u_1(t)$ and $u_2(t)$ estimated respectively from within and outside the tumor. Solid line indicates the average estimate, while the shaded area represents average $\pm$ one standard deviation. The estimates S_{11} and S_{21} are shown in Figs. 9(c) and (d).

Fig. 9(c) and (d) show the color of the tissue response estimated from within and outside the tumor. In forming the convolutional inverse $u_j(k)^{-1}$ (see 32), we used the average of 20 combined kernels estimated within the tumor. According to Fig. 9, it is possible to delineate the tumor region from normal tissue using the estimate S_{ij}, $i = 1,2, j = 1$. The closeness of the estimator to a Dirac-delta function can be used as a relative tissue signature in the present case.

Note that the variations in the estimations, i.e. the shaded areas in the figures, are not entirely due to statistical estimation errors. It has been shown in [1], [2], that using the same higher-order estimation techniques, under similar conditions, one can achieve a much smaller variance. A major reason for the seemingly larger variance is the effects of natural biological variations of the scatterer spacing distributions among A-lines across the image, i.e. natural differences in the color of the tissue response be-

tween different A-lines.

V. Discussion and Conclusions

We modeled biological tissue as a collection of point scatterers positioned in a uniform non-scattering media. Based on the higher order statistics of scatterer spacings, we derived a technique to estimate mean-scatterer spacing, which has received a lot of attention in the past as a potential tissue signature for organs with periodic variation of ultrasonic properties. We also proposed a higher-order-spectra based tissue signature, the color of the tissue response to supplement situation where there is no periodicity or periodicity fails to delineate normal from abnormal tissue.

Using simulated data, it was shown that the periodicity can be better visualized and detected in the higher-order spectra domain. Since zero-mean Gaussian processes are suppressed in higher-order domain, the proposed method is robust against additive measurement noise unavoidable in data acquisition. Microscopic, diffuse scatterers of the size of individual cells often lead to *RF*-echos with circular Gaussian statistics. Thus the proposed method is insensitive, unlike power spectra/cepstra techniques, to the diffused component, because of the property that *HOS* suppress Gaussian processes. This makes the higher-order spectra domain a well suited place to estimate periodicity associated with medical ultrasound data.

The periodicity has been proposed as a potential tissue signature in detecting liver diffuse diseases such as cirrhosis and chronic hepatitis [13], [10]. Using the higher-order statistics based schemes proposed in this paper, we estimated resolvable periodicities from healthy livers and a liver with a hypo-echoic tumor. Although we were able to detect and estimate periodicity from all images, we observed that there is no significant difference in the mean-scatter-spacing estimated from within and outside the tumor under study.

Detecting and estimating periodicity from clinical data is not always a simple task. In methods such as [10], [13], the presence of coherently reflecting blood vessels, for instance, confuse the periodicity estimation process. There are also a lot of biological variations and imaging-equipment dependent factors such as the focus points of the system, beam width etc. which compromise the definition of periodicity, and its estimation. Tumors are highly irregular, complex structures whose organization depends on the type of the tumor and the stage of growth. There can be regions of necrosis, and regions with various levels of perfusion, served by a network of haphazardly developed blood vessels [23]. Even when the organ under study has periodic ultrasonic properties, there can be situations where there is no characteristic period which would have enabled us to detect abnormalities. It is plausible to expect such situations in the presence of a malignant tumor growing dendrites into a periodic structure, such as the liver. Methods that can only estimate periodicities associated with resolvable scatterers will not be able to capture the true picture in such cases.

The higher-order spectra based tissue signature, the color of the tissue response proposed in this paper, compactly summarizes the correlation structure existing among the scatterers of both short-range and long-range order. It is largely independent of the axial pulse echo impulse response of the imaging system $h(t)$, and also, does not require the *RF* echo be periodic. Therefore, the color of the tissue response can perform as a tissue signature which supplements the periodicity, and be measured even when the periodicity is not defined. Correlated, unresolvable scatterers can be expected in situations such as the tumor micro-vasculature. Since our model includes the correlations among unresolvable scatterers, the effects of micro-vasculature is automatically included.

We estimated the color of the tissue response from within and outside of a hypo-echoic tumor of the liver. We observed different colors of the tissue responses for the two cases, indicating characteristic scatter correlation structures inside and outside the tumor. Currently, investigations are under way to devise tumor detection schemes based on the color of the tissue response, as observed from *RF* data corresponding to traditional B-scan images.

VI. Acknowledgment

The authors wish to thank the associate editor for coordinating the review of this paper, and the anonymous reviewers whose comments dramatically improved the technical content of this paper. The also wish to thank the Radiology Department at Thomas Jefferson University Hospital, Philadelphia, Pennsylvania, for providing the clinical images described in section 3.2, *clinical data.*

References

[1] U.R. Abeyratne, A.P. Petropulu, "System Reconstruction from Weighted Cumulant Projections, *IEEE Tr. on Signal Processing*, submitted in 1995.

[2] U.R. Abeyratne, A.P. Petropulu, "α-Weighted Cumulant Projections: A Novel Tool For System Identification", *Twenty-Ninth Annual Asilomar Conference on Signals, Systems and Computers*, California, Oct. 1995.

[3] U. R. Abeyratne, A. P. Petropulu, J. M. Reid, "Higher Order Spectra Based Deconvolution of Ultrasound Images", *IEEE Trans. on Ultr., Ferroelec. and Frequency Control*, vol. 42, no.6, pp. 1064-1075, 1995.

[4] U. R. Abeyratne, A. P. Petropulu, J. M. Reid, "Higher Order Spectra Based Deconvolution of Ultrasound Images", *1995 IEEE Workshop on Nonlinear Signal and Image Processing*, Neos Marmaras, Greece, 1995.

[5] J.C. Bamber, "Theoretical Modelling of the Acoustic Scattering Structure of Human Liver", *Acoustic Letters*, Vol.3, No. 6, pp. 114-119, 1979.

[6] J.-F. Chen, J.A. Zagzebski, and E.L. Madsen, "Non-Gaussian Vs. Non-Rayleigh Statistical Properties of Ultrasound Echo Signals", *IEEE Tr. on Ultrasonics, Ferroelec., and Frequency Control*, vol. 41, no. 4, pp. 435-440, 1994.

[7] F.S. Cohen and G. Georgiou, "Detecting and Estimating Structure Regularity of Soft Tissue Organs From Ultrasound Images", *International Conference on Image Processing*, Washington D.C., October, 1995.

[8] F.S. Cohen, "Modeling of Ultrasound Speckle with Application in Flaw Detection in Metals", *IEEE Tr. on Signal Processing*, vol. 40, no. 3, pp. 624-632, 1992.

[9] K.D. Donohue, J.M. Bressler, T. Varghese and N.M. Bilgutay, "Spectral Correlation in Ultrasonic Pulse-echo Signal Processing", *IEEE Tr. on Ultrasonics, Ferroelec., and Frequency Control*, vol. 40, no. 4, pp.330-337, 1993.

[10] L. L. Fellingham and F.G. Sommer, "Ultrasonic Characterization of Tissue Structure in the *In Vivo* Human Liver and Spleen", *IEEE Trans. on Sonics and Ultr.*, vol. SU-31, No-4, pp 418-428, 1984.

[11] J.C. Gore, S. Leeman, C. Metreweli, N.J. Plessner, K. Willson, "Dynamic Autocorrelation Analysis of A-scans *in-vivo*", *Ultrasonic Tissue Characterization II*, M. Linzer (ed.), National Bureau of Standards, Washington, D.C, pp. 275-280, 1979.

[12] J.F. Greenleaf and C.M. Sehgal, **Biologic System Evaluation with Ultrasound**, Springer-Verlag, New York, 1992.

[13] M.F. Insana, R.F. Wagner, B.S. Garra, D.G. Brown and T.H. Shawker, "Analysis of ultrasound image texture via generalized Rician statistics", *Optical Engineering*, Vol. 25, No. 6, pp. 743-748, 1986.

[14] L. Landini and L. Verrazzani, " Spectral characterization of tissue microstructure by ultrasound: A stochastic approach", *IEEE Tr. Ultra.,Ferroelec. and Freq. Control*, vol. 37, pp 448-456, 1990.

[15] F.L. Lizzi, "Clinical Spectrum Analysis Techniques for Tissue Characterization", *Ultrasonic Tissue Characterization II*, M. Linzer (ed.), National Bureau of Standards, Washington, D.C, pp. 111-119, 1979.

[16] F.L. Lizzi, M. Greenebaum, E.J. Feleppa, M. Elbaum, D.J. Coleman, "Theoretical Framework for Spectrum Analysis in Ultrasonic Tissue Characterization", *J. Acoust. Soc. Am.*, 73(4), pp. 1366-1373, 1983.

[17] F.L. Lizzi, M. Ostromogilsky, E.J. Feleppa, M. Rorke, M.M. Yaremko, "Relationship of Ultrasonic Spectral Parameters to Features of Tissue Microstructure", *IEEE Tr. on Ultr. Ferroelec. and Frequency Control*, 33(3), pp 319-329, 1986.

[18] A. Lymberis, A. Herment, G. Demoment and C. Fric, "Estimation of Frequency-Dependent Attenuation Based on parametric Spectral Analysis and Correlation Lags of the Demodulated Echo Signal", *Ultrasonic Imaging*, vol. 13, pp. 1-26, 1991.

[19] C. L. Nikias and A.P. Petropulu, **Higher-Order Spectra Analysis: A Nonlinear Signal Processing Framework**, Prentice Hall Incorporated, Oppenheim Series in Signal Processing, 1993.

[20] A.V.Oppenheim and R.W. Schafer, **Discrete Time Signal Processing**, Prentice-Hall Inc., Englewood Cliffs, New Jersey, 1989.

[21] A. P. Petropulu and C. L. Nikias, "Blind Deconvolution Using Signal Reconstruction from Partial Higher Order Cepstral Information", *IEEE Trans. on Signal Processing*, Vol. 41, No. 6, pp 2088-2095, 1993.

[22] J.M.Reid, "The Measurement of Scattering", in *Tissue Characterization with Ultrasound*, CRC Press, Boca Raton, Florida, pp.81-114, 1986.

[23] A.A. Shah-Yukich and A.C. Nelson, "Characterization of Solid Tumor microvasculature: A Three Dimensional Analysis Using the Polymor Casting Technique", *Lab. Invest.*, vol. 58, pp. 236-244, 1988.

[24] P. M. Shanker, J. M. Reid, H. Ortega, C. W. Piccoli and B. B. Goldberg, "Use of Non-Rayleigh Statistics for the Identification of Tumors in Ultrasonic B-Scans of the Breast", *IEEE Trans. on Medical Imaging*, Vol. 12, pp 687-692, 1993.

[25] R. H. Tuthill, R. H. Sperry and K. J. Parker, "Deviations From Rayleigh Statistics in Ultrasound Speckle", *Ultrasonic Imaging*, 10, pp 81-89, 1988.

[26] K.A. Wear, R.F. Wagner, M.F. Insana and T.J. Hall, "Application of Autoregressive Spectral Analysis to Cepstral Estimation of Mean Scatterer Spacing", *IEEE Tr. on Ultrasonics, Ferroelec., and Frequency Control*, vol. 40, no. 1, pp. 50-58, 1993.

[27] L. Weng, J.M. Reid, P.M. Shanker, K. Soetanto and X.-M. Lu, "Nonuniform phase distribution in ultrasound speckle analysis-Part I: Background and experimental demonstration", *IEEE Tr. Ultrasonics, Ferroelec., and Frequency Control*, Vol. 39, pp 352-359, 1992.

[28] T. Varghese and K.D. Donohue, "Characterization of Tissue Microstructure Scatterer Distribution with Spectral Correlation", *Ultrasonic Imaging*, vol. 15, pp.238-254, 1993.

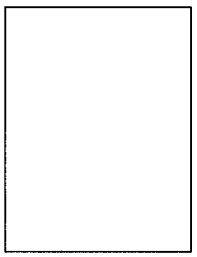

Udantha R. Abeyratne (M '94) was born in Matale, Sri Lanka. He received a B.Sc.(Honors) degree in electrical and electronic engineering from the University of Peradeniya, Peradeniya, Sri Lanka in 1985 and a M.S. degree in electrical engineering from The University of Tokushima, Tokushima, Japan, in 1991. Currently he is a Ph.D. candidate at the Biomedical Engineering and Science Institute, Drexel University, Phailadelphia. From 1985 to 1988 he was an assistant lecturer in electrical engineering at the University of Peradeniya, Sri Lanka. From 1988-1989 he was with the University of Tokushima, Japan, as a researcher, where he studied artificial neural networks in communication engineering. During the period 1988-1991, he was a *Monbusho* scholar of the Ministry of Education, Japan. from 1992-1994 he held a *Calhoun* fellowship at the Biomedical Engineering and Science Institute, and a research assistantship at the Electrical and Computer Engineering Department, both of Drexel University. In 1990 he co-received the *President's Award for the Best Paper* award at the International Congress on Brain Electromagnetic Topography, Osaka, Japan. His research interests include higher order statistics, system identification, ultrasound imaging and tissue characterization, digital signal/image processing and the functional electromagnetic imaging of the brain. He is currently a member of the I.E.E.E. Signal Processing and E.M.B.S societies.

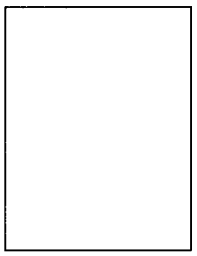

Athina P. Petropulu (S'86-M'91) was born in Kalamata, Greece. She received the Diploma in Electrical Engineering from the National Technical University of Athens, Greece in 1986, the M.Sc. degree in Electrical and Computer Engineering in 1988 and the Ph.D. degree in Electrical and Computer Engineering in 1990 both from Northeastern University, Boston. Since September 1992 she is an Assistant Professor in the Electrical and Computer Engineering Department and the Biomedical Engineering and Science Institute, both at Drexel University, Philadelphia. She is the coauthor (with C.L. Nikias) of the textbook *Higher-Order Spectra Analysis: A Nonlinear Signal Processing Framework* (Englewood Cliffs, NJ: Prentice-Hall, Inc., 1993.) Her research interests span the area of statistical signal processing, communications, higher-order spectra analysis, image/speech processing, biomedical engineering and earthquake engineering. In 1995 she received the *Presidential Faculty Fellow Award (PFF)* for her work in Electrical Engineering. She has served as an Associate Editor for the IEEE TRANSACTIONS ON SIGNAL PROCESSING. Dr. Petropulu is member of the Technical Chamber of Greece and the Greek Association of Electrical and Electronic Engineers.

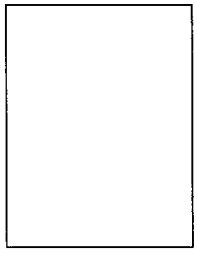

John M. Reid (SU48,-AU51-MU56-SMU79-FU84-LFU92) was born in Minneapolis, MN, in 1926. He received the B.S. and MS. in electrical engineering from the University of Minnesota and the Ph.D. from the University of Pennsylvania. He worked on medical diagnosis with ultrasound at the University of Minnesota and St. Barnabas Hospital, MN, from 1950-1957, and developed the first ultrasonic scanner. At the University of Pennsylvania (1957-1965), he worked on echocardiography, and developed methods for making ultrasonic scattering measurements in tissues. He was a Research Assistant Professor at the University of Washington from 1966-1971, where he continued the tissue research and worked on the Pulse Doppler and duplex imaging devices. He participated in forming the Institute of Applied Physiology and Medicine in Seattle, and was also affiliated with Providence Hospital from 1971 to 1981, while working on measurements, Doppler imaging and other ultrasonic developments. He occupied the Calhoun Chair of Biomedical Engineering at Drexel University from 1981 to 1994, and became an Adjunct Professor of Radiologyt at Thomas Jefferson

University, both in Philadelphia. He is currently an Emeritus and Research Professor at Drexel, and an Affiliate Professor at the Univsity of Washington (Seattle). Dr. Reid is a fellow of the Acoustical Society of America, the American Institute of Medical and Biological Engineering, and the American Institute of Ultrasound in Medicine. He received his Lifetime Achievement Awarding of the IEEE Engineering in Medicine and Biology Society.

TABLE I

Simulation-I: MONTE CARLO SIMULATIONS FOR PERIODICITY ESTIMATION USING POWER CEPSTRUM AND THE PROPOSED METHOD.

	Mean (mm)	*Variance* (mm^2)
True Period	1.00	0.000
Power cepstrum method	0.91	0.026
Proposed method	0.97	0.005

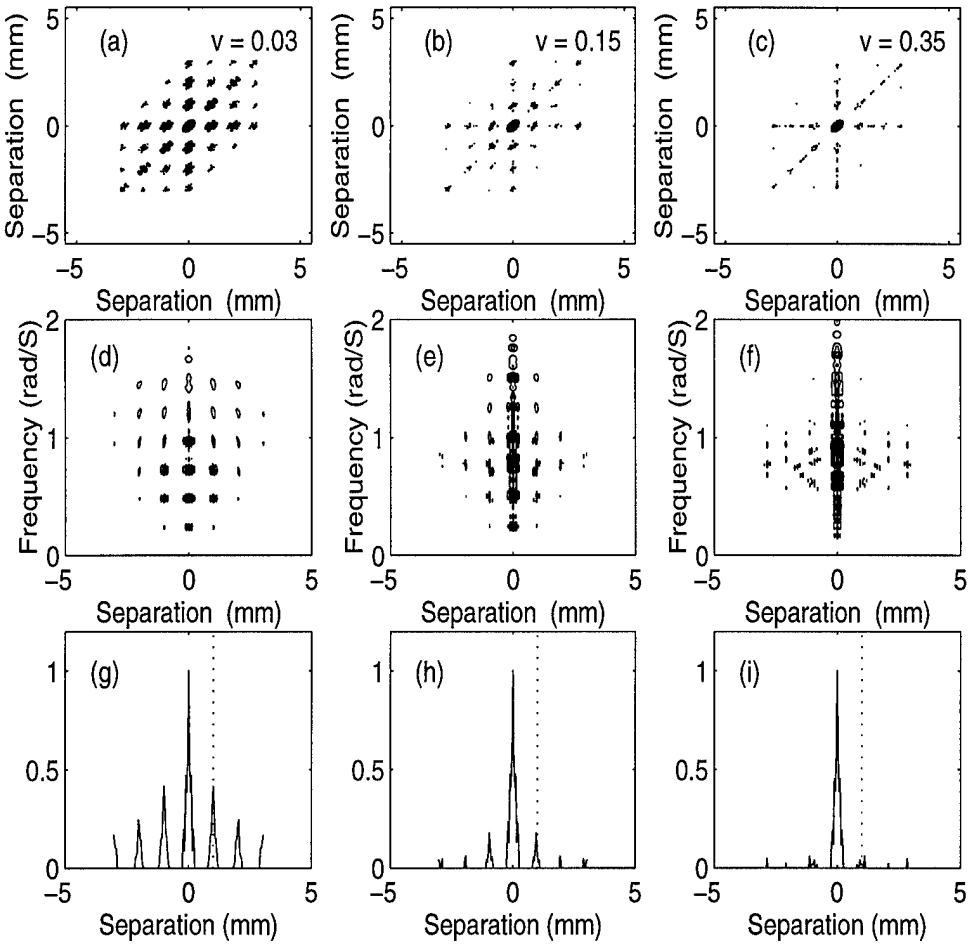

Fig. 1. *Simulation I:* (a), (b), (c) Contour maps for the absolute values of cumualnts corresponding to $v = 0.03, 0.15, 0.35$, (d), (e), (f) contour maps of $|p_3^y(\tau_1, \omega)|$, $0 \leq \omega < \pi$ for cases $v = 0.03, 0.15, 0.35$, (g),(h),(i) smoothed, projected $|p_3^y(\tau_1, \omega)|$ along the ω-axis for cases $v = 0.03, 0.15, 0.35$. The dotted lines in (g), (h) and (i) indicate the true periodicity, $1mm$.

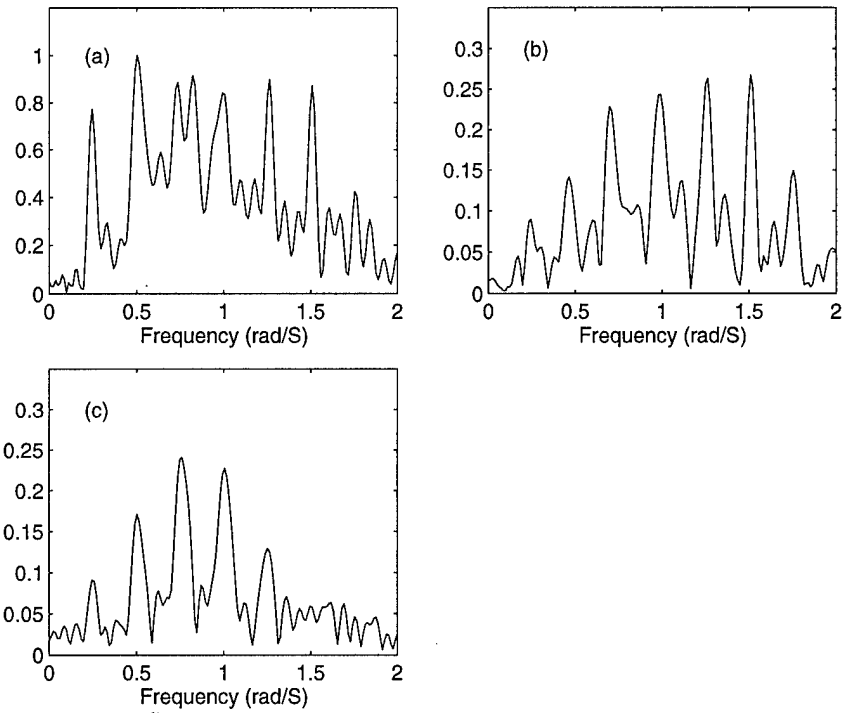

Fig. 2. *Simulation I:* The slices of the $|p_3^y(\tau_1, \omega)|$ along the ω-axis corresponding to (a) $\tau_1 = 0.0$mm, (b) $\tau_1 = 1.0$ mm, (c) $\tau_1 = 2.0$mm. The spectral peaks are separated by $2\pi/T$, where T is the period.

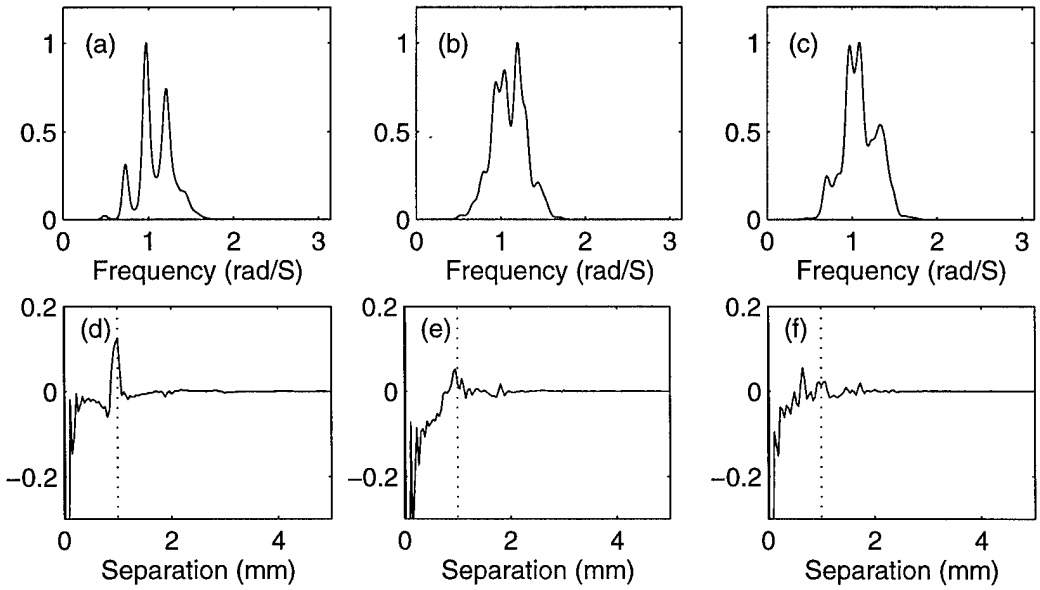

Fig. 3. *Simulation-I:* (a), (b), (c) The power spectrum for cases $v = 0.03, 0.15, 0.35$, and, (d),(e),(f) the power cepstrum for cases $v = 0.03, 0.15, 0.35$, of the RPC-only digitized RF scan line segments. True periodicity, $1mm$, is indicated in (d),(e) and (f) by dotted lines.

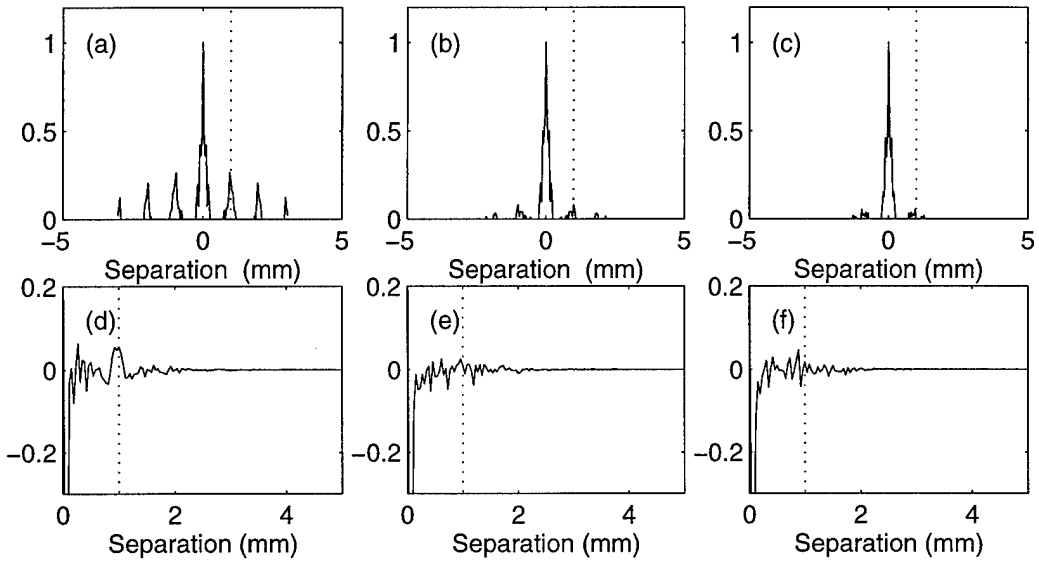

Fig. 4. *Simulation II:* (a), (b) ,(c) The smoothed, projected $|p_3^y(\tau_1, \omega)|$ along the ω-axis for $v = 0.03, 0.15, 0.35$, and, (d),(e),(f) the power cepstrum for $v = 0.03, 0.15, 0.35$. In all cases, the true period is indicated by dotted lines.

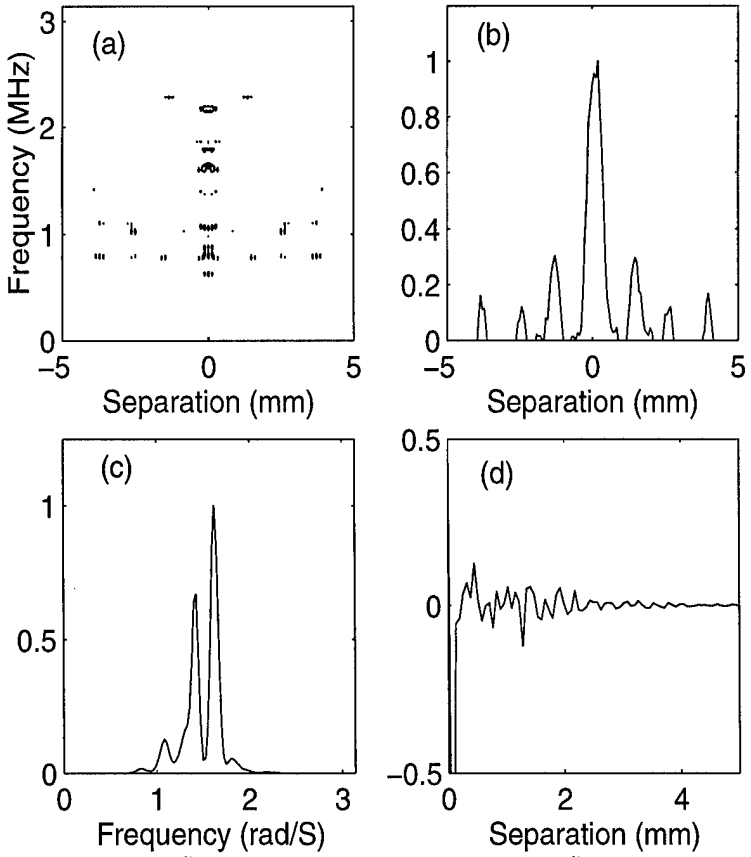

Fig. 5. *Normal liver:* (a) The contour map of $|p_3^y(\tau_1, \omega)|$, (b) the smoothed, projected $|p_3^y(\tau_1, \omega)|$ along the ω-axis, (c) the power spectrum, and, (d) the power cepstrum corresponding to the liver image of the normal subject, *Volunteer-I.*

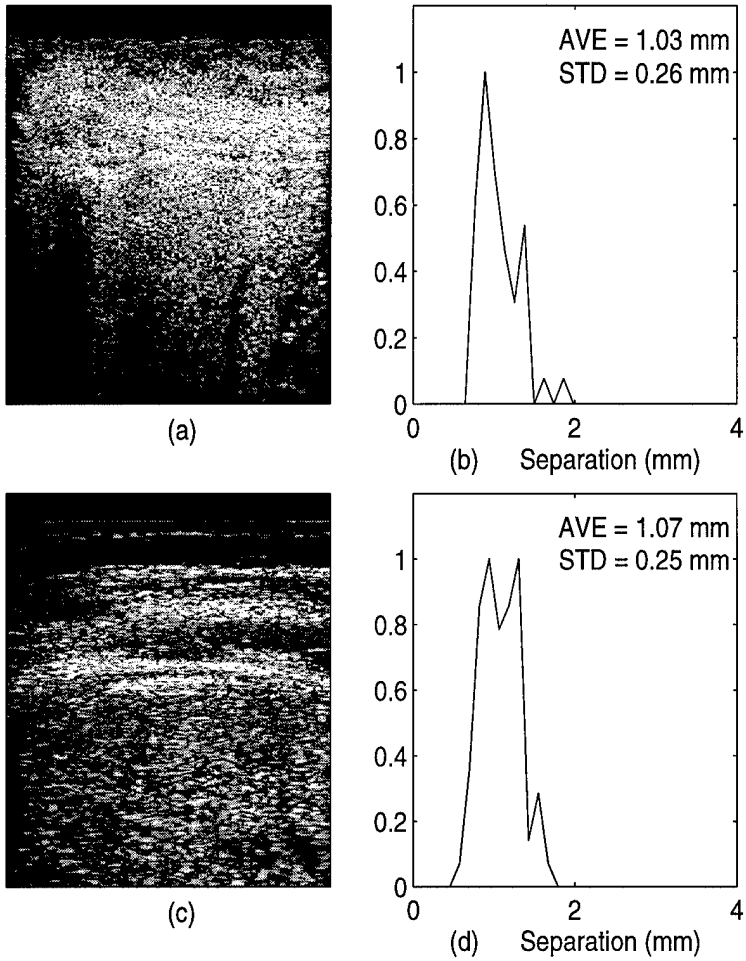

Fig. 6. *Normal liver:* (a),(c) B-mode images of parts of normal liver obtained from *Volunteer-I and II*, (b), (d) the normalized histogram for the mean scatterer spacing estimate corresponding to (a) and (c). The number of estimates involved in forming the histograms is 80. Average and the standard deviation for *Volunteer-I* are 1.03 and 0.26 *mm*. Corresponding numbers for *Volunteer-II* are 1.07 and 0.25 *mm*.

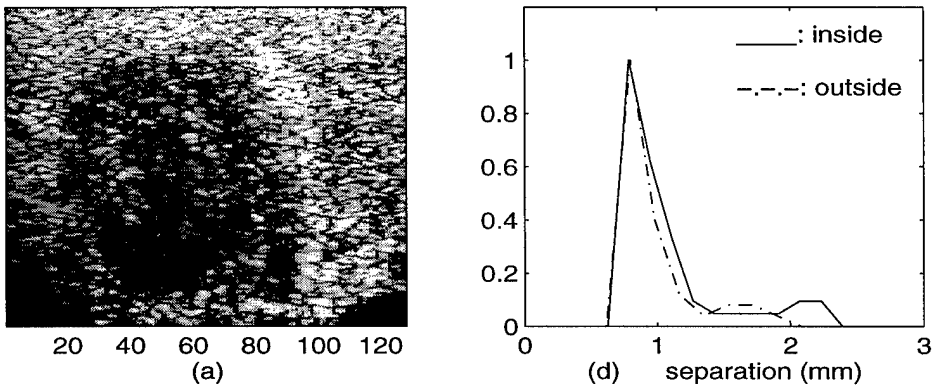

Fig. 7. *Tumor of the Liver* (a) The B-mode image of a liver with a hypo-echoic tumor, (b) the histograms of the mean-scatterer spacings estimated from inside and outside the tumor. The average and the standard deviation estimated inside the tumor are respectively 1.07 and 0.42 *mm*, while the corresponding numbers obtained from outside the tumor are 0.97 and 0.31 *mm*.

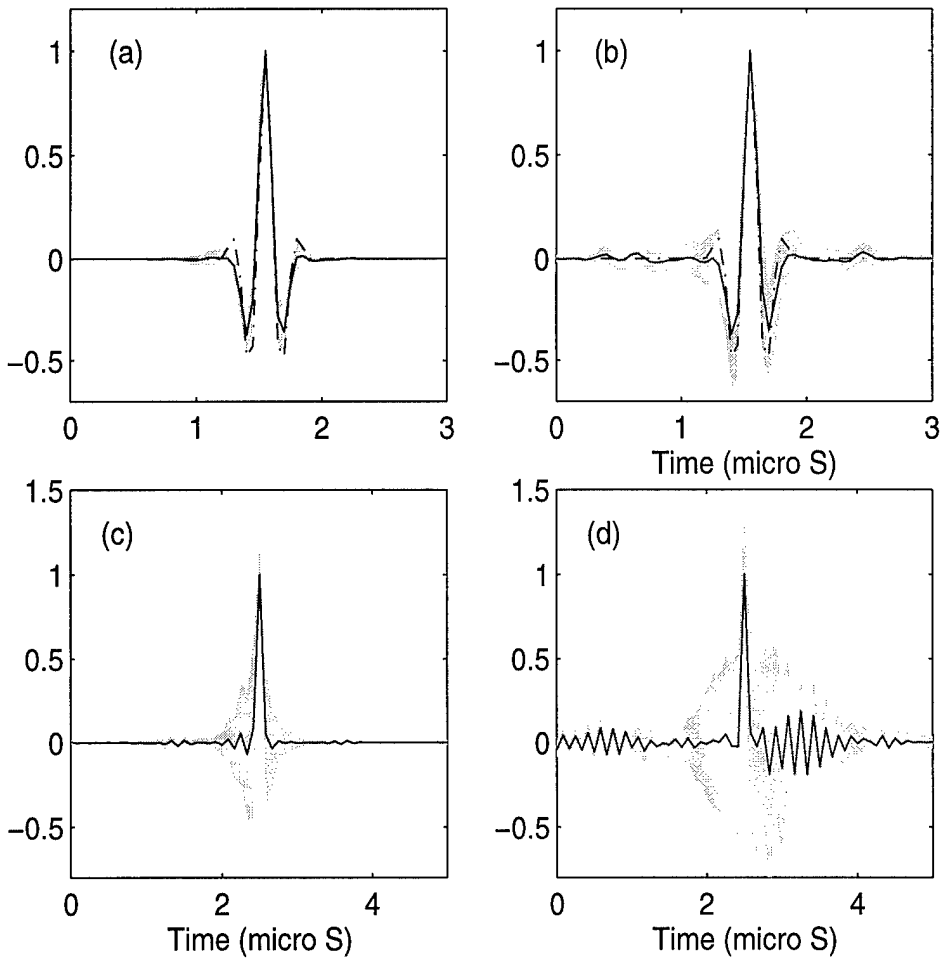

Fig. 8. *Color of the tissue response:* (a) The combined kernel $u_1(k)$ corresponding to $v = 0.05$, (b) the combined kernel $u_2(k)$ corresponding to the case $v = 0.35$ and short-range, correlated scatterers. The true pulse used in the simulation is shown in a dash-dotted line, and the average estimate evaluated over 50 Monte Carlo runs is indicated in a solid line. The shaded area represents average $\pm$ one standard deviation. (c) The estimator S_{11}, and (d) S_{21}; solid line indicates the average over 50 Monte Carlo runs, and the shaded area represents the average $\pm$ one standard deviation.

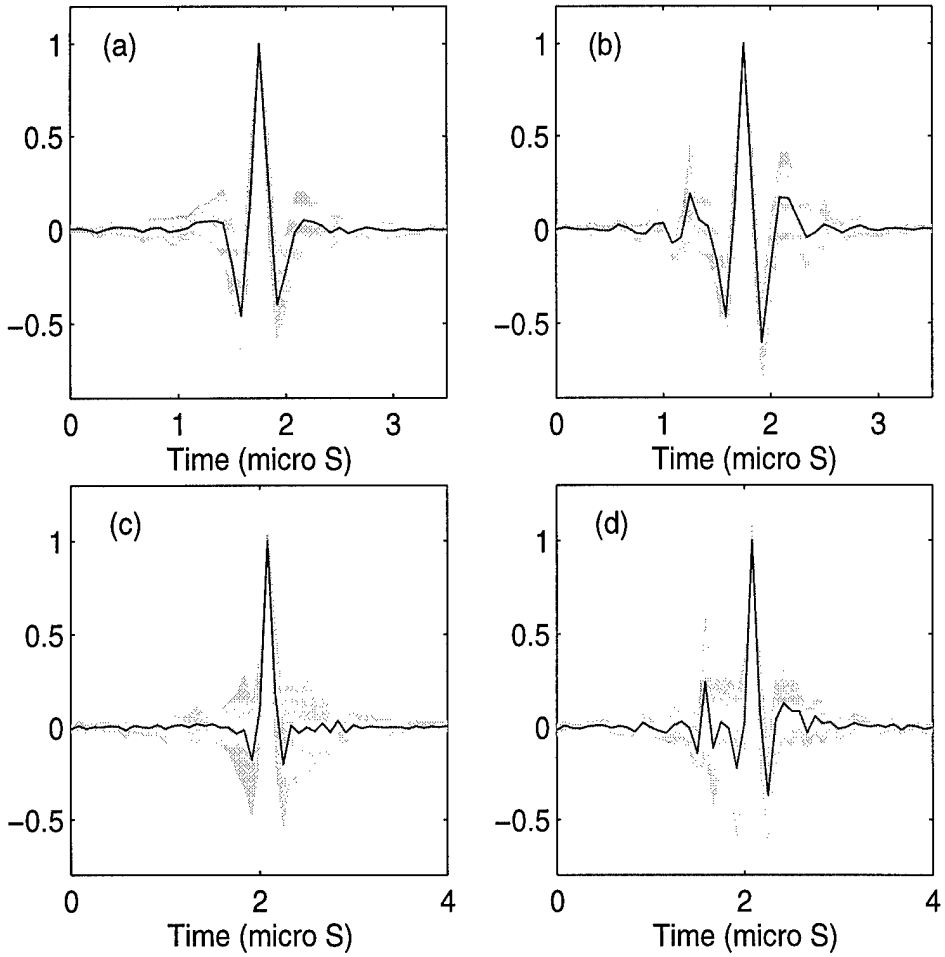

Fig. 9. *Tumor of the liver:* Combined kernels estimated form (a) inside, and (b) outside the tumor; (c) the color of the tissue response signature S_{11} estimated inside the tumor and (d) S_{21} estimated outside the tumor. In all cases the solid line indicates the average estimation, and the shaded area represents average $\pm$ one standard deviation.